



# Universidad de Navarra

**Facultad de Farmacia**

**TESIS DOCTORAL**

**Targeted Polymeric Nanoparticles:  
Radiolabelling with Ga-67 and *in vivo*  
Evaluation in a Mouse Model of Pancreatic  
Adenocarcinoma using Single Photon Emission  
Computerized Tomography**

**Larraitz Gil Iceta**

**Pamplona, 2016**





Universidad  
de Navarra

**Targeted Polymeric Nanoparticles:  
Radiolabelling with Ga-67 and *in vivo*  
Evaluation in a Mouse Model of Pancreatic  
Adenocarcinoma using Single Photon Emission  
Computerized Tomography**

**Larraitz Gil Iceta**

Thesis dissertation submitted to the Faculty of Pharmacy of the  
University of Navarra (UNAV) in the fulfillment of the  
requirements of the degree of Doctor of Philosophy

Pamplona, June 2016



## DECLARATION

The present work entitled “Targeted Polymeric Nanoparticles: Radiolabelling with Ga-67 and *in vivo* Evaluation in a Mouse Model of Pancreatic Adenocarcinoma using Single Photon Emission Computerized Tomography” has been conducted at CIC biomaGUNE under the supervision of Dr. Jordi Llop Roig, principal investigator and head of Radiochemistry of CIC biomaGUNE, and the co-supervision of Dr. Iván Peñuelas Sánchez, head of the Radiopharmacy department at the Clínica Universidad de Navarra.

Heads gathered, we state that Ms. Larraitz Gil Iceta meets the requirements to obtain the PhD mention by the University of Navarra and declare that the work can be presented to the examining panel for judgment.

And for the record, we hereby sign the present document:

Dr. Jordi Llop Roig

Dr. Iván Peñuelas Sánchez



The experimental part of this PhD thesis has been fully conducted in the Molecular Imaging Facility of CIC biomaGUNE. The research was part of the collaborative project Save Me “A Modular Active Nano-Platform for Advanced Cancer Management: Core Nanosystems, Tumor Targeting and Penetration, Molecular Imaging & Degradome based Therapy”. The project as a whole was executed by a consortium of 21 groups from 8 different countries and funded by the European Commission under the FP7 NMP theme (No. CP-IP 263307 grant).

Ms. Larraitz Gil Iceta has been funded by a pre-doctorate studentship program from the Department of Education, Language Policy and Culture of the Basque Government.





*Bonum est diffusivum sui*



## ACKNOWLEDGEMENTS

Firstly, I would like to express my gratitude to Prof. Manuel Martín Lomas and Prof. Luis M. Liz Marzán, former and current scientific directors of CIC biomaGUNE, respectively, for giving me the opportunity to develop the experimental work of this PhD in the outstanding facilities of the centre.

Sincere thanks are for my supervisors Dr. Jordi Llop and Dr. Iván Peñuelas for giving me the opportunity to work on an interesting topic. Specially, I would like to stress Jordi's necessary support during the whole project. He was always available whenever I needed to brainstorm fundamental concepts and analyse results. His meticulous critiques and the high standards he set during his instructing made me work hard.

I would not have come close to completing my doctorate without the help and friendship of my current and former fellow lab members, students and colleagues from the entire institute, your diverse backgrounds and histories have made me rich! I am extremely grateful for all help received from my group: Eunice, Jaya, Olatz, Aitor, Ángel, Carlos, Kiran, Krishna, Luis, Luka, Mikel E., Mikel G., Sameer, Unai, Víctor, Vijay and Xabi, especially to María P., Vanessa and Zuriñe who were highly involved in my experiments. Thank you guys for so much fun in the lab and comforting atmosphere, long working hours were enjoyable and rewarding with all of you.

I feel so much appreciated to the all the people working in the Molecular Imaging Unit, who are entitled extra acknowledgement for their always professional assistance: Image Analytics (Eneko), MRI (Géraldine, Sandra, Dani and Pedro), Nuclear Imaging (Bogdan), Animal Facility (Ainhoa and Ander) platforms, Torsten Reese and his research group, particularly María J. and Enrique for their invaluable contribution to this thesis.

I would like to recognise the work of IT, maintenance and administration departments as well as the labour of cleaning ladies.

The Save Me project involved active collaboration among other research groups from whom I learnt a lot and fostered healthy working relationships. For that reason, I thank all the people involved in the project for the very fruitful cooperation. Their critical comments during our collaboration group meetings were of great help.

## ACKNOWLEDGEMENTS

I would like to thank the financial support from the European Union's Commission 7-FP for funding the Save Me project as well as the PhD studentship from the Basque Government.

Thanks are also due to all the friends from Lasarte-Oria, San Sebastián and the ones from the University, for their support and sincere friendship.

Nobody has been more important to me but my family members who backed me up throughout the thesis project. Above all, I especially thank my parents, Fernando Gil and M<sup>a</sup> Luz Iceta for their unwavering support and sacrifices made to provide me with the numerous opportunities that I have had throughout my life. I am truly lucky to have such dedicated and hardworking parents as mentors and role models. I owe much gratitude to my brother Fernando for keeping alive my joy for discovery and appetite for learning, and to my sister Ainoa, who makes a world of difference and loves me as only a sister can.

And of course, especial thanks are for my beloved Pablo J. Oroz, whose continuous encouragement, understanding, temperance and emotional support always kept my sights firmly set on my goal.

## ABSTRACT

Nanoparticle (NP) based theranostics may play a pivotal role in oncology in the near future. However, determination of the pharmacokinetic (PK) properties of novel nanomedicines, which is essential for the determination of the effective dose and potential translation into the clinical setting, is extremely challenging. Radiolabelling of the NPs with positron or gamma emitters and subsequent imaging studies using nuclear imaging techniques can provide relevant information on the PK properties of novel nanomedicines, aiding in the selection of the most promising candidates while enabling the discontinuation of non-appropriate drugs at early stages in the process of drug development.

Within the frame of the EU-funded project “SaveMe”, NP-based theranostic agents for the early detection and treatment of Pancreatic Cancer (PaCa, the fourth deadliest cancer type), have been developed. Different polymeric and protein-based NPs were synthesised by different partners and decorated with targeting moieties with high affinity for somatostatin (SST) or galectin (Gal) receptors, both over-expressed in PaCa cells. In this PhD thesis, the different particles have been radiolabelled with  $^{67}\text{Ga}$  *via* formation of chelator-radiometal complexes or by taking advantage of unspecific interactions between the radionuclide and the NP core. After assessing radiochemical integrity of the labelled NPs, Single Photon Emission Computerised Tomography (SPECT) studies were carried out in a subcutaneous mouse model of PaCa, which was implemented by subcutaneous injection of Panc-1 (human pancreatic adenocarcinoma) cells. The biodistribution of the labelled NPs and the accumulation of NPs in the tumour could be determined from SPECT images, which were combined with Computerised Tomography (CT) images for proper localisation of the radioactive signal. Complementary studies were performed with Magnetic Resonance Imaging, which provided relevant information regarding tumour heterogeneity. Imaging studies enabled the selection of the most appropriate NP core and the investigation of the effect of the targeting moieties and other surface decorations on the accumulation of the NPs in the tumour.

Results obtained with a SST-derived targeting moiety anchored to polymeric NPs prepared by partner CID suggested that these NPs might find application as therapeutic or diagnostic tools in the context of pancreatic cancer.



## RESUMEN

En un futuro, la teranóstica basada en el uso de nanopartículas (NPs) podría ser de vital importancia en oncología. Sin embargo, resulta extremadamente dificultoso determinar las propiedades farmacocinéticas (PC) de los nuevos nanofármacos, característica esencial para determinar la dosis efectiva y su posible aplicabilidad clínica. El radiomarcaje de NPs con emisores positrónicos o gamma y la adquisición de imágenes mediante técnicas de imagen nuclear, puede proporcionar información relevante de las propiedades PC de nuevos fármacos, permitiendo seleccionar aquellos candidatos más prometedores y descartar los que no lo son en etapas tempranas del proceso de desarrollo de nuevos medicamentos.

Dentro del marco de las investigaciones financiadas por la UE, se creó el proyecto "SaveMe", cuya finalidad era desarrollar agentes teranósticos para cáncer de páncreas (CaPa, el cuarto tipo tumoral con mayor mortalidad). Diversos participantes, desarrollaron diferentes NPs poliméricas y proteínicas y las decoraron con agentes específicos de alta afinidad por receptores somatostatínicos (SST) y de galectina (Gal), ambos sobreexpresados en células de CaPa. En esta tesis doctoral, se han marcado radiactivamente las NPs desarrolladas con  $^{67}\text{Ga}$ , bien mediante la formación de un complejo agente quelante-radiometal o mediante interacciones inespecíficas entre el radionúclido y el núcleo de las NPs. Tras estudiar la integridad radioquímica de las NPs marcadas, se ensayaron *in vivo* mediante Tomografía Computarizada por Emisión de Fotón Único (SPECT-CT), en un modelo animal de CaPa (realizado tras inocular de manera subcutánea células Panc-1 de adenocarcinoma pancreático de origen humano). Mediante las imágenes SPECT en combinación con la tomografía computerizada (CT), herramienta útil para la correcta localización de la señal radiactiva, se pudo determinar la biodistribución de las NPs marcadas y su acumulación en tumor. Se realizaron estudios complementarios mediante imagen por resonancia magnética, lo que permitió evaluar la heterogeneidad de los tumores. Gracias a los estudios de imagen y en función de su capacidad de acceso a los tumores, se seleccionó tanto el núcleo de NP más adecuado, el agente específico, como otras decoraciones de las NPs,.

Los resultados obtenidos con un agente específico derivado de SST unido a NPs poliméricas sintetizado por el colaborador CID, indican que dichas NPs poseen una potencial aplicabilidad como agentes terapéuticos o diagnósticos para cáncer de páncreas.





# CONTENTS

	Page
<b>ABBREVIATIONS</b> .....	<b>1</b>
<b>1. GENERAL INTRODUCTION</b> .....	<b>5</b>
1.1 PANCREATIC CANCER .....	7
1.1.1 Definition, Types, Epidemiology, Risk Factors .....	8
1.1.2 Current Treatment Options .....	14
1.2 NANOPARTICLES AS THERAPEUTIC AGENTS: NANOMEDICINE ...	16
1.2.1 Targeting moieties for Pancreatic Cancer .....	18
1.3 MOLECULAR IMAGING IN THE ASSESSMENT OF PK PROPERTIES OF NPS .....	22
1.3.1 Nuclear imaging .....	23
1.3.1.1 <i>PET and SPECT: Principles and System description</i> .....	25
1.3.2 Computerized Tomography (CT) .....	28
1.3.3 Magnetic Resonance Imaging (MRI) .....	29
1.3.4 Radiolabelling of Nanoparticles .....	30
1.3.4.1 <i>Radiolabelling strategies</i> .....	31
1.3.4.2 <i>Radiochemical stability of radiolabelled nanoparticles</i> .....	39
<b>2. MOTIVATION AND OBJECTIVES OF THE THESIS</b> .....	<b>45</b>
2.1 JUSTIFICATION OF THE STUDY: THE SAVE ME PROJECT .....	47
2.2 OBJECTIVES .....	50
<b>3. FIRST <i>IN VIVO</i> SCREENING: SELECTION OF MOST APPROPRIATE NP CORE AND TARGETING MOIETY</b> .....	<b>53</b>
3.1 INTRODUCTION .....	55
3.2 MATERIALS AND METHODS .....	58
3.2.1 Synthesis of targeting moieties .....	59
3.2.1.1 <i>Synthesis of SST analogues</i> .....	59
3.2.1.2 <i>Synthesis of tPA analogues</i> .....	60
3.2.2 Synthesis of nanoparticles .....	61
3.2.2.1 <i>Bar-Ilan University</i> .....	61
3.2.2.2 <i>Goethe University</i> .....	63
3.2.2.3 <i>University of Bologna</i> .....	63
3.2.2.4 <i>CIDETEC-IK4</i> .....	64
3.2.3 Radiolabelling of nanoparticles .....	67

## CONTENTS

3.2.3.1	<i>Purification of <sup>67</sup>Ga</i> .....	67
3.2.3.2	<i>Radiolabelling and purification of NPs</i> .....	69
3.2.3.3	<i>Radiochemical integrity of NPs</i> .....	72
3.2.3.4	<i>Dose preparation</i> .....	72
3.2.4	Imaging studies .....	73
3.2.4.1	<i>Animal model: athymic nude mice</i> .....	73
3.2.4.2	<i>Nuclear imaging studies: data acquisition and image processing</i> .....	77
3.2.4.3	<i>Magnetic resonance imaging (MRI)</i> .....	80
3.2.5	Statistical methods .....	83
3.3	RESULTS AND DISCUSSION .....	85
3.3.1	Radiolabelling of nanoparticles .....	85
3.3.1.1	<i>Purification of <sup>67</sup>Ga</i> .....	85
3.3.1.2	<i>Radiolabelling of NPs with <sup>67</sup>Ga</i> .....	88
3.3.1.3	<i>Radiochemical integrity of NPs</i> .....	92
3.3.1.4	<i>Dose preparation</i> .....	95
3.3.2	Animal model: human pancreatic carcinoma tumours growth and characterization .....	96
3.3.3	<i>In vivo</i> biodistribution imaging studies .....	100
3.3.3.1	<i>SPECT-CT: biodistribution pattern of the different NPs</i> .....	100
3.3.3.2	<i>MRI: angiogenesis in the PaCa tumour stages</i> .....	116
3.4	CONCLUSIONS .....	120
<b>4. SECOND <i>IN VIVO</i> SCREENING: SELECTION OF OPTIMAL TARGETING WITH MOST PROMISING NP CORE</b> .....		<b>123</b>
4.1	INTRODUCTION .....	125
4.2	MATERIALS AND METHODS .....	128
4.2.1	Synthesis of targeting moieties .....	128
4.2.1.1	<i>Synthesis of SST analogues</i> .....	128
4.2.1.2	<i>Synthesis of tPA analogues</i> .....	128
4.2.2	Synthesis of nanoparticles .....	128
4.2.2.1	<i>CIDETEC-IK4</i> .....	129
4.2.2.2	<i>Goethe University</i> .....	131
4.2.3	Radiolabelling of nanoparticles .....	132
4.2.3.1	<i>Purification of <sup>67</sup>Ga</i> .....	132
4.2.3.2	<i>Radiolabelling and purification of NPs</i> .....	132
4.2.3.3	<i>Radiochemical integrity of NPs</i> .....	133
4.2.3.4	<i>Dose preparation</i> .....	133
4.2.4	Imaging studies .....	134

## CONTENTS

4.2.4.1	<i>Animal model: athymic nude mice</i> .....	134
4.2.4.2	<i>Nuclear imaging studies: data acquisition and image processing</i> .....	134
4.2.5	Statistical methods .....	136
4.3	RESULTS AND DISCUSSION .....	137
4.3.1	Radiolabelling of nanoparticles .....	137
4.3.1.1	<i>Radiolabelling of NPs with <sup>67</sup>Ga</i> .....	137
4.3.1.2	<i>Radiochemical integrity of NPs</i> .....	140
4.3.1.3	<i>Dose preparation</i> .....	143
4.3.2	Animal model: human pancreatic carcinoma tumours growth and characterization .....	144
4.3.3	<i>In vivo</i> biodistribution imaging studies .....	145
4.3.3.1	<i>SPECT-CT: biodistribution pattern of the different NPs</i> .....	145
4.4	CONCLUSIONS .....	160
5.	GENERAL DISCUSSION .....	161
6.	FINAL CONCLUSIONS .....	175
7.	CONCLUSIONES FINALES .....	181
8.	BIBLIOGRAPHY .....	187
9.	FIGURES AND TABLES INDEX .....	201
10.	ANEXX: ORIGINAL PUBLICATIONS .....	209



## ABBREVIATIONS

2D	Two-dimension
3D	Three-dimension
aa	Amino acid
ALARA	As low as reasonably achievable
ANOVA	Analysis of variance
BBB	Blood brain barrier
BFCA	Bifunctional chelating agent
BI	Before injection
CAN	Cerium ammonium nitrate
CNS	Central nervous system
CPS	Counts per second
CT	Computerized tomography
DLS	Dynamic light scattering
DMTMM	4-(4,6-dimethoxy-1,3,5-triazin-2-yl)-4-methylmorpholinium
DOTA	1,4,7-tetraazacyclododecane-1,4,7,10-tetraacetic acid
DOTA-NHS	1,4,7,10-tetraazacyclododecane-1,4,7,10-tetraacetic-NHS ester
DTPA	Diethylenetriaminepentaacetic acid
εc	Electron capture
ECACC	European Collection of Cell Cultures
EDC	1-ethyl-3-(3-dimethylaminopropyl) carbodiimide
EPR	Enhanced permeation and retention effect
FBP	Filtered-back-projection
FDA	Food and Drug Administration
FITC	Fluorescein isothiocyanate
FOV	Field of view
FT-IR	Fourier transform Infrared Spectroscopy
GABA	Gamma-aminobutyric acid
Gal	Galectin receptor
GRAS	Generally recognized as safe
HEPES	4-(2-hydroxyethyl)-1-piperazineethanesulfonic acid
HPLC	High performance liquid chromatography
ICPC	International Cooperation Partner Country
IPMN	Intraductal papillary-mucinous neoplasm
iTLC/TLC	(Instant) thin layer chromatography
IV	Intravenous
MEN1	Multiple endocrine neoplasia type 1
MNP	Magnetic nanoparticle
MRI	Magnetic resonance imaging
MWCO	Molecular weight cut-off
(P)NET	(Pancreatic) neuroendocrine tumors

## ABBREVIATIONS

N/A	Not applicable
NH <sub>2</sub> -NODA-GA	2,2'-(7-(4-((2-aminoethyl)amino)-1-carboxy-4-oxobutyl)-1,4,7-triazonane-1,4-diyl)diacetic acid
MR	Nuclear magnetic resonance
NOTA	1,4,7-triazacyclononane-1,4,7-triacetic acid
NP	Nanoparticle
OSEM	Ordered subset expectation maximization
PaCa	Pancreatic Cancer
PAMAM	Polyamidoamide dendrimer
PBS	Phosphate buffered saline
PDAC	Pancreatic ductal adenocarcinoma
PDI	Polydispersity index
PEG	Polyethylene glycol
PET	Positron emission tomography
PI	Post injection
PK	Pharmacokinetic
PLGA	Poly(D,L-lactide-co-glycolide)
PMAAc	Polymethacrylic acid
PTR	Peptidic somatostatin analog conjugate
QD	Quantum dots
RCC	Radiochemical conversion
RE	Radiolabelling efficiency
RES	Reticuloendothelial system
rHSA	Recombinant human serum albumin
RT	Room temperature
s.i.	Signal intensity
SC	Subcutaneous
SCPN	Single chain polymeric nanoparticles
SEC	Size exclusion chromatography
SEM	Scanning electron microscopy
SPE	Solid phase extraction
SPECT	Single photon emission computerized tomography
SPION	Superparamagnetic iron oxide nanoparticles
SPPS	Solid phase peptide synthesis
SST	Somatostatin
SSTR	Somatostatin receptor
T/M	Tumour/Muscle ratio
TEM	Transmission electron microscopy
TF	Transferrin
tPA	Tissue plasminogen activator peptide ligand

## ABBREVIATIONS

UV	Ultraviolet
VIP	Vasoactive intestinal peptide
VOI	Volume of interest
WDHA	Watery diarrhea and hypokalemia achlorhydria
XO	Xylenol orange





# 1. GENERAL INTRODUCTION



## 1.1 PANCREATIC CANCER

Despite recent advances, cancer remains a pressing public health concern. There were 14.1 million new cancer cases worldwide in 2012, and the global cancer burden is expected to nearly double to 21.4 million cases and 13.5 million deaths by 2030. Advances in the early diagnosis and treatment of cancer have raised the 5-year relative survival rate for all cancers from 50 % (1974) to 68 % (2007) (1); however, cancer still accounted for 8.2 million deaths worldwide in 2012 (2), and for some types of cancer incidence equals mortality (4,5).

Pancreatic cancer is one of the most aggressive cancer types. With a 5-year survival rate lower than 5 % and an average survival rate below 6 months, it remains as one of the deadliest solid malignancies. The development of new treatments and therapies is therefore urgently needed, together with the implementation of early diagnostic tools, which require the identification of new biomarkers over-expressed in these tumour types. Currently, there are no efficient and sensitive methods for the early detection of pancreatic cancer and only 10 % - 15 % of patients are diagnosed in the early stages of the disease (4–7).

### 1.1.1 DEFINITION, TYPES, EPIDEMIOLOGY, RISK FACTORS

The pancreas is a fifteen centimetres long-five centimetre wide gland located in the abdomen. With a shape similar to a flat pear, it is surrounded by the stomach, the small intestine, the liver, the spleen and the gallbladder. Anatomically, the pancreas is divided into a head, which rests within the concavity of the duodenum, a body lying behind the base of the stomach, and a tail, which ends abutting the spleen (see Figure 1). The neck of the pancreas is between the body and head, and lies anterior to the superior mesenteric artery and vein. The head of the pancreas surrounds these two vessels, and a small uncinata process emerges from the lower part of the head, lying behind the superior mesenteric artery (8).

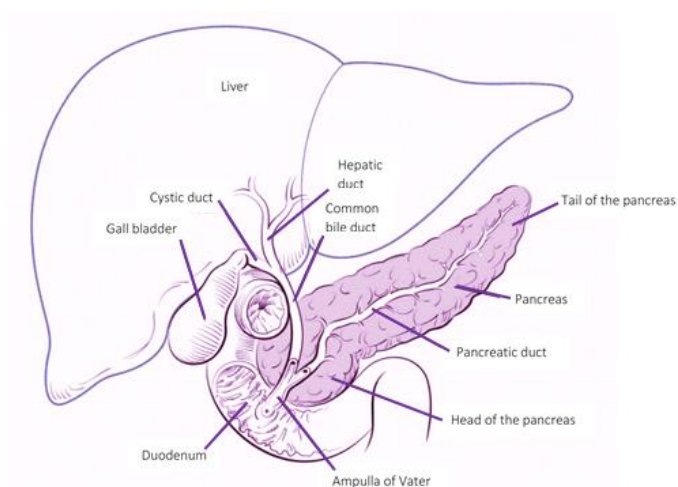


**Figure 1:** Anatomical description and localization of the pancreas. Image modified from reference (9).

The pancreas is a dual-function gland, having features of both endocrine and exocrine glands. Exocrine cells of the pancreas produce enzymes that assist the digestive system. More than 95 % of the cells in the pancreas are in the exocrine glands and ducts. When food enters the stomach, exocrine cells release the pancreatic enzymes into a system of small ducts that lead to the main pancreatic duct. The pancreatic duct, which runs the length of the pancreas, carries pancreatic enzymes and other secretions, collectively called pancreatic juice. The main pancreatic duct connects with the common bile duct, which carries bile from the gallbladder, and together they connect with the duodenum at the ampulla of Vater. Here, bile and pancreatic enzymes enter the duodenum to aid with the digestion of fats, carbohydrates and proteins.

The endocrine cells of the pancreas produce hormones (10). Hormones are substances that control or regulate specific functions in the body and are usually synthesized in one part of the body and carried through the blood to take action in a different location. A small percentage of the cells in the pancreas are *endocrine* cells. These cells are in small clusters called *islets* (or *islets of Langerhans*). Islet cells are endocrine cells within the pancreas that produce and secrete insulin and glucagon into the bloodstream. Insulin and glucagon lower and raise blood sugar levels, respectively. Together, these two main hormones maintain appropriate sugar levels in blood. Finally, the islet cells also produce a hormone called somatostatin, which regulates the levels of a variety of other hormones in the blood.

Pancreatic cancer begins when abnormal cells within the pancreas grow out of control and form a tumour. The two types of cells in the pancreas (exocrine cells and endocrine cells) form different types of tumours (exocrine and endocrine, respectively), which have distinct risk factors, causes, signs and symptoms, and are diagnosed using different tests, treated in different ways, and have different outlooks.

*Pancreatic exocrine tumours*

Exocrine tumours account for more than 95 % of pancreatic cancers. Within this category, the vast majority of tumours are adenocarcinomas. The main different types of pancreatic exocrine tumours are described in Table 1.

**Table 1:** Pancreatic cancer exocrine tumour types.

Types	Description
<b>Adenocarcinoma</b>	Accounting for about 95 % of all pancreatic cancers, pancreatic tumours are commonly known as pancreatic adenocarcinomas (PDACs). These begin in the cells lining the pancreatic duct and affect to the cells producing insulin.
<b>Acinar Cell Carcinoma</b>	Acinar cell carcinoma is a very rare form of pancreatic cancer, and it is caused by an excessive production of pancreatic lipase, the enzyme secreted to digest fats. The levels of pancreatic lipase can be measured in blood.
<b>Intraductal Papillary-Mucinous Neoplasm (IPMN)</b>	An IPMN is a cystic tumour that grows from the main pancreatic duct or from side branches of the duct and may therefore be a precursor for adenocarcinomas. The tumour may appear as a papillary (finger-like) projection into the duct. Although an IPMN may be benign at the time of diagnosis, it has a risk of progressing to malignancy mainly when the IPMN originates in the main pancreatic duct.
<b>Mucinous Cystadenocarcinoma</b>	Mucinous cystadenocarcinoma is a rare, malignant, cystic tumour which is mostly present in women. The characteristic of this tumour is that the cyst is filled with a thick fluid called mucin. It is similar to an IPMN but occurs in just one area of the pancreas, more commonly in the tail.

Other less frequent types of exocrine pancreatic tumours, not listed in the previous table, include adenosquamous carcinomas, squamous cell carcinomas, signet ring cell carcinomas, undifferentiated carcinomas and undifferentiated carcinomas with giant cells.

*Pancreatic endocrine tumours*

Pancreatic endocrine tumours, also known as pancreatic neuroendocrine tumours (NETs or PNETs) or islet cell tumours, account for less than 5 % of all pancreatic cancers. They develop from the abnormal growth of endocrine (hormone-producing) islet cells. They may be benign or malignant, tend to grow slower than exocrine tumours and are typically diagnosed once the tumour is advanced and is causing symptoms such as pain or jaundice (11).

Pancreatic neuroendocrine tumours are classified according to their hormone production as either functional or nonfunctional. Functional neuroendocrine tumours lead to overproduction of hormones, resulting in hormone-related symptoms such as gastrinomas and insulinomas. Nonfunctional tumours do not produce any hormones and consequently do not cause hormone-related symptoms. The majority of PNETs are nonfunctional tumours. With the exception of the insulinomas, nonfunctional tumours are usually malignant or have a high potential to become malignant (12). Due to the lack of hormone production, symptoms do not appear and tumours can often grow quite large before they are detected; however, the outlook of any type of NET is better than that of pancreatic exocrine cancers. The most important types of pancreatic neuroendocrine tumours are included in Table 2.



**Table 2:** Pancreatic cancer endocrine tumour types.

Types	Description
<b>Gastrinoma (Zollinger-Ellison Syndrome)</b>	In this type of PNET, gastrin is overproduced. When this tumour is inherited as part of a genetic syndrome called Multiple Endocrine Neoplasia Type 1 (MEN1), multiple tumours (likely to become malignant) may be found in the head of the pancreas and/or the duodenum.
<b>Glucagonoma</b>	In this type of PNET, glucagon is overproduced. Glucagonomas are commonly found in the body and tail of the pancreas. They are usually large, often metastasize and have a very high potential to become malignant, although they rarely occur.
<b>Insulinoma</b>	Insulinomas overproduce insulin. They are the most common type of functional pancreatic neuroendocrine tumours. They tend to be small and difficult to diagnose. Most of them are benign.
<b>Somatostatinoma</b>	Somatostatinomas overproduce somatostatin. They are extremely rare and usually very large. They can occur anywhere in the pancreas and in the duodenum and are very likely to become malignant.
<b>VIPoma (Verner-Morrison Syndrome)</b>	VIPomas produce vasoactive intestinal peptide (VIP). Two-thirds of VIPomas are found in women. The syndrome is also known as Watery Diarrhoea and Hypokalemia Achlorhydria (WDHA) Syndrome. They tend to become malignant.
<b>Nonfunctional Islet Cell Tumour</b>	Nonfunctional islet cell tumours are usually malignant and difficult to detect.

Pancreatic cancer symptoms, if present, are often vague. Hence, many patients are diagnosed at an advance stage of the disease. The symptoms vary depending upon the type of cancer, the location of the tumour, and its stage; common symptoms include jaundice, abdominal and/or back pain, faeces colour change, digestive difficulties and unexplained weight loss. In the worst case scenario, ascites and blood clots are present.

The exact causes of pancreatic cancer are not yet well understood. Research studies have identified certain risk factors such as smoking habits, age, family history, long-standing diabetes, chronic or hereditary pancreatitis, alcoholism, and certain dietary habits (13,14). Environmental factors seem to play also a significant role in the development of this disease.

### 1.1.2 CURRENT TREATMENT OPTIONS

Pancreatic cancers are usually detected by imaging techniques; unfortunately, imaging studies are performed only after the onset of symptoms (15). Because such symptoms are usually few or vague if any, pancreatic cancer is usually detected at a late stage. Consequently, more than 80 % of new pancreatic cancer cases are detected at a metastatic stage, when the primary tumour is surgically resectable but metastases are not. In few fortunate cases, the tumour is detected at an early stage (16).

Depending on the type and stage of the cancer, the patient may be treated surgically, with radiation therapy, targeted therapy and/or palliative therapies (17). Once a tumour is detected, the cancers are staged usually by imaging techniques (stages IA to IV) and the treatment is applied accordingly.

The best treatment option is the surgical resection of the organ or part of it, but will be effective only when the tumour is still confined to the pancreas

and has not metastasized (18). After surgery, periodical medical check-ups are required in order to monitor possible dissemination to the lymph nodes (19). Unfortunately, tumours are usually detected once they have proliferated, and hence more aggressive treatments are needed (20). These treatments include chemotherapy, which basically uses drugs to kill rapidly dividing cells in the body preventing tumours from growing; radiation therapy, in which cells are killed by applying high-energy radiation such as x-rays or protons directed to the targeted region; or the combination of both therapies (21–23).

## 1.2 NANOPARTICLES AS THERAPEUTIC AGENTS: NANOMEDICINE

Nanoparticles (NPs) are small particles with sizes ranging generally from 1 to 100 nm. Due to their unique physical-chemical properties, NPs have shown to be promising tools with applications in different areas such as biomedicine (bioimaging, targeted drug and gene delivery), optics and electronics, among many others (24,25).

NPs to be used in biomedical applications, especially in the context of therapy, need to fulfil the following properties: (i) have an appropriate pharmacokinetic (PK) profile; (ii) have a high vascular circulation life-time to guarantee bioavailability; (iii) be stable over time; (iv) have a tunable surface, suitable for the functionalization with *e.g.* stabilizers or targeting moieties; (v) have the appropriate size for biodistribution purposes; and (vi) be able to cross cell membranes. Different biodegradable and biocompatible polymeric NPs, including both natural and chemically engineered polymers, have been used to develop non-toxic GRAS (Generally Recognized as Safe) and Food and Drug Administration (FDA) approved NPs (26,27).

One of the main advantages of NPs as therapeutic agents in oncology arises from two main factors: (i) their size; and (ii) their high surface-to-volume ratio, which enables multi-functionalization. NPs preferentially accumulate in tumour tissue due to the well-known enhanced permeability and retention (EPR) effect (28). This effect is based on the presence of leaky vasculature in

the vicinity of tumours, whose endothelium is fenestrated with gaps between 100 nm and 780 nm in size. This, together with a deficient lymphatic drainage, results in a passive accumulation of NPs in tumour tissue (see Figure 2). Such accumulation can be even improved by attaching targeting moieties to the surface of the NPs, with high affinity for specific receptors over-expressed in tumour cells but not in the surrounding healthy tissue. Because multiple targeting moieties can be attached to each individual NP, multiple interactions with the receptors present at the cell surface lead to improved retention and, eventually, internalization of the NP (29–31).

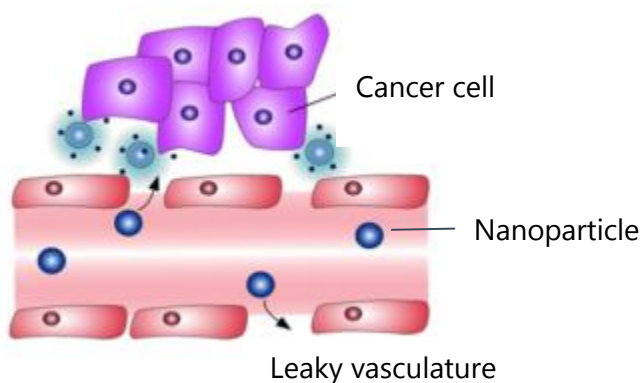


**Figure 2:** Schematic representation of passive targeting penetration for NPs access to tumour cells. Image modified from reference (32).

From the statements above, it is clear that NPs are promising tools for specific (or preferential) delivery of drugs in tumour cells, and NPs have been proposed in the literature as potential drug delivery agents, which should lead to improved selectivity and, in consequence, less off-target side effects.

The release of the therapeutic agent or drug to become effective once in the tumour can be triggered by different mechanisms (24,33,34).

Despite the above-mentioned advantages, the use of engineered NPs as therapeutic agents has several limitations that have hampered the development of NP-based systems with application in the clinical field and require careful consideration. Accurate analysis of such limitations is out of the scope of the current PhD thesis. Just to mention a few, unsolved problems include the batch-to-batch variability during production of the NPs, difficulties in accurate characterization of complex NPs and limitations in the production under Good Manufacturing Practices, which is strictly required to move into the clinical setting. Besides the above mentioned limitations, one major obstacle in the development of NPs as therapeutic agents is the need to assess their pharmacokinetic properties. This is extremely challenging because NPs are very difficult to detect after administration into living organisms. In this context, *in vivo*, non-invasive molecular imaging techniques gain relevance. This will be thoroughly discussed in section 1.3.

### 1.2.1 TARGETING MOIETIES FOR PANCREATIC CANCER

Abnormal metabolism and the over-expression of certain membrane receptors have been historically exploited to accumulate drugs in cancer cells. The vast majority of human malignancies tend to over-express one of

the somatostatin receptor (SSTR) subtypes compared to adjacent normal tissues (29,35,36). Native somatostatin (SST) is a small cyclopeptidic hormone produced in the Langerhans islets of the pancreas, consisting of a concatenation of 14 amino acids (aa), which plays an important role in controlling biological functions of the gastrointestinal tract (mainly colon and gut) *via* membrane coupled SSTRs. The recognition sites for somatostatin are the amino acids numbered 6 (Phenylalanine), 8 (Tryptophan), 9 (Lysine), 10 (Threonine) and 11 (Phenylalanine) (see Figure 3) (37).

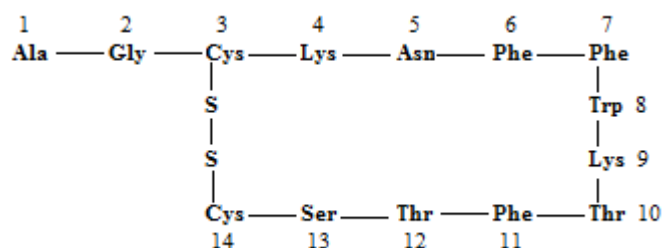


**Figure 3:** SST amino acid's sequence and structure. MW: 1638 g/mol.

Somatostatin receptors are actually a family of different receptors that can be classified according to the gene they are encoded as SSTR1, SSTR2, SSTR3 (expressed in highest levels in pancreatic islets), SSTR4 and SSTR5. Of note, the receptor sub-types can be expressed with different patterns depending on tumour type and may vary on a patient-to-patient basis, turning tumour targeting into a real challenge (38).

Somatostatin-based targeting seems to be a promising route towards improved pancreatic cancer detection and therapy because SSTRs are over-expressed in gastro-entero-pancreatic neuroendocrine tumours (39,40). Unfortunately, native somatostatin has a short half-life (2-3 minutes) due to enzymatic activity. This is the reason why novel SST analogues are being developed, with a longer duration of action although with (still) not full satisfactory selectivity results (25). Octreotide (with affinity for SSTR2 and SSTR3) is currently used as the gold standard for the detection of endocrine tumours. The IV administration of this commercially available drug, (composed by 8 amino acids, see Figure 4) with  $\gamma$ -emitting or  $\beta$ -emitting radionuclides shows rapid clearance from the tumour and a high uptake by normal tissue (42).

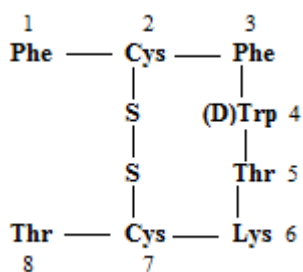


**Figure 4:** Octreotide amino acid's sequence and structure. MW: 1019 g/mol.

Other highly expressed tumour associated antigens could serve as tumour target proteins. Such is the case of Galectins, a family of proteins that bind poly-*N*-acetyllactosamine enriched glycol-conjugates. Galectin-1 (Gal-1), a member of this family, is an endogenous functional receptor located in cell membranes for tissue plasminogen activator (tPA). Being Gal-1 the target



(receptor) of the tPA peptide vector (ligand), tPA seems to send proliferative and invasive signals both to pancreatic tumour cells and to the surrounding fibroblasts, contributing thus to tumour progression.

### 1.3 MOLECULAR IMAGING IN THE ASSESSMENT OF PK PROPERTIES OF NPS

As mentioned above, one of the main limitations in the use of NPs as therapeutic agents is the lack of techniques suitable for the determination of the PK properties of NPs after administration in living organisms. In this regard, *in vivo* imaging techniques can play a pivotal role. Contrast agents can be incorporated into the NPs or attached to the NP surface in order to enable subsequent *in vivo* tracking using a combination of imaging modalities such as Positron Emission Tomography (PET), Single Photon Emission Computerized Tomography (SPECT) or Magnetic Resonance Imaging (MRI) eventually together with purely anatomical imaging modalities such as Computerized Tomography (CT). For example, magnetic NPs (MNPs) can be used as contrast agents for *in vivo* tracking in biological systems using MRI. MNPs can be engineered with organic ligands, which enable their entrapment into polymeric matrices, resulting in engineered nanosystems that retain to a certain extent the magnetic properties of the MNPs but allow surface functionalization with a plethora of bioactive moieties (43,44). Also, radionuclides can be incorporated into NPs by using different strategies, including (but not limited to) formation of a radiometal-chelator complex, attachment of pre-labelled prosthetic groups to the surface of the NPs, unspecific absorption of the radionuclide to the NP or direct neutron or ion irradiation (42,45). The use of different imaging modalities for the determination of the PK properties of engineered NPs with potential

application as therapeutic tools for pancreatic cancer is the core of the current PhD thesis. A detailed description of the most relevant imaging modalities used within this PhD, as well as an overview of the different labelling strategies used for the incorporation of radionuclides into NPs with special focus on the strategies used in this work is included in the following sections.

### 1.3.1 NUCLEAR IMAGING

Nuclear imaging techniques rely on the administration of trace amounts of compounds labelled with radioactive isotopes that enable external detection. The radiolabelled compound is called a radiotracer, tracer or radiopharmaceutical. Radionuclides emitting high-energy gamma-rays as a result of the disintegration process are suitable for this purpose, as gamma rays can travel through biological tissues without suffering significant scatter or attenuation and can be detected using specific instrumentation in such a way that the original concentration of radiotracer can be accurately quantified using tomographic reconstruction algorithms programmed into a computer.

Broadly, there are two different kinds of radioisotopes that are commonly used in nuclear imaging, gamma emitters and positron emitters, which differ in their respective decay routes. Gamma emitters decay by emitting a gamma

ray, while positron emitters decay by emission of a positron. In PET, the emitted positron has a very short lifetime and rapidly interacts with other charged particles and loses its kinetic energy while describing a random path. When most of this energy has been lost, positrons annihilate together with an electron. The annihilation process results in the emission of two gamma rays emitted 180 degrees apart. Two photons detected almost simultaneously by two different detectors will be assumed to arise from a single annihilation and the direction of the incident rays will be determined as the line between the two detectors.

Over time, radioactive compounds undergo exponential decay characterized by the half-life or the time required to half the initial radioisotope amount. Commonly used gamma emitters present half-lives ranging from several hours to days, whereas positron emitters typically have half-lives in the range from a few minutes to a few hours. This characteristic has a critical impact on the production and distribution of these two types of radioisotopes.

Both techniques, PET or SPECT allow the *in vivo* evaluation of new chemical entities once radiolabelled with a radioisotope. By PET imaging, absolute quantification of the biodistribution to the different tissues can be carried out, by analysing the dynamic images from which the time activity curves in each organ can be obtained. On the contrary, quantification in SPECT, despite possible, is much more challenging and usually semi-quantitative data is obtained.

### 1.3.1.1 PET and SPECT: Principles and System description

In order to capture the three dimensional location and concentration of the radioisotope, computed tomographic techniques require the detection of emitted gamma-rays and the determination of the direction of the incident ray. Many angular views (projections) have to be acquired in order to feed mathematical reconstruction algorithms to obtain tomographic datasets.

In SPECT, the typical configuration of the scanners consists of a gamma-ray detection module and a collimator (see Figure 5).

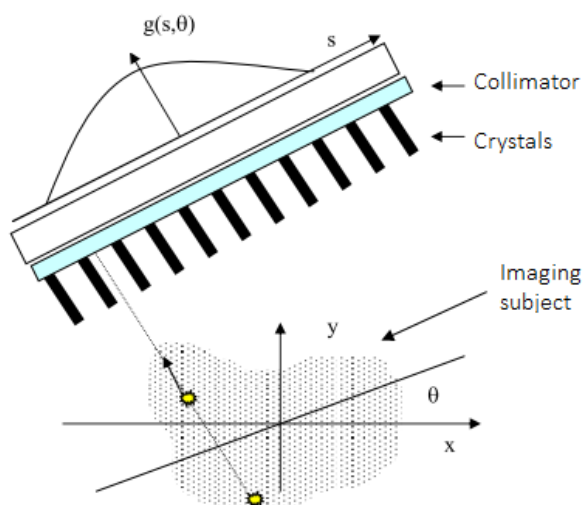


**Figure 5:** Principle of SPECT tomographic acquisition. In the representation,  $g(s, \theta)$  is the number of gamma photons detected at any location (s) along the detector crystals at a given angle ( $\theta$ ). Image adapted from reference (46).

The core of the detection module is normally a scintillation crystal, which absorbs its energy and re-emits the absorbed energy in the form of a flash of

light. This flash is subsequently detected by a photo-electronic system, which records its location in the crystal and its intensity, which is proportional to the energy of the incidental gamma-ray. The collimator most commonly consists of a lead plate containing a large number of holes, and serves the purpose of determining the direction of the detected rays. By stopping all the rays that do not reach the detector in a given direction, the collimator forms a projected image of the radioisotope distribution on the surface of the scintillation crystal (dashed lines in Figure 5).

In PET, the imaging strategy requires back-to-back detection heads (typically, PET scanners consist of a stationary array of full-ring pixelated detectors) and coincidence detection circuitry. PET scanners do not need collimators. Detection of the annihilation coincidences is known as ‘electronic’ collimation as opposed to the ‘physical’ collimation implemented in SPECT scanners. A schematic representation of SPECT and PET scanners is shown in Figure 6.

Both SPECT and PET systems acquire a set of projections at different angular positions around the body being imaged. Reconstruction tomography makes use of computers and mathematical algorithms to estimate the unknown distribution of radiotracer in the body from the detected projection data. The mathematical principles of tomographic image reconstruction fall beyond the scope of this thesis. From a user’s perspective, reconstruction algorithms can be roughly divided into analytical methods, and most notably the Filtered-Back-Projection (FBP) algorithm; and iterative statistical reconstruction

methods such as Ordered Subset Expectation Maximization (OSEM) and its many variants. Typically, iterative reconstruction methods provide images with improved spatial resolution and better signal-to-noise ratios at the expense of increased computational time and some unpredictability in the final outcome.

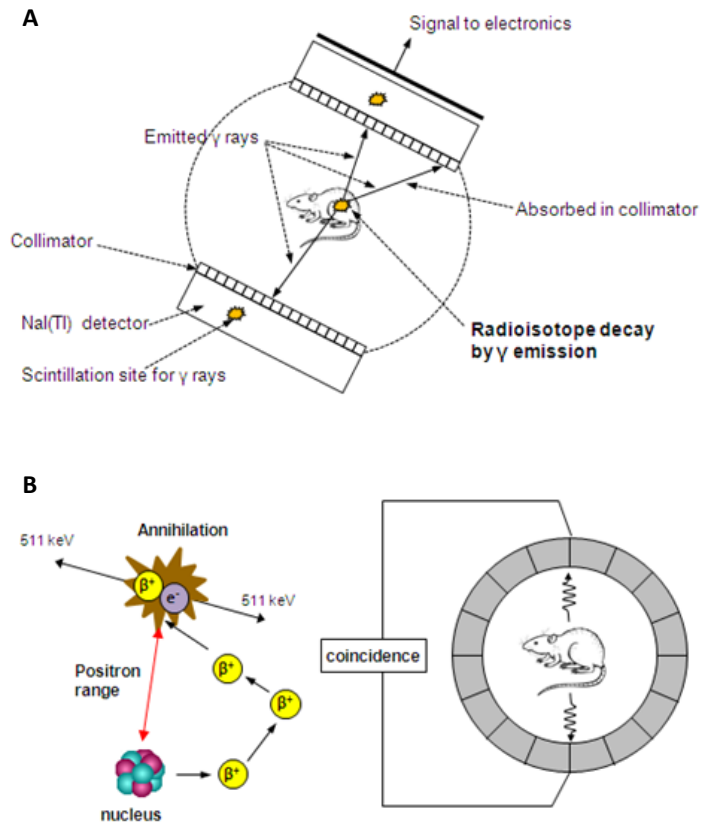


**Figure 6:** Schematic representation of the detection of photons using SPECT (a) and PET (b) scanners. Adapted from reference (47).

The use of nuclear imaging techniques (PET and SPECT) for the *in vivo* determination of the biodistribution of NPs requires, as a first step, radiolabelling (or incorporation of a radionuclide) of the NPs. This is covered in section 1.3.4 of the current PhD thesis.

### 1.3.2 COMPUTERIZED TOMOGRAPHY (CT)

The term computerized tomography, introduced in 1973 by Hounsfield,(48) is often used to refer to X-ray computerized tomography (X-ray CT), as by means of X-rays, virtual cuts of an object allowing the visualization of the its inner structures are produced (49).

The basis of this tomography procedure consists in an X-ray source and a series of detectors measuring intensity attenuation around a single axes of rotation of the object being imaged, producing three-dimensional (3D) images by acquiring a series of two-dimensional (2D) sequences in a non-invasive manner.

CT images provide anatomical information with high image resolution and good contrast in hard tissue. This is the reason why MRI is preferred to get anatomical information of soft tissues whereas CT is more frequently used for bone analysis and calcified tissue. Besides providing anatomical information, CT images are currently used in PET-CT and SPECT-CT systems to



obtain the attenuation map, which is later used for attenuation correction during image reconstruction.

### 1.3.3 MAGNETIC RESONANCE IMAGING (MRI)

MRI scans use radio waves and powerful magnets to take images of organs and structures inside the body by measuring their energy by imaging proton signal intensities. Similarly to CT, MRI takes several pictures of thin slices of the organ once the subject lies down motionless on a table set inside of a long cylinder. Then, a computer combines all of the images and creates a 3D image of the body (50). MRI scans do not involve exposure to radiation (49).

MRI is particularly useful in pancreas imaging because bile ducts can be specifically visualized. Due to this, MRI is a popular tool in tumour detection because of its high depth penetration, spatial resolution, and high soft tissue contrast (51).

Contrast agents are used in MRI to facilitate the visualization of normal and abnormal tissues, as contrast agents may selectively highlight the abnormal cells. Nowadays, Gadolinium Gd(III) is one of the main ones used but side effects to the nephritic system have been attributed. Additionally, they do not sufficiently enhance water proton relaxation rates. Most clinically used MRI contrast agents work through shortening the T1 and T2 relaxation times.

In general, transition metals have paramagnetic properties, which make them ideal candidates for MRI contrast agents. Consequently, paramagnetic and superparamagnetic contrast agents are currently being used in MRI to diagnose various diseases. Nowadays, NPs are being employed for MRI imaging and the different NP-based MRI contrast agents are classified based on the imaging modality (*i.e.*, T1 or T2 weighted) for obtaining an appropriate image contrast (51).

### 1.3.4 RADIOLABELLING OF NANOPARTICLES

Radiolabelling and subsequent imaging using PET or SPECT enables the determination of the spatiotemporal accumulation of the labelled NPs in tumours and other major organs and tissues. Hence, execution of comparative studies to assess the suitability of different functionalized NPs in order to determine the most promising candidates for therapeutic applications is straightforward. Radionuclides typically employed in the investigation of the PK properties of NPs are listed in Table 3.

**Table 3:** Physical decay characteristics of conventional positron emitting (PET) and gamma emitting (SPECT) radionuclides and most common production routes.

Radionuclide	Half-life	Decay mode	Production route	E (KeV)
$^{11}\text{C}^*$	20.4 m	$\beta^+$ (100 %)	$^{14}\text{N}(\text{p},\alpha)^{11}\text{C}$	981
$^{13}\text{N}^*$	10.0 m	$\beta^+$ (99 %)	$^{16}\text{O}(\text{p},\alpha)^{13}\text{N}$	1190
$^{15}\text{O}$	2.07 m	$\beta^+$ (100 %)	$^{15}\text{N}(\text{p},\text{n})^{15}\text{O}$	1723
$^{18}\text{F}$	109.8 m	$\beta^+$ (97 %)	$^{18}\text{O}(\text{p},\text{n})^{18}\text{F}$	634
$^{89}\text{Zr}$	78.1 h	$\epsilon\text{c}, \beta^+$ (23 %)	$^{89}\text{Y}(\text{p},\text{n})^{89}\text{Zr}$	900
$^{67}\text{Cu}$	62.01 h	$\beta^-$	$^{67}\text{Zn}(\text{n},\text{p})^{67}\text{Cu}$	577, 484, 395
<b><math>^{67}\text{Ga}</math></b>	<b>78.26 h</b>	$\gamma$	<b><math>^{67}\text{Zn}(\text{p},\text{n})^{67}\text{Ga}</math></b>	<b>91, 93, 185, 296, 388</b>
$^{123}\text{I}$	13.0 h	$\gamma$	$^{124}\text{Xe}(\text{p},2\text{n})^{123}\text{I}$	159
$^{111}\text{In}$	67.9 h	$\gamma$	$^{111}\text{Cd}(\text{p},\text{n})^{111}\text{In}$	247, 172

m= minutes; h= hours; when more than one different kind of energy is emitted, only those containing more than 11% abundance are listed (34, 48, 24). \*Despite these radionuclides have been reported in the literature for the investigation of labelled NPs, its half-life is too short for the majority of biomedical applications.

#### 1.3.4.1 Radiolabelling strategies

Different strategies can be applied for the preparation of radiolabelled NPs. The choice of the radioisotope to be used depends on many different factors, including the biological half-life of the NP under investigation, the imaging modality available, and the nature and composition of the NP, among others. Once the radioisotope has been selected, different labelling strategies might

be available; again, selection of the most appropriate procedure depends on the chemical properties of the NPs and other factors.

One of the most important factors to take into consideration is the half-life of the radioisotope to be used. The half-life should be sufficiently long to enable the investigation of PK parameters during the whole residence time of the NP within the organism (or at least the time-window of interest) and sufficiently short to minimize the radiation dose posed on the subject under investigation.

The decay mode is also paramount. In order to enable external detection of the radiation, gamma emitters or positron emitters (note that the emission of one positron results in the annihilation of the positron with a surrounding electron, resulting in the formation of two gamma rays) are required. Gamma rays have high penetration capacity and virtually no limit to tissue penetration; hence, the gamma rays can escape from the organism and be externally detected with the dedicated detectors incorporated into the imaging camera.

Finally, the chemical route to be used is also one of the key parameters to take into consideration. Not all NPs can be labelled, and depending on the chemical properties and surface decoration, one labelling strategy will be more appropriate compared to other.

For NPs devoted to biomedical applications, the preferred strategy is the incorporation of a radiometal *via* formation of a radiometal-chelator complex. This strategy requires previous attachment of the chelator (bifunctional chelating agent or BFCA) to the NP, usually achieved by covalent bonding. BFCAs are polydentate cyclic ligands where the donor atoms belong to the ring and/or to their pendant arms, which can efficiently bind a broad variety of bi- and trivalent metal ions and at the same time, be conjugated to a biologically active molecule (see Figure 7).

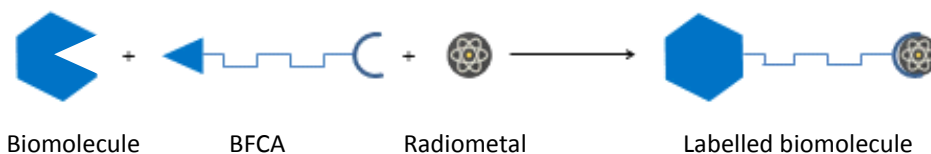


**Figure 7:** Schematic representation of the labelling strategy by means of bifunctional chelators.

As Figure 8 illustrates, BFCAs have three or four nitrogen atoms in their ring and external substituents such as carboxylates, phosphonates, thiols or amino groups that can react with functionalities present at the surface of the NPs.

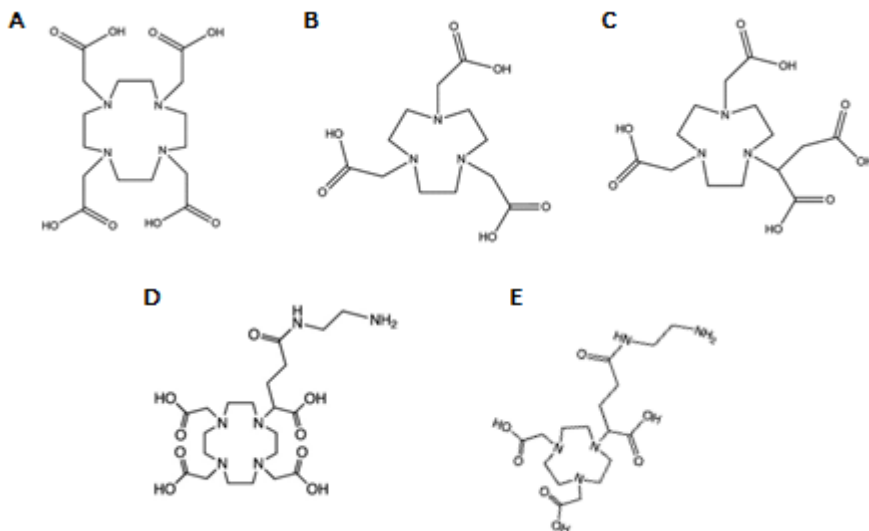


**Figure 8:** Examples of the ligands DOTA (A), NOTA (B) and NODAGA (C) derivatives. Adapted from reference (52) And NH<sub>2</sub>-DOTA-GA (D) and NH<sub>2</sub>-NODA-GA (E) chelators.

Different BFCAs based on 1,4,7,10-tetraazacyclododecane-1,4,7,10-tetraacetic acid (DOTA) and 1,4,7-triazacyclononane-triacetic acid (NOTA) have been developed and reported in the literature, including 2,2',2''-(10-(4-((2-aminoethyl)amino)-1-carboxy-4-oxobutyl)-1,4,7,10-tetraazacyclododecane-1,4,7-triyl)triacetic acid (NH<sub>2</sub>-DOTA-GA) or 2,2'-(7-(4-((2-aminoethyl)amino)-1-carboxy-4-oxobutyl)-1,4,7-triazonane-1,4-diyl)diacetic acid (NH<sub>2</sub>-NODA-GA). These enable the conjugation with the targeting molecule while preserving the BFCAs capability to stably chelate the radiometal. Currently, the development of novel BFCAs with improved chelating properties and enhanced stability are continuously being developed (53).

The main advantage of using BFCAs is that the formation of the radiometal-chelator complex takes place usually under mild conditions, preventing thus the decomposition of the NP. However, potential detachment of the radionuclide during *in vivo* studies can be expected, especially considering that strong chelating proteins are present in the blood. On the other hand, surface decoration may result in a modification of the surface properties of the NP. Consequently, this fact will have an effect in the biological activity. Hence, it is of paramount importance to investigate the effect of the radiolabelling on both the physico-chemical and biological properties of the NPs. Radioisotopes such as  $^{64}\text{Cu}$  (positron emitter, half-life= 12.8 h),  $^{67}\text{Ga}$  (gamma emitter,  $T_{1/2} = 78.26$  h) and  $^{99\text{m}}\text{Tc}$  (gamma emitter,  $T_{1/2} = 6.0$  h) have been used for the radiolabelling of NPs using this strategy (42,49).

If functional reactive groups are present in the surface of the NP, the use of a pre-labelled prosthetic group may constitute a valid alternative for the radiolabelling of NPs. This labelled precursor must contain a functional group suitable for conjugation to the surface of the NP by reaction with the reactive group present in there. A wide variety of prosthetic groups labelled with  $^{18}\text{F}$  and radioiodine have been successfully assayed as reported in the literature (37,54). The short half-life of  $^{18}\text{F}$  seriously limits the time-gap in which PK parameters can be investigated.

As previously mentioned, other radiolabelling strategies such as direct absorption of the radionuclide either at the core or on the surface of the NPs,

direct irradiation by neutron or ion beam or preparation of labelled precursors, which are incorporated into NPs during the preparation process have been described in the literature. Because these strategies are less appropriate in the context of biomedical applications, a detailed description will not be included here. For thorough revision, the reader is referred to recent reviews and one recently published book (55,56).

In the frame of this PhD thesis, the radioisotope of choice was  $^{67}\text{Ga}$ . Gallium can be found in nature consisting of two nonradioactive isotopes;  $^{69}\text{Ga}$  (60.108 % natural abundance) and  $^{71}\text{Ga}$  (39.892 % natural abundance) although 30 different gallium isotopes are known. The most interesting radioactive isotopes of gallium are the positron emitters  $^{66}\text{Ga}$  ( $T_{1/2} = 9.45$  h) and  $^{68}\text{Ga}$  ( $T_{1/2} = 67.84$  min) (57,58) and the gamma emitter  $^{67}\text{Ga}$  ( $T_{1/2} = 78$  h). These three radionuclides are widely used in the field of nuclear imaging.  $^{68}\text{Ga}$  is widely utilized due to its convenient availability from a  $^{68}\text{Ge}/^{68}\text{Ga}$  generator system, and has been employed for the evaluation of pulmonary, myocardial, cerebral, renal and hepatobiliary function, as well as tumour imaging. The main drawback when handling  $^{68}\text{Ga}$  for research purposes is that its short half-life severely limits long-term examinations.  $^{66}\text{Ga}$  is also a convenient radioisotope due to its longer half-life.

Gallium-67 is a gamma emitter with a long half-life (3.26 days), it decays to stable Zn by electron capture ( $\epsilon\text{c}$ ) and has no  $\beta$  emission. It can be produced in particle accelerators using different nuclear reactions, including



$^{67}\text{Zn}(p,n)^{67}\text{Ga}$ ,  $^{68}\text{Zn}(p,2n)^{67}\text{Ga}$ ,  $^{66}\text{Zn}(d,n)^{67}\text{Ga}$  and  $^{67}\text{Zn}(d,2n)^{67}\text{Ga}$ .  $^{67}\text{Ga}$  is usually separated from Zn (irradiated material) by ion exchange chromatography or by liquid extraction (59,60). Due to its long half-life, the radioisotope is usually supplied to end users at reasonable cost in citrate solution, which is widely used in the clinical setting.

Gallium-67 has been extensively used in the form of  $^{67}\text{Ga}$ -citrate as an imaging agent in SPECT for the detection of tumours (61) and inflammatory diseases (62,63). Currently,  $^{67}\text{Ga}$ -citrate is still a widely used radiopharmaceutical for the diagnosis of certain types of neoplasms as the capability of transferrin (TF) to bind  $\text{Ga}^{3+}$  is similar to iron-binding mechanisms (64,65).

Gallium-67 has been used for the preparation of labelled NPs. In one of the examples, (53) cobalt–ferrite nanoparticles surrounded by fluorescent rhodamine within a silica shell matrix were functionalized with the AS1411 aptamer. The resulting particles were further decorated with the bifunctional chelator p-SCN-bn-NOTA and labelled with  $^{67}\text{Ga}$ -citrate. The radiolabelling step was performed by incubation of the NPs with  $^{67}\text{Ga}$ -citrate under phosphate buffer (pH 6.5). Another example reported by Jalilian *et al.*, was meant to check the biodistribution profile of superparamagnetic iron oxide NPs (SPIONs) radiolabelled using  $^{67}\text{Ga}$ . In this case, the radioisotope was introduced during NP preparation (66). In the work reported by Shanehsazzadeh *et al.*,  $^{67}\text{Ga}$  was also employed to radiolabel SPIONs with

biodistribution purposes. However, the selected radiolabelling strategy was conducted using a cyclic-DTPA-dianhydride chelator (67). Very recently, a direct strategy for the labelling of magnetite and quantum dot-filled micelles using  $^{67}\text{Ga}$  was reported by a group of our institute (68). Magnetite based NPs (7 nm size) stabilized with oleic acid/oleylamine and 5 nm sized core-shell (CdSe-ZnS) quantum dots (QDs) stabilized with tri-n-octylphosphine oxide (TOPO)/stearic acid were treated with polyethylene glycol (PEG) phospholipids to yield stable, water soluble magnetite and QD-filled micelles, respectively. Micelles were incubated with  $^{67}\text{GaCl}_3$  to yield from 50 % to almost quantitative incorporation of the radiometal depending on the nature of the micelles.

Gallium's coordination numbers are 3, 4, 5 and 6. Six-coordinated complexes offering octahedral geometries are preferred as they saturate the sphere of gallium (69). Although these complexes are less prone to ligand exchange or hydrolysis, which would lead to transmetallation, (69) slightly deformed octahedral configurations have shown to be inert enough for use *in vivo* (52).

Two main classes of ligands are suitable for coordinating  $\text{Ga}^{3+}$ , which on the basis of their structural properties can be classified as linear ligands or macrocyclic ligands. The most widely used polydentate linear ligand with hard donor groups is diethylenetriaminepentaacetic acid (DTPA); NOTA and DOTA chelators are the most commonly used cyclic chelators (40,69). Ga-NOTA has demonstrated to be more stable ( $\log K = 30.98$ ) (70,71) than Ga-

DOTA ( $\log K = 21.33$ ), due to the cavity hole in which the small  $\text{Ga}^{3+}$  metal ion fits perfectly (72–75). Moreover, despite DOTA is within the composition of several FDA approved agents, the formation of the complex with the radiometal requires higher temperatures and has an affinity constant comparable to that of transferrin with  $\text{Fe}^{3+}$  ( $\log K = 20.3$ ), which could be detrimental (76–79).

#### *1.3.4.2 Radiochemical stability of radiolabelled nanoparticles*

Radiolabelling followed by nuclear imaging is a convenient tool for the determination of pharmacokinetic properties of NPs. Noteworthy, a crucial aspect to guarantee reliable data is the stability of the radiolabel once it has been administered into the subject under investigation. If detachment of the radioisotope or metabolism occurs during imaging studies, the distribution of the *in situ* generated labelled species might significantly differ from that of the parent compound, leading to misinterpretation of the results or a decrease in the signal-to-noise ratio.

The *in vivo* instability of radiolabelled NPs, which may result in detachment of the radionuclide, can have a significant impact on the conclusions obtained from imaging studies. Hence, a key step in the evaluation of radiolabelled NPs is the investigation of their *in vivo* stability. When dealing with small molecules, assessment of such stability usually requires blood sampling and processing. Sample processing typically encompasses the isolation of the

plasma by centrifugation, and subsequent analysis using instrumental analytical techniques such as high performance liquid chromatography (HPLC) with radiometric detection or (instant) thin layer chromatography (iTLC/TLC). When dealing with macromolecules such as proteins or antibodies, size exclusion chromatography (SEC) or gel electrophoresis are often used. Despite the identification of the radioactive metabolites or detached radiolabelled species is frequently very challenging, the percentage of the radioactivity that is present as the parent compound can be determined. In principle, blood sampling followed by isolation of the plasma and further analysis can be anticipated as a suitable strategy for the assessment of the stability of radiolabelled NPs. However, three main drawbacks require careful consideration: (i) NPs are not easily isolated from blood samples; (ii) NPs usually have long residence time in the body. When using the appropriate radioisotopes, imaging studies can thus prolong over days or even weeks; in this scenario, radiochemical stability has to be assessed at least during a time gap equivalent to the duration of the imaging studies; and (iii) the stability of the NPs themselves is very difficult to determine.

The simplest way to measure radiochemical integrity consists of incubation of the labelled NPs with a selected media, followed by separation by centrifugation of the NPs and determination of the amount of radioactivity in the different fractions (pellet and supernatant) (25,80,81). This method has one main drawback: all the radioactivity present in the pellet will be

considered as “labelled NPs”, while all the radioactivity in the supernatant will be considered as “(unidentified) soluble species” that have detached from the NPs. Of note, no information about the chemical nature of the soluble species or the aggregation state/stability of the NPs will be obtained; the latter can be solved by subsequent analysis of the pellet using techniques such as transmission electron microscopy (TEM), scanning transmission microscopy (SEM) or dynamic light scattering (DLS). However, such equipment is usually located out of radiation controlled facilities and hence complete decay of the radioactivity is required before processing.

Chromatographic techniques, sometimes combined with the above mentioned centrifugation/filtration strategy, are often used to determine the radiochemical integrity of labelled NPs *in vitro* (82–85). Noteworthy, chromatographic methods applied to the determination of the radiochemical integrity of NPs require careful validation (or determination of their suitability to perform the desired analysis) before being applied, as unexpected drawbacks might appear. For example, stationary phases used in TLC/ITLC have reactive properties that may lead to the destruction or alteration of the NPs during analysis. Our research group has realized that <sup>67</sup>Ga-labelled polymeric NPs may not be stable in contact with silica plates, leading to a progressive detachment of the radionuclide; this led to a curious result: NPs integrity depended on the time gap between seeding the sample in the TLC plate and eluting with the solvent (unpublished results). On the other hand, NPs may aggregate in certain environments; if the aggregates reach a certain

size, they may get stuck into the column when applying HPLC or SEC. These and other factors might lead to inconclusive results or data misinterpretation.

Most of the stability studies included in the works referred above are based on the incubation of the NPs with saline solution, buffers or plasma. The use of plasma as incubation media for the evaluation of radiochemical integrity implies the presence of proteins, and its use is especially relevant in those cases in which NPs are labelled by taking advantage of the formation of metal complexes, because proteins can act as competitors leading to transchelation. Alternatively to the use of plasma, solutions containing artificially added competitors, which are usually complexing agents that can sequester the radiometal by transchelation, can be used. For example, multidentate bifunctional chelators are commonly utilized to yield stable complexes with radioisotopes such as  $^{67}\text{Ga}$  or  $^{68}\text{Ga}$ , among others. Once in contact with blood, gallium ions, (which have similar properties to iron) can be chelated by porphyrins or to the iron transporter protein Apo-transferrine. Apo-transferrine is a commercially available protein and can thus be used to simulate the chelation of radiometals to plasma proteins, mimicking *in vivo* conditions. Another approach would consist of incubating the radiolabelled NPs with simple chelators such as citrate, DOTA, NOTA or DTPA, since these chelators readily form a complex with the radiometal at moderate temperature. The same rationale can be applied to, for example,

NPs labelled with  $^{99m}\text{Tc}$ , which can be incubated in the presence of cysteine as a competitor (86).

Incubation of the NPs with solutions containing competitors similar to those ones found in the blood or tissues is a good strategy to estimate the radiochemical integrity of the NPs *in vivo*; however, the presence of blood cells is completely neglected in such approach. In principle, radioactivity in the blood is distributed between blood cells and plasma, because radioactive particles can be either cell-bound or freely suspended in plasma. Hence, it might be interesting to investigate the percentage of NPs that will remain attached to the blood cells and the amount of particles that will remain in the plasma. From the plasma, it is also convenient to investigate the fraction of the radioactivity that has been detached from the NPs. This problem can be solved by performing experiments based on the incubation of labelled NPs in blood (87).

*In vivo*, the determination of the stability of the labelled NPs is even more challenging, as it requires blood sampling and processing. Especially when working with small animals (*e.g.* mice) the blood sampling is limited to a few tens of  $\mu\text{L}$  unless sacrifice by exsanguination is carried out. Hence, analytical methods should be efficient, robust and require as less amount of blood as possible. Only a few examples reporting *in vivo* radiochemical stability of NPs have been published in the scientific literature (88,89).

Alternatively to withdrawal of blood samples and subsequent analysis, “indirect” methods for the qualitative determination of the *in vivo* radiochemical integrity of labelled NPs can be employed. These usually consist in administering both the labelled NP and the labelling agent (*i.e.*, the “free” radionuclide) and comparing the biodistribution profiles. Differences in biodistribution are usually accepted as an indirect proof of radiolabelled NP stability. Noteworthy, indirect methods provide only an estimation of the radiochemical integrity of NPs *in vivo* and the results should be carefully considered. The methods rely on the direct comparison of the biodistribution patterns of different chemical entities; however, if the detached radiolabelled specie has a distribution pattern similar to that of the parent labelled NPs, complete erroneous conclusion would be derived from the studies.

Very recently, multi-labelling of NPs and individual tracking of the different radioisotopes has proven efficient in the determination of *in vivo* radiochemical stability of NPs (90). This might be a very useful tool for future investigation of novel engineered NPs.

In the context of this PhD, the centrifugation method followed by gamma counting has been used for the determination of the radiochemical integrity of the radiolabelled NPs.



## 2. MOTIVATION AND OBJECTIVES OF THE THESIS



## 2.1 JUSTIFICATION OF THE STUDY: THE SAVE ME PROJECT

An estimated 3.2 million new cancer cases and 1.7 million deaths per year in Europe define cancer as a crucial public health problem. Among all cancer types, pancreatic cancer is the fourth deadliest cancer cause. The overall five-year survival rate is less than 5 % and thus, quick and effective actions need to be taken to develop novel diagnostic and therapeutic tools.

The Save Me project was a collaborative work funded by the European Commission under the FP7 NMP Theme (No. CP-IP 263307 grant) (91). The aim of the project was to investigate novel modular nanosystem platforms integrating advanced functionalized nano-core particles and active agents for pancreatic cancer diagnosis and treatment. By exploiting the partners' research expertise, the designed platforms had to be based on biocompatible polymeric core NPs with selective active agents in their surface for tumour targeting and penetration.

The consortium as a whole included 21 partners from 7 member states (Germany, UK, Sweden, Belgium, Spain, Austria and Italy) one Associated State (Israel) and one International Cooperation Partner Country (ICPC) (Russia) coming from different scientific and technological disciplines. Five of the partners, namely Bar-Ilan University (Israel), CIDETEC (Spain), Goethe University (Germany), Nanosystems (Russia) and the University of Bologna (Italy), were devoted to the preparation of core nanoparticles and

incorporation of targeting agents, stabilizers and further decorations to improve blood circulation, tissue penetration and cell internalization. Hence, all nanomaterials investigated in the context of this PhD were synthesized, characterized and provided by the above-mentioned partners.

The role of CIC biomaGUNE in the project was the assessment of the suitability of the multi-decorated nanosystems provided by associated partners as potential therapeutic or diagnostic tools for pancreatic cancer, using a combination of *in vivo* imaging modalities. As initially planned in the project proposal, evaluation should be conducted using Magnetic Resonance Imaging and Nuclear Imaging, opportunistically in combination with other imaging modalities such as CT.

The piece of work included in this PhD comprises radiolabelling of the nanosystems, the assessment of radiochemical integrity, the development of an animal tumour model and the evaluation of the nanosystems using *in vivo* nuclear imaging, mainly SPECT in combination with CT.

In the first part of the work, radiolabelling of nanoparticles from all five partners was approached and the accumulation in the tumour was evaluated using a reduced number of animals. This first fast screening was aimed at selecting the most promising NP cores and targeting moieties in order to tackle, in a second step, more accurate studies with the selected particles, using a higher number of animals and with potential refinement of the

properties of the NPs. In this context, the initial efforts in developing the right nanosystems by the different Save Me partners, including a full description of the systems, the radiolabelling reactions with the gamma emitter  $^{67}\text{Ga}$  (including optimization of the experimental conditions and assessment of radiochemical integrity), as well as the implementation of the animal tumour model for the *in vivo* tests with the different NPs are described in Chapter 3. The SPECT-CT experiments conducted, the quantification methods employed and the results of the first screening are also described in this chapter.

After the first screening, the most promising NP cores and targeting moieties were selected and submitted to more thorough evaluation. With the aim of improving blood circulation time, tissue penetration capability and cell internalization, further decoration based on PEG chains containing a substrate for matrix metalloproteinase 9 (MMP9) were incorporated into the most promising NPs. Radiolabelling of the NPs with  $^{67}\text{Ga}$  followed by SPECT-CT studies were conducted and the results are reported in chapter 4.

## 2.2 OBJECTIVES

Within the context of the Save Me project, the general objective of the work conducted in the frame of this PhD thesis was to develop strategies for the radiolabelling of the different NPs provided by the Save Me partners and evaluate their capability to accumulate in the tumour using an animal model of pancreatic adenocarcinoma and a combination of imaging modalities. To achieve this general objective, the following specific objectives were defined:

1. Development of radiolabelling strategies for the incorporation of  $^{67}\text{Ga}$  into NPs provided by other partners involved in the consortium.
2. Optimization of the transformation procedure of  $^{67}\text{Ga}$  citrate into  $^{67}\text{Ga}$  chloride based on previously reported methods.
3. Efficient purification procedure of free  $^{67}\text{Ga}$  species from radiolabelled NPs.
4. Determination of the radiochemical stability of the labelled NPs trying to simulate *in vivo* conditions.
5. Implementation of a subcutaneous (SC) mouse tumour model of human pancreatic adenocarcinoma.
6. Evaluation of the PK properties and tumour accumulation of  $^{67}\text{Ga}$ -labelled NPs with different cores and targeting moieties, using a combination of *in vivo* imaging modalities during a longitudinal follow-up; selection of the most appropriate candidate/s for further investigation.

7. Statistical comparisons of different compounds regarding tumour accumulation.
8. *In vivo* evaluation of the PK properties and tumour accumulation capacity of the most promising candidates longitudinally, using different targeting moieties and PEG-based decorations to improve blood circulation time and internalization capacity





**3. FIRST *IN VIVO* SCREENING:  
SELECTION OF MOST APPROPRIATE NP  
CORE AND TARGETING MOIETY**



### 3.1 INTRODUCTION

As already mentioned, the Save Me consortium was integrated by more than 20 partners; five of them were dedicated to the preparation of targeted nanosystems with different cores, although only four could be used for radiolabelling and *in vivo* studies. Besides that, two partners, *i.e.* SHEBA medical center and Universitäts Klinikum group in Heidelberg (UKH) were developing novel tumour targeting agents: somatostatin analogues (PTRs) and tPA, respectively, and performing *in vitro* studies in order to select those candidates showing better affinity towards their specific receptors (SSTRs and Galectine-1). The most promising targeting moieties within each category were attached to the different NPs; hence, each partner was anticipated to provide 3 different particles: the core particles without targeting moiety and the same particles functionalized with the most promising PTR and tPA targeting moieties.

In this scenario, the first job to be conducted at CIC consisted of determining, among the 12 particles provided, which were the ones resulting in better tumour accumulation and optimal pharmacokinetic properties. Because the resources were limited, this initial investigation was carried out in 2 animals per NP.

Some of the NPs provided by the partners could be directly imaged using magnetic resonance imaging, as they contained small iron oxide NPs trapped

into the polymeric core. However, nuclear imaging was anticipated as the optimal tool to gain information regarding the PK properties of the NPs: first, the images can be directly quantified, and consequently the absolute amount of NPs accumulated in the tumour after administration might be obtained; second, nuclear imaging overcomes one of the major limitations of MRI, *i.e.*, the poor sensitivity. Because the biological half-life of the NPs was anticipated to be long (from days to weeks) the choice of the radionuclide for the radiolabelling was quite restricted. Taking into consideration the available tools during project execution,  $^{67}\text{Ga}$  was selected as the optimal radionuclide, as it has a relatively long half-life and excellent emission properties for its detection using SPECT.

Within this context, the first task was to set up the experimental conditions for the radiolabelling of all the NPs provided by the different partners. In parallel, the animal tumour model was implemented, with the aid of the animal facility staff and in collaboration with personnel in the MRI department. Of note, the tumour growth curve was a key factor; an appropriate growth curve enabling proper execution of the imaging studies was required, and hence different numbers of cells were inoculated into a number of animals to obtain the optimal experimental conditions. After having established the animal tumour model, *in vivo* experiments using SPECT-CT were initiated. MRI studies were also carried out with selected animals and the results obtained with both modalities were combined when

possible, to get advantage of the impressive resolution of MRI and the unparalleled sensitivity of nuclear imaging.

## 3.2 MATERIALS AND METHODS

Most of the NPs were designed to contain a superparamagnetic maghemite core as starting material, surrounded by diverse polymeric matrices. Functional groups such as COOH, CHO, NH<sub>2</sub>, SH, and/or OH located on the surface of the polymeric matrices allowed further attachment of targeting moieties. Moreover, the core nanoparticles were engineered to be stable in acidic aqueous media (pH 5.0) to allow the radiolabelling *via* chelators, which were anchored to the NP surface also at the production sites.

Most of the nanoparticle producers opted for a DOTA-like chelator. Moreover, as mentioned in previous sections, the developed nanosystems included a targeting moiety for pancreatic cells. Endogenous SST and tPA have a short biological half-life and hence new analogues were synthesized. Despite this work was not carried out at CIC biomaGUNE, a brief description of the preparation method for both targeting moieties and the different NPs are provided below for clarity.

### 3.2.1 SYNTHESIS OF TARGETING MOIETIES

#### 3.2.1.1 Synthesis of SST analogues

The preparation of SST analogues (namely, PTRs) was carried out by DeveloGen Ltd. (now named as Evotec AG, Gottingen, Germany) using standard Fmoc solid phase peptide synthesis (SPPS), based on backbone cyclization *via* the carbon or nitrogen atoms without interfering with side chains.

The developed peptide chain sequence was covalently bound to fluorescein isothiocyanate (FITC) fluorescein moiety *via*  $\gamma$ -aminobutyric acid (GABA) in Tel-Aviv University (TAU) (see Figure 9), following a previously reported method by Gazal *et al.* (92) creating the disulfide-bridged backbone cyclic somatostatin analogue PTR<sub>3207-86</sub>, which will be referred throughout the thesis as PTR<sub>86</sub>.

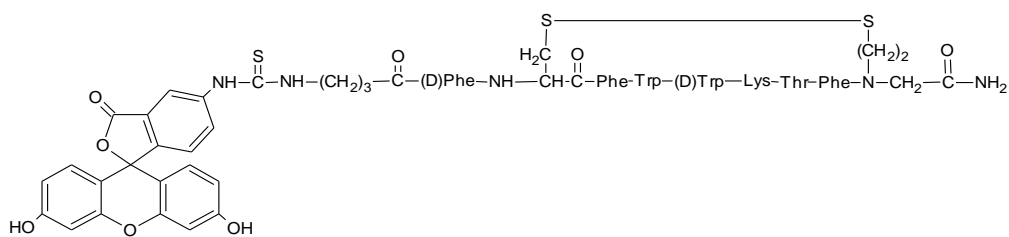


**Figure 9:** PTR<sub>3207-86</sub>-GABA-FITC amino acid's sequence and structure. MW: 1753 g/mol. Reprinted with permission of TAU partner.

### 3.2.1.2 Synthesis of tPA analogues

The design of tPA analogues was carried out by UKH, while the synthesis and purification of the selected amino acid sequences were executed at the Peptide Specialty Laboratories (PSL) GmbH Company (<http://www.peptid.de>), Heidelberg, Germany.

The entire tPA sequence is constituted by 562 amino acids; this protein has a limited half-life time. In order to improve PK properties, a fraction of the entire amino acid sequence was selected (aa 137-164) and synthesized with slight modifications with respect to the original sequence (see Figure 10).

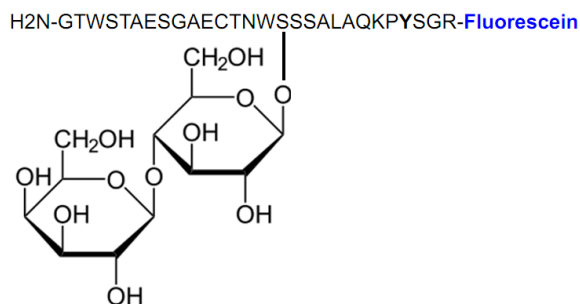


**Figure 10:** tPA-1 targeting moiety with a Serine- $\gamma$ -D-lactose peptide sequence and FITC fluorescent agent. Reprinted with permission of UKH partner.

In the Figure above, the R side chain is a lysine linked to fluorescein and the G side chain has a *N*-terminal amino group, which was used for covalent linkage to the NPs. Additionally, the aa in position 152 (asparagine) was substituted by a serine, which was bound to a lactose molecule, a disaccharide known to interact with galectins.



The above sequence (tPA-1) showed 20-fold higher binding to Gal-1 receptor, compared to the native tPA protein (93).

### 3.2.2 SYNTHESIS OF NANOPARTICLES

#### 3.2.2.1 *Bar-Ilan University*

The Bar-Ilan University (BIU) from Ramat Gan in Israel designed and synthesized PAMAM<sub>inj</sub>-CAN-Maghemite ( $\gamma$ -Fe<sub>2</sub>O<sub>3</sub>) based NPs under the supervision of Professor Jean-Paul Lellouche.

Starting with the oxidation of magnetite to maghemite, NPs were stabilized with cerium ammonium nitrate (CAN) forming stable colloidal water dispersions due to electrostatic repulsive interactions. The CAN-Maghemite core was self-assembled with polyamidoamide (PAMAM) dendrimers through an ultrasound-assisted nanofabrication process (referred as “inj”, which stands for injection). The NPs were coated with a hydrophobic organic ligand (ethyl 12-((3,4-dihydroxyphenethyl)amino)-12-oxododecanoate) designed to confer hydrophobicity to the iron oxide NPs. The ligand possesses a catechol unit at one end, (which presents strong affinity to iron due to both the  $\sigma$  and  $\pi$  donor power of oxygen atoms), a central aliphatic chain and a terminal ester group. These stabilized NPs were encapsulated in a poly(D,L-lactide-co-glycolide)-block-polyethyleneglycol copolymer (PLGA-b-

PEG-COOH) to provide solubility in water and potential improvement of the residence time in the bloodstream.

A PEG corona bearing carboxylic acid groups was attached to the surface of the NPs to partially avoid the sequestration of the NPs by the reticuloendothelial system (RES) organs *in vivo*. The carboxylic acids were subsequently used for the incorporation of the targeting moieties. This was achieved by activation with 1-ethyl-3-(3-dimethylaminopropyl) carbodiimide (EDC) in water and further amidation reaction with the *N*-terminus of PTR<sub>86</sub> and the tPA analogue. Finally, the particles were purified with a centrifugal filter device (94). In order to know the amount of targeting moieties (PTR<sub>86</sub> and tPA) covalently attached to the NPs, the free amino functions present in solution were quantified first using a Kaiser test before and after covalent linkage to the NPs. Then, the same molar amounts of the peptides were attached covalently onto the NPs surface.

All nanostructures were positively charged and had an average particle size between 100 and 150 nm according to DLS measurements, while core diameter was around 40 nm. The total iron concentration (measured by ICP) of the bare NPs was 1.7 mg/ml whereas the concentration of targeting moiety was 0.79 mg/ml for NPs decorated with PTR<sub>86</sub> and 0.85 mg/ml for NPs decorated with tPA.

### 3.2.2.2 *Goethe University*

The second NP type was synthesized in the Department of Biochemistry, Chemistry and Pharmaceutical Science of the Goethe-Universität (GU) from Frankfurt am Main in Germany. CAN maghemite NPs with recombinant human serum albumin (rHSA) were designed and synthesized under the supervision of Professor Jörg Kreuter. A 1,4,7,10-tetraazacyclododecane-1,4,7,10-tetraacetic-NHS ester (DOTA-NHS) chelator (CheMatech, Dijon, France) was attached to the NPs at a concentration of  $0.49 \pm 0.012$  mg/mg NP. PTR<sub>86</sub>-FITC and tPA moieties were also anchored to the NP surface *via* EDC chemistry (94). The NPs had a size range of 160-190 nm, as measured by DLS using a Zetasizer Malvern Nano ZS (Malvern Instruments Ltd., Malvern, UK). The iron concentration was 1 µg of iron / 1 mg protein. After production, the nanoparticles were purified by centrifugation and gel-permeation chromatography.

### 3.2.2.3 *University of Bologna*

The third NP investigated in the context of this PhD thesis was prepared at the Department of Chemistry from the University of Bologna (UNIBO) in Italy under the supervision of Professor Mauro Comes Franchini. Maghemite-loaded PLGA-b-PEG-COOH NPs were produced by co-nanoprecipitation of the poly(D,L-lactide-co-glycolide)-b-polyethyleneglycol polymer with an hydrophobic ligand-coated magnetic maghemite core. Thereafter, NODA

bifunctional chelator was coupled to the outer shell by EDC/NHS linkage, keeping the solution under stirring overnight and resulting in negatively charged NPs. The resulting NPs were further functionalized with PTR<sub>86</sub> or tPA.

#### 3.2.2.4 CIDETEC-IK4

CIDETEC-IK4 (CID), located in San Sebastian, Spain, prepared polymeric NPs under the supervision of Dr. Iraida Loinaz. This group followed a different strategy to produce their nanosystems, as no CAN-maghemite core was utilized. Starting from a linear polymethacrylic acid (PMAAc) deprotected copolymer and alkyloxyamine-derivative reactive monomers; intramolecular chain collapse was forced by continuous addition of a dialdehyde containing diethylenetriaminepentaacetic acid (DTPA cross-linker creating the so-called single chain polymeric nanoparticles (SCPNs)). This synthetic procedure was described in an article published by M.K. Aiertza *et al.* (95). The core SCPNs were negatively charged (zeta potential = -32 mV), around 45 nm in size and visually homogeneous by TEM. Moreover, by proton nuclear magnetic resonance (<sup>1</sup>H-NMR) the different bands corresponding to the polymeric chains were identified. This core system was the starting point for the production of targeted SCPNs. In all cases, NPs were functionalized with NH<sub>2</sub>-DOTA-GA (MW: 518.56 g/mol) purchased at CheMatech. Attachment of the functionalities was approached by activation of the carboxylic acid groups available at the surface of the NPs using 4-(4,6-dimethoxy-1,3,5-

triazin-2-yl)-4-methylmorpholinium (DMTMM), and subsequent amide coupling (see Figure 11). The final NPs were purified by dialysis.

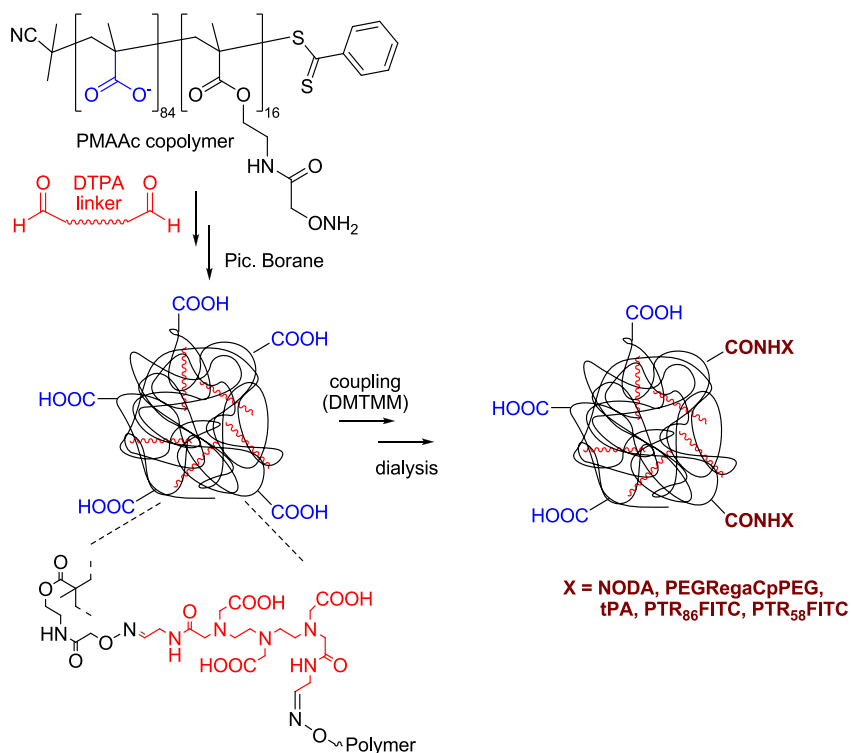


**Figure 11:** Synthetic process of SCPNs, in which X stands for any BFCA or targeting or penetrating agent. Reprinted with permission of CID partner.

The main characteristics of the NPs provided by the partners are summarized in Table 4.

FIRST *IN VIVO* SCREENING: SELECTION OF MOST APPROPRIATE NP CORE AND TARGETING MOIETY

**Table 4:** Composition, functionalization, size, polydispersity index (PDI) and zeta-potential of the NPs.

Partner ID & NP code	Core composition	Functionalization: BFCA / targeting moiety	Size (nm) (n=3)	PDI and Z potential
CID-01	PMAAc based SCPNs	NH <sub>2</sub> -DOTA-GA [18 % w/w]	75	PDI: 0.3
CID-02	PMAAc based SCPNs	NH <sub>2</sub> -DOTA-GA [N/A*] PTR <sub>86</sub> -FITC [0.7 % w/w]	148	PDI: 0.4
CID-03	PMAAc based SCPNs	NH <sub>2</sub> -DOTA-GA [N/A*] tPA-FITC [0.26 % w/w]	193	PDI: 0.2
BIU-01	PAMAM <sub>inj</sub> -CAN-Fe <sub>3</sub> O <sub>4</sub>	None	34	ζ pot: 53.5 mV
BIU-02	PAMAM <sub>inj</sub> -CAN-Fe <sub>3</sub> O <sub>4</sub>	PTR <sub>86</sub> -FITC [46 μg/ml]	144	ζ pot: 43.8 mV
BIU-03	PAMAM <sub>inj</sub> -CAN-Fe <sub>3</sub> O <sub>4</sub>	tPA-FITC [110 μg/ml]	100	ζ pot: 41.8 mV
UNIBO-01	PEG-PLGA-Fe <sub>3</sub> O <sub>4</sub>	NODA [0.8 mM]	154 ± 2	ζ pot: -10.5 PDI: 0.28 ± 0.09
UNIBO-02	PEG-PLGA-Fe <sub>3</sub> O <sub>4</sub>	NODA [1.05 mM] PTR <sub>86</sub> -FITC [57 μM]	90 ± 2	ζ pot: -38.2
UNIBO-03	PEG-PLGA-Fe <sub>3</sub> O <sub>4</sub>	NODA [1.1 mM] tPA-FITC [33 μM]	95 ± 1	ζ pot: -37.8 PDI: 0.20 ± 0.006
GU-01	CAN-Fe <sub>3</sub> O <sub>4</sub> -rHSA	DOTA-NHS [0.49 ± 0.012 mg/mg NP]	174 ± 6	ζ pot: 16.5 ± 2 PDI: 0.106 ± 0.022
GU-02	CAN-Fe <sub>3</sub> O <sub>4</sub> -rHSA	DOTA-NHS [N/A*] PTR <sub>86</sub> -FITC [N/A*]	164 ± 4	ζ pot: 17.1 ± 2.2 PDI: 0.088 ± 0.022
GU-03	CAN-Fe <sub>3</sub> O <sub>4</sub> -rHSA	DOTA-NHS [0.49 ± 0.012 mg/mg NP] tPA[7.56 ± 0.02 mg/mg NP]	181 ± 14	ζ pot: 21.4 ± 1.5 PDI: 0.132 ± 0.042

\* N/A: Information not provided by the supplier.

### 3.2.3 RADIOLABELLING OF NANOPARTICLES

#### 3.2.3.1 Purification of $^{67}\text{Ga}$

Galium-67 is generally produced in a cyclotron by the  $^{68}\text{Zn}(p, 2n)^{67}\text{Ga}$  reaction *via* irradiation of a zinc target (enriched or natural) with a determined proton energy (MeV), although other production methods have also been described (59). The  $^{67}\text{Ga}$  is then separated from the  $^{67}\text{Zn}$  target by chemical synthesis (96).

In the context of the current PhD thesis,  $^{67}\text{Ga}$  was obtained from Cis Bio International (Gif-sur-Yvette, France) or Mallinckrodt Medical, B.V. (Le Petten, The Netherlands). It was supplied as citrate salt at a pH between 6.5 and 7.5, as pharmaceutical formulation. However, gallium citrate has shown a low labelling efficiency in chelation reactions. This is the reason why prior to labelling reactions,  $^{67}\text{Ga}$  citrate was converted to  $^{67}\text{Ga}$  chloride using a solid-phase extraction (SPE) method following a protocol described by I. Vergara *et al.*, (97) based on the method described by Chang and Gonda (98) with slight modifications.

In a first step, the complete citrate solution was eluted through two silica cartridges (Sep-Pak<sup>®</sup>, WAT023537, Waters Co., Milford, MA, USA) connected in series, containing 120 mg of silica each with a pore size of 125Å, using a syringe pump (11 plus Syringe Pump, Harvard apparatus, Strategic Applications Inc.) at a constant flux rate of 0.1 ml/min. The cartridges were

not conditioned previous to elution. Gallium ions from the solution were retained in the silica cartridges and the residual fraction was collected into a waste vial (vial A). After flushing the cartridges with dry air, the activity in the columns and vial A was measured in a dose calibrator (26 x 6 cm ionization chamber, CPCRC-25R, Capintec Inc., NJ, USA). In a second step, the cartridges were washed with ultrapure water (5 mL) obtained from a Milli-Q® Purification System (Millipore®, Merck KGaA, Darmstadt, Germany) at a flux of 3 ml/min in order to rinse the remaining citrate. The eluted liquid was collected in a second vial (vial B), and the amount of radioactivity in the columns and the vial were again measured. Finally, desorption of gallium ions from the silica was conducted by elution with 0.1 M HCl (1 ml) prepared by dilution of HCl<sub>30%</sub> (Suprapur®, Merck kGaA, Darmstadt, Germany) using a syringe pump at a flux of 0.1 ml/min. The eluate was collected in 10 different fractions (ca. 100 µL/fraction) into 1.5 ml volume micro test polypropylene tubes (Eppendorf AG, Hamburg, Germany). The amount of radioactivity in each fraction was measured in a dose calibrator, and those containing the maximum activity concentration were used in subsequent labelling experiments. A conceptual flow sheet of the system is presented in Figure 12.



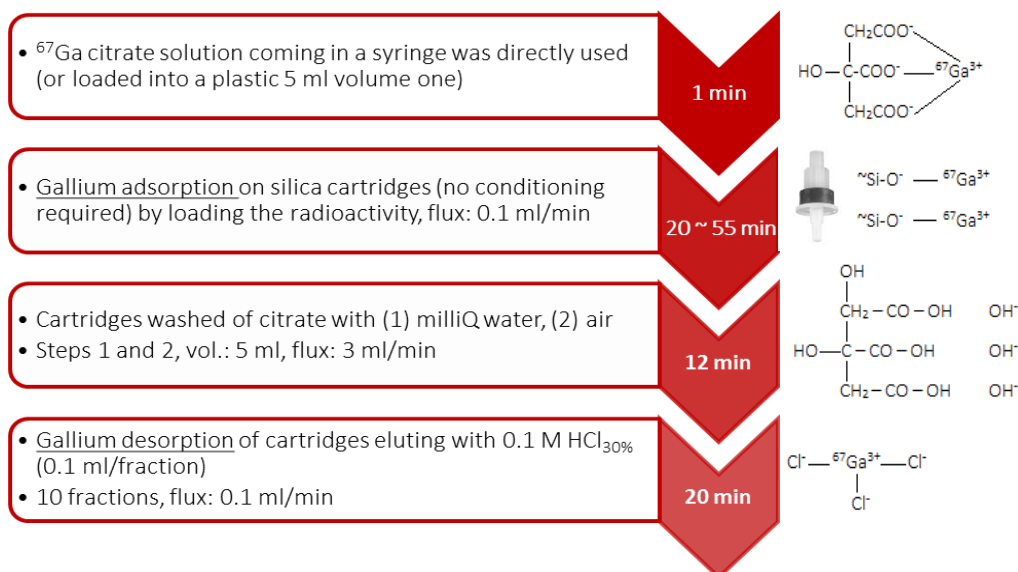


Figure 12: Flowchart of the conversion procedure of  $^{67}\text{Ga}$  citrate into  $^{67}\text{Ga}$  chloride.

### 3.2.3.2 Radiolabelling and purification of NPs

Following the ALARA criteria (*as low as reasonably achievable*) maximization of the distance between the operator and the radioactive source ( $^{67}\text{Ga}$ ), minimization of the handled dose and use of appropriate shielding units were applied. Radioactive sources were always handled in hot cells (see Figure 13). The handled doses were over 370 MBq when animal experiments had to be conducted; however, low amounts of radioactivity (*ca.* 0.7-3.7 MBq) were used during optimization of experimental conditions.

For the radiolabelling reactions, ultrapure water was obtained from a Milli-Q® Purification System as previously mentioned and used to prepare all

aqueous solutions. Radiolabelling of NPs was performed by incubation of the NPs with a solution of  $^{67}\text{GaCl}_3$ . Briefly, 200  $\mu\text{L}$  of a 0.2 M sodium acetate buffer solution (S2889-250G, Sigma-Aldrich Química S.L., Madrid, Spain) acidified with acetic acid (ReagentPlus<sup>®</sup>  $\geq 99\%$ , Sigma-Aldrich Química S.L., Madrid, Spain) at a pH value of 3.8, 50  $\mu\text{L}$  of NP solution (1 mg/ml) and 100  $\mu\text{L}$   $^{67}\text{GaCl}_3$  were mixed together. Sodium acetate was used as buffering agent. When required, sodium hydroxide 0.1 M (prepared from 1 M solution, Panreac Química S.L.U., Catalonia, Spain) filtered on 0.22  $\mu\text{m}$  polyethersulfone (PES) membrane filters (Thermo Fischer Scientific Inc., MA, USA) was used to adjust the pH values after addition of the  $^{67}\text{GaCl}$  solution.



**Figure 13:** Hot cell installed in the Molecular Imaging Unit of CIC biomaGUNE.

The mixture was incubated at room temperature (25 °C, RT), or heated into a temperature-controlled heating block (SBH130D model, Stuart Group Ltd.). After incubation, the crude material was purified by centrifugal filtration using a centrifuge (Nahita 2507/100, Auxilab S.L., Navarra, Spain) and Millipore filters (100 kDa cut-off, Amicon® Ultra 0.5 ml UFC510096, Molsheim, France). After centrifugation the resulting precipitate was washed three times with acetate buffered solution (pH 3.8) to remove unreacted <sup>67</sup>Ga species. Thereafter, the amount of radioactivity in the pellet, the supernatant and the washings were determined in a dose calibrator. Radiolabelling efficiency (RE, expressed in percentage) was calculated using equation 1 and referred throughout the thesis as radiochemical conversion value (RCC):

$$\text{Equation 1:} \quad \text{R.E. \%} = A_{\text{filter}} / (A_{\text{filter}} + A_{\text{filtrates}}) * 100$$

Where  $A_{\text{filter}}$  is the amount of radioactivity in the filter, and  $A_{\text{filtrates}}$  is the amount of radioactivity in the filtrates, including washings. Finally, NPs in the filter were suspended in 200  $\mu$ L of saline solution (0.9% NaCl, Braun Medical S.A., Catalonia, Spain), recovered in a syringe and the amount of radioactivity was measured in a dose calibrator. Radiochemical yield was calculated using equation 2:

$$\text{Equation 2:} \quad \text{R.Y. \%} = A_{\text{rf}} / A_{\text{t}} * 100$$

Where  $A_{rf}$  is the amount of radioactivity in the resuspended fraction, and  $A_t$  is the starting amount of radioactivity.

### 3.2.3.3 *Radiochemical integrity of NPs*

*In vitro* radiochemical integrity of the labelled NPs was assessed by means of the centrifugation technique. Briefly, NPs were prepared and purified as described in section 3.2.3.2 and subsequently suspended in 250  $\mu$ L of physiologic NaCl 0.9 % solution (Braun Medical S.A.). The suspensions were then divided into 4 different fractions and mixed with a solution of DOTA (final concentration = 32  $\mu$ M) purchased to Macrocyclics Inc, which acted as a high interacting competitor towards  $^{67}\text{Ga}$ . The aliquots were kept at 37 °C for 1, 3, 24 and 48 hours respectively using a digital block heater. The samples were then filtered and radioactivity in the filter (supernatant) and the filtrate (pellet) measured in a 2470 WIZARD<sup>2</sup> Automatic Gamma Counter. Finally, the radiochemical integrity was calculated as the percentage of radioactivity in the supernatant with respect to the total amount of radioactivity (pellet + supernatant).

### 3.2.3.4 *Dose preparation*

The preparation of the radioactive doses was carried out by diluting the radiolabelled nanoparticles in 200  $\mu$ L of saline solution (0.9 %). The injected dose was always below the permitted limit in animal experiments, according to the species and administration route (10 ml/Kg) (99,100).

### 3.2.4 IMAGING STUDIES

#### 3.2.4.1 *Animal model: Athymic Nude Mice*

##### General considerations:

Animals were maintained and handled in accordance with the Guidelines for Accommodation and Care of Animals (European Convention for the Protection of Vertebrate Animals Used for Experimental and Other Scientific Purposes). All animal procedures were performed in accordance with the Spanish policy for animal protection (RD53/2013), which meets the requirements of the European Union directive 2010/63/UE regarding their protection during experimental procedures. Experimental procedures were approved by the Ethical Committee of CIC biomaGUNE and authorized by the regional government. Three protocols were authorized for a period valid since 15<sup>th</sup> July 2013 until 14<sup>th</sup> July 2016 under the protocol codes AE-biomaGUNE-0713, AE-biomaGUNE-0813 and AE-biomaGUNE-0913. Basically, the 0713 protocol authorized us to produce an orthotopic tumour model and evaluate its growth by *in vivo* imaging techniques. Although not commented on the thesis, an orthotopic tumour model was also tested and the growth evaluated by MRI contrast imaging. Nevertheless, due to a more homogeneous growth of SC tumours compared to the orthotopic ones and due to the fact that SC tumours were palpable and could be seen at naked eye some weeks after injection, we opted for the production of SC tumours.

The protocol 0813, was the one we used throughout the project; authorized us to induce a SC tumour to immunosuppressed mice and to evaluate the diagnostic efficacy of different radiolabeled nanosystems within time. Last but not least, the protocol 0913 was also approved. This last protocol was related to the study of the SC tumour growth or size regression; however, it was never utilized because none of the partners producing the NPs for therapy sent us the particles loaded with SiRNA (small interfering RNA) for the selected oncogenes and the antimetaloproteinases (antiMMPs) that have been identified as having therapeutic potential.

Within the consortium, different human pancreatic cancer cell lines were proposed to be used for the Save Me project: MiaPaca-2, ASPC-1, Panc-1, and T3M4 (101). Out of these four, human Panc-1 pancreatic cancer cell line, a pancreatic carcinoma of ductal origin, which over-expresses SSTR-1, SSTR-2 and SSTR-5 and Gal-1 receptor (102–104) was selected.

Mice, nude and albinos, were acquired from Charles River Laboratories Inc. and housed in polycarbonate ventilated cages (Tecniplast, S.p.A), which were changed once per week, under a controlled environment (12 h light/ 12 h dark cycles with dawn and dusk transitional periods, RT 25 °C and 55 % relative humidity) and maintained on an *ad libitum* access to commercially available pelleted diet (Teklad 2919, Harlan Laboratories, Inc.) and sterilized water. Mice were acclimated to the housing facility for at least 5 days prior to experiments.

Cell culture:

The human pancreatic tumour Panc-1 cell line was obtained from the European Collection of Cell Cultures (ECACC Cell Lines, Sigma Aldrich) and was maintained as a monolayer culture in RPMI-1640 media (Lonza, Verviers, Belgium) supplemented with 10 % fetal bovine serum, FBS (Sigma-Aldrich, St. Louis USA), 1 % penicillin-streptomycin mixture (Invitrogen, USA) and 2 mM glutamine (Lonza, Verviers, Belgium) at 37 °C in a humidified atmosphere of 5 % CO<sub>2</sub>/95 % air. Regular testing of the presence of Mycoplasma was performed with the use of a commercial kit (Lonza, Rockland, ME, USA).

Cells were harvested with trypsin/EDTA 0.25 % (Gibco, Life Technologies) and collected in a pellet by centrifugation. Thereafter, cell counting was done with the use of an automated cell counter (Cell Countess, Life Technologies). Cells were then suspended in Dulbecco's Phosphate Buffered Saline (PBS) (Lonza, Verviers, Belgium) to different final concentrations (5-20 x 10<sup>6</sup> cells/mL) depending on the number of cells to be inoculated. The suspension was mixed with Matrigel (Becton Dickinson, Oak Park, Bedford, MA), a mixture of laminin, type IV collagen, entactin and heparin sulphate kept at 4 °C at a 1:1 (v/v) ratio. Finally, 200 µL of the mixture were collected in a 1 ml syringe and used for the injection (99).

Cell inoculation:

Mice were anesthetized with inhaled isoflurane at 4-5 % in 100 % O<sub>2</sub>. Subsequently, the animals were placed in ventral position and maintained anesthetized with 1 - 2.5 % isoflurane using a facial mask for inhalation. A region in the left upper flank of the animals was chosen and the skin pinched with the help of tweezers in order to leave a space for the slow injection of the Panc-1 cells. After conducting the injection, the animals were recovered from anaesthesia and returned to their cages. Animal weight and tumour volume were monitored three times per week. The tumour volume (expressed in mm<sup>3</sup>) was calculated using the formula  $(L \times W^2)/2$  where L is the longest diameter (in mm) of the tumour and W (in mm) is the longest perpendicular diameter with respect to L, both measured with a calliper.

During set up of the experimental conditions to determine the optimal number of cells to be inoculated, 3 different numbers of cells were used: 0.5, 1 and 2 million per animal. After determination of the growth curves, the optimal number of cells was used in all subsequent *in vivo* imaging studies.

After inoculation of tumours with imaging purposes, mice were not randomized immediately after cell inoculation, but rather selected one week before starting the imaging studies. Consequently, when animal experiments were to start, at week 6-8 after inoculation (at this time point tumours had



appropriate size to approach imaging studies), animals were grouped according to their tumour volumes (see Figure 14). Animals bearing tumours with equivalent size were included in imaging experiments.

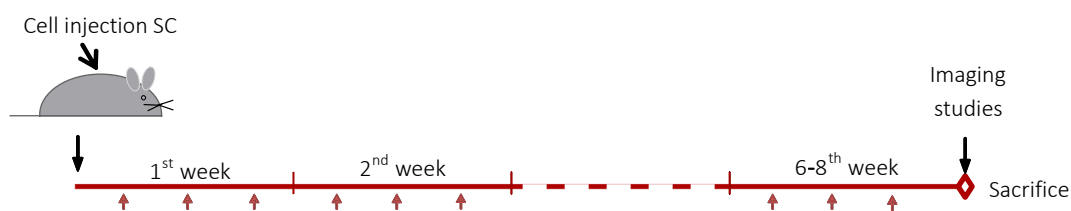


**Figure 14:** Flowchart of the experimental protocol for the study of tumour growth profile until imaging assays were conducted. Red arrows indicate animal monitoring procedures; animal weight and tumour volume calculations.

### 3.2.4.2 Nuclear imaging studies: Data acquisition and image processing

Imaging studies in tumour-bearing mice were performed for the different  $^{67}\text{Ga}$ -NPs. Mice received an intravenous (IV) injection of the radiolabelled NPs as a slow infusion in a total volume of 200  $\mu\text{L}$  of saline solution 0.9 % (see animal doses injection in section 3.3.1.4) three hours before examination. During the administration of the doses and during image acquisition, anaesthesia was first induced using 4.5 – 5 % isoflurane and maintained with 1.5 – 2 % isoflurane blended with  $\text{O}_2$ . The liquid anaesthesia for inhalation Isoflurane (IsoFlo<sup>®</sup>) was a product from Abbott Laboratories. During the image acquisition, mice were kept normothermic using a heating blanket (Homeothermic Blanket Control Unit; Bruker BioSpin GmbH, Karlsruhe, Germany). Body temperature was monitored using a rectal probe,

and respiratory frequency was monitored uninterruptedly during image acquisition.

SPECT-CT images were acquired using the eXplore speCZT CT preclinical imaging system from General Electric (GE Healthcare, USA). The system combines SPECT and CT on one gantry, allowing co-registration of the SPECT and CT datasets without additional post-processing. The SPECT scanner (see Figure 15 for general view of the camera and positioning of the animals in the scanner) uses a stationary, full ring of CZT detectors and interchangeable rotating cylindrical collimators. An 8-slit collimator was used with a field of view of 32 and 78 mm in the transaxial and axial directions, respectively. With the full ring detector, 360° of data were acquired by rotating the collimator 45° (45 steps, 1°/step).



**Figure 15:** SPECT-CT preclinical imaging system from GE installed in CIC biomaGUNE (A) and animal positioned on the SPECT-CT gantry (B).

Once the animals were positioned within the field of view of the system, data was collected in an energy window of 84-102 keV in static mode. The mice were under isoflurane anaesthesia during the whole-body SPECT-CT

scans acquired at 3, 24, and 48 hours post-injection for 30, 60, or 120 minutes (40sec/step, 80sec/step, or 160sec/step, respectively). As a general rule, the image acquisition period was dependent on the counts detected by the collimator of the scanner, thus, longer imaging times were needed as the gamma emissions decreased. After each SPECT scan, CT acquisitions were performed to provide anatomical information of each animal. The CT acquisition consisted of 220 views, acquired in 0.88° increments around the animal with 16 ms exposure per view. The X-ray tube settings were 70 kV and 32 mA.

SPECT images were reconstructed using the OSEM iterative algorithm (3 iterations, 5 subsets) into 128 x 128 x 32 array with a voxel size of 0.4 x 0.4 x 2.46 mm<sup>3</sup>, and were not corrected for scatter and attenuation. The CT images were reconstructed using a cone beam filtered back-projection Feldkamp algorithm into 437 x 437 x 523 array with a voxel size of 0.2 x 0.2 x 0.2 mm<sup>3</sup>.

Finally, images were analysed by  $\pi$ MOD software (version 3.4,  $\pi$ MOD Technologies Ltd., Zürich, Switzerland) co-registering SPECT and CT images. Volumes of interest (VOIs) were drawn around the organs under investigation (tumour and muscle), and results of the SPECT signal were used to calculate the tumour-to-muscle (T/M) ratio. Thereafter, the T/M ratios were determined and compared. Visual inspection of the images gave an overall idea of the biodistribution pattern of the NPs.

### 3.2.4.3 *Magnetic resonance imaging (MRI)*

Unlike SPECT, MRI technique does not use ionizing radiation and provides higher spatial resolution than SPECT and excellent contrast in soft tissue. Hence, accurate delineation of the tumour mass is achieved, although quantification of the amount of NPs in the different tissues is very challenging. Some of the samples produced by the Save Me partners were appropriate MRI contrast agents, as they contained  $\gamma$ -Fe<sub>2</sub>O<sub>3</sub> (BIU particles) or  $\gamma$ -Fe<sub>2</sub>O<sub>3</sub> incorporated into a shell layer surrounded by the core polymer (GU particles). Despite it was not the main objective of this work, when possible, MRI studies were executed and the results compared to those obtained by SPECT.

Prior to conducting MRI imaging experiments, the animals were anesthetized using 3.5 % isoflurane and maintained at 1.5 – 2.5 % in 100 % O<sub>2</sub> during the whole acquisition. Then, mice were placed in a mouse holder compatible with the MRI equipment and warmed throughout the study using a heated water blanket (Homeothermic Blanket Control Unit; Bruker BioSpin GmbH, Karlsruhe, Germany). Temperature was registered with a rectal probe and respiration rate was monitored with an MRI compatible animal monitoring system (SA Instruments Inc., New York, USA). One lateral tail vein of the animal was previously catheterized with a 26-gauge catheter (Hospira Venisystems Abbocath-T 26G Radiopaque I.V. cannula) for intravenous administration of the different NP formulations.

Measurements were conducted using an 11.7 Tesla horizontal bore Biospec 11.7/16 scanner (Bruker, Ettlingen, Germany) using a 40 mm transmit/receive body volumetric coil acquiring T2 weighted images (see Figure 16).



**Figure 16:** MRI 11.7 Tesla scanner from Bruker installed in CIC biomaGUNE.

Images were acquired before and after injection of the NPs to detect the distribution of the NP through the subcutaneous tumour and other organs of interest (e.g. liver, kidney). MRI images were acquired before injection (BI), around 2 hours post-injection (PI), as well as 24 h after injection. The image acquired at  $t = 24$  hours required re-positioning of the animal; attention was paid in order to place the animal in a similar position. Images were then normalized, *i.e.* a reference organ was selected in the same slice

of the tumour and the contrasts weighted towards it. An area in the spinal cord was anticipated to be convenient as the reference tissue with normalization purposes. Firstly, the spine was visible in all MR slices through the abdomen and secondly, the spinal cord, as part of the central nervous system (CNS), is protected by the blood brain barrier (BBB), preventing the entrance of most contrast agents.

A summary of the NPs submitted to MRI *in vivo* studies is included in Table 5.

**Table 5:** List of NPs tested by MRI 11.7 T in the animal model bearing Panc-1 SC tumours (n=2/sample) and injected doses depending upon NP's iron content.

Partner ID & NP code	Functionalization: BFCA / targeting moiety	Fe [mg/100 mg body weight]
BIU-01	None	$1.7 * 10^{-3}$
BIU-02	PTR <sub>86</sub> -FITC	$1.6 * 10^{-3}$
BIU-03	tPA-FITC	$1.7 * 10^{-3}$
GU-01	DOTA-NHS	$4.2 * 10^{-4}$
GU-02	DOTA-NHS PTR <sub>86</sub> -FITC	$4.2 * 10^{-4}$
GU-03	DOTA-NHS tPA	$4.2 * 10^{-4}$

Non-targeted NPs were used as negative control for BIU and GU particles (BIU-01 and GU-01). PTR<sub>86</sub> and tPA were used as targeting moieties. Similar

doses were injected into animals tested with BIU and GU particles, respectively.

Prior to acquiring any image, the MRI parameters were fixed. Image acquisition was synchronized with animal breathing (triggered acquisition). Then, a fast SCOUT (or exploratory) image for positioning was performed to the animal covering the area of interest using a field of view (FOV) of  $3 \times 3 \text{ cm}^2$  covered by a matrix of  $128 \times 128$  points fixing an in-plane resolution of  $234 \mu\text{m}/\text{pixel}$ . The volume of interest (VOI) was then selected to be of 26 slices of 0.6 mm thickness. Image contrast was settled by using an echo time (TE) and the repetition time (TR) values of 13.4 ms and 1050 ms, respectively. A TurboRARE (Rapid Acquisition with Relaxation Enhancement) sequence (RAREfactor = 4) was chosen for T2 imaging using the aforementioned spatial resolution, TE and TR times and slice thickness. At the same time of conducting the tests with the Save Me particles, tumour angiogenesis was assessed.

### 3.2.5 STATISTICAL METHODS

Statistical calculations and graphs were performed by applying a one-way ANalysis Of VAriance (ANOVA) for matched observations (105). In those cases where significant differences were found, the ANOVA test was followed by a Tukey's multiple comparisons post-hoc test using GraphPad

Prism versions 5.04 and 6.00 for Windows, GraphPad Software, La Jolla California USA, ([www.graphpad.com](http://www.graphpad.com)) and considering  $P \leq 0.05$  statistically significant. P values of  $P \leq 0.05$  (\*),  $P \leq 0.01$  (\*\*), or  $P \leq 0.001$  (\*\*\*) are indicated on the figures when appropriate. All data has been presented as the mean value of the group  $\pm$  SD error bars with a 95 % confidence interval. The obtained data was considered to follow a normal distribution and normality tests were not performed as too small samples would rather be affected by the lack of normality.



## 3.3 RESULTS AND DISCUSSION

### 3.3.1 RADIOLABELLING OF NANOPARTICLES

#### 3.3.1.1 *Purification of <sup>67</sup>Ga*

Gallium-67 was selected as the radioisotope because of its long half-life, which enabled longitudinal follow-up of the biodistribution pattern up to several days. The radionuclide was obtained as citrate solution at neutral pH, either from Molypharma, S.A. (Galdakao, Biscay, Spain) or from Mallinckrodt Radiopharmaceuticals Spain, S.L.U. (Cornellá de Llobregat, Catalonia, Spain). Hence, the first step to approach the radiolabelling of NPs consisted of converting it into the chloride form, much more appropriate for subsequent formation of the radiometal-chelator complex. This was carried out using solid phase extraction.

Absorption of <sup>67</sup>Ga in the purification resin was almost quantitative. The percentage of radioactivity absorbed in the cartridges after step 1 was 93.54 ± 4.54 % (see flowchart on Figure 12 in section 3.2.3.1) when an elution rate of 0.1 mL/min was used. The amount of radioactivity retained in the cartridges depended on the elution flow. As expected, faster elution resulted in lower trapping efficiency. Using a flow rate of 0.3 ml/min, only 49.46 ± 7.09 % was retained in the cartridges. Therefore, an elution rate to 0.1 ml/min was used in all subsequent experiments.

After rinsing with ultrapure water and flushing with air, the average percentage of radioactivity of  $^{67}\text{Ga}$  still attached to the resin was  $92 \pm 5 \%$  (referred to the starting amount of radioactivity).

The elution through the cartridge was carried out using a syringe pump. This has several advantages with respect to manual operation, mainly: (i) radiation exposure is minimized; and (ii) a constant flux is applied, and the time required to perform the complete elution through the cartridges can be estimated.

After flushing with air, the cartridges were flushed with hydrochloric acid and separated in 10 different fractions. Figure 17 shows the amount of radioactivity in each individual vial.

The overall recovery of radioactivity as  $^{67}\text{Ga}$  chloride was around a 90 %; this value is much higher than those reported in previous works (60 % of  $^{67}\text{Ga}$  recovery, see reference (97)). Approximately 94 % of the recovered radioactivity was distributed in the fourth, fifth and sixth collected fractions. Just to mention one specific example, in 5 different experiments in which an average activity of  $531 \pm 17$  MBq were withdrawn from the cartridges, the fourth, fifth and sixth peak fractions represented  $260 \pm 73$ ,  $213 \pm 75$  and  $27 \pm 5$  MBq of radioactivity, respectively.

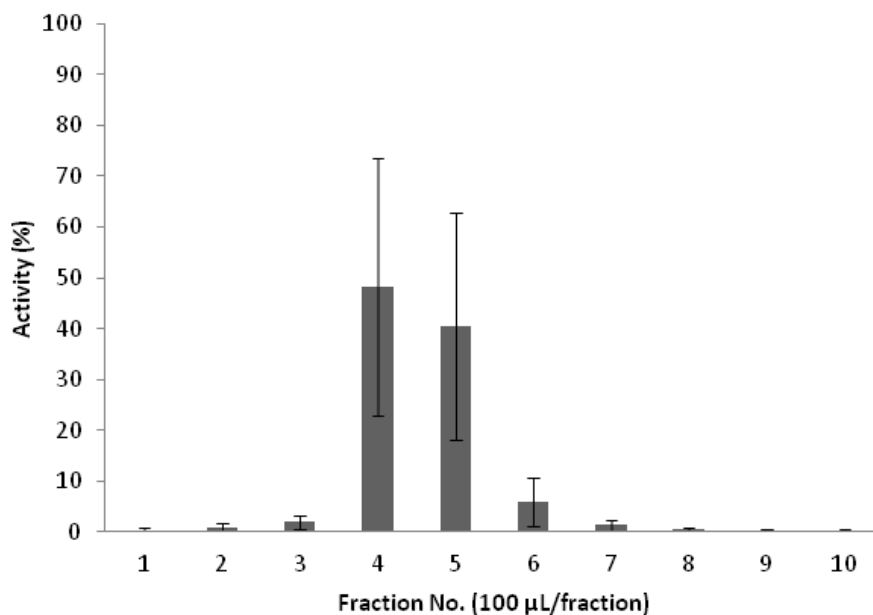


**Figure 17:** Graphical representation of the fractionated elution of  $^{67}\text{Ga}$  after extraction of the activity retained on the Sep-Pak<sup>®</sup> with 1 M  $\text{HCl}_{30\%}$ .

The overall duration of the purification process was between 52 and 87 minutes (depending on the amount of initial gallium volume). This time is acceptable taking into account the radioisotope's half-life ( $T_{1/2} = 3.26$  d) and the recovery percentage of  $90 \pm 4$  % of  $^{67}\text{Ga}$ .

The amount of radioactivity remaining in the cartridge after elution was very low (around 1 % of the retained activity). These values are significantly lower than those reported previously by I. Vergara *et al.* ( $30 \pm 5$  %) (97) probably due to their experimental procedure, in which they used 1 g of silica-gel for the adsorption of gallium ions instead of using a packed silica column, which

might be more convenient due to more efficient packing of the solid support. Besides, in the previous work desorption of gallium chloride ions by extracting the radioactive fraction (supernatant) after centrifugation (and sedimentation of the silica as pellet) in a larger acidic volume (3 mL HCl) may lead to a loss of efficiency.

### *3.3.1.2 Radiolabelling of NPs with $^{67}\text{Ga}$*

The radiolabelling reactions with the different NPs produced by the 4 partners producing the nanosystems were conducted by first converting the gallium citrate solution into gallium chloride. Diverse temperatures and reaction times were tested to determine the most efficient radiolabelling parameters. Moreover, the filtration parameters used during purification also varied depending on the nanosystems. Most of the NPs were radiolabelled at RT to prevent thermal damage to the NPs. Heating was eventually required to achieve good radiochemical conversion values. Nanosystems were sonicated before radiolabelling if recommended by the manufacturer of the NPs. Radiolabelling of NPs bearing FITC fluorescent agent was carried out under strict darkness.

Table 6 summarizes the radiolabelling conditions and the radiochemical conversion obtained for the different NPs. In all cases, a blank experiment was carried out by addition of all active reagents except the NPs. By conducting blank experiments, the formation of gallium colloids could be

observed when 4-(2-hydroxyethyl)-1-piperazineethanesulfonic acid (HEPES) was used as the buffer. Hence, acetate, which did not show the formation of colloids, was selected as the buffer of choice.

The amount of NPs used for the reactions was constant. Usually, 50  $\mu$ L of a 1 mg/mL stock solution was used. Nevertheless, for BIU NPs good radiochemical yields were achieved when only 10  $\mu$ L were used (see Table 6). The high incorporation ratios can be attributed to the presence of maghemite into the polymeric matrix of the NP core. The strong affinity between gallium ions and iron is well known (62,78,106). Our hypothesis is that radiolabelling in this case occurs thanks to absorption of gallium ions on the surface of maghemite NPs, or even incorporation into the crystal lattice.

**Table 6:** Optimized radiolabelling conditions and radiochemical conversion (RCC) values of <sup>67</sup>Ga labelled NPs for *in vivo* imaging studies in Panc-1 SC tumour model nude mice. All results are expressed as mean ± SD (n=4).

Partner ID & NP code	Functionalization: BFCA / targeting moiety	RCC ± SD %	Radiolabeling/ filtration conditions
CID-01	NH <sub>2</sub> -DOTA-GA	52 ± 25 %	60°C, 30 minutes/ 10 minutes, 4472 g
CID-02	NH <sub>2</sub> -DOTA-GA PTR <sub>86</sub> -FITC	53 ± 8 %	
CID-03	NH <sub>2</sub> -DOTA-GA tPA-FITC	9 ± 6 %	
BIU-01	None	74 ± 3 %	RT, 30 minutes/ 10 minutes, 4472 g
BIU-02	PTR <sub>86</sub>	71 ± 4 %	
BIU-03	tPA-FITC	71 ± 4 %	
UNIBO-01	NODA	52.2 ± 15.6 %	70°C, 30 minutes/ 10 minutes, 4472 g
UNIBO-02	NODA PTR <sub>86</sub>	57.7 ± 23.3 %	
UNIBO-03	NODA tPA-FITC	5.3 ± 2.7 %	
GU-01	DOTA-NHS	46.6 ± 11.2 %	30°C, 20 minutes/ 5 minutes, 2191 g
GU-02	DOTA-NHS PTR <sub>86</sub> -FITC	62.5 ± 18.3 %	
GU-03	DOTA-NHS tPA	51.2 ± 13.2 %	

For CID NPs, RCC values close to 50 % were obtained both for control and PTR<sub>86</sub> functionalized NPs, although heating to 60 °C was required. Labelling

at RT led to RCC values below 10 %. Interestingly, low labelling efficiencies were achieved for tPA-functionalized NPs, even when the reaction was carried out at 60 °C (see Table 6). No explanation was found for this unexpected result, although the low labelling efficiencies might be due to low amount of chelating agents on the surface of the NP or low availability, maybe due to the presence of the targeting moiety. These NPs were not submitted to *in vivo* imaging studies.

The nanosystems from BIU partner were efficiently labelled at RT. As previously mentioned, the efficient radiolabelling might be due to the interaction between gallium ions and the iron oxide particles entrapped in the polymeric matrix.

Nanoparticles provided by UNIBO were also efficiently radiolabelled, although a reaction temperature of 70 °C was required to achieve significant radiochemical yields. Again, NPs functionalized with tPA showed poor radiochemical yields, even when the labelling reaction was conducted at high temperature. This finding suggests the presence of tPA on the NPs may modify the surface properties, hampering efficient incorporation of the radiometal.

Radiolabelling of the NPs provided by GU was conducted at RT, because as specified by the manufacturer, these were not stable at temperatures above 37 °C. Good labelling efficiencies were obtained, irrespective of the

functionalization on the surface of the NPs. Surprisingly, and contrary to the results obtained with the NPs from other partners NPs functionalized with tPA could also be efficiently labelled.

One key factor to take into consideration is the specific activity of the labelled NPs. In order to prevent adverse effects after administration of the NPs into animals, the mass amount of NPs per animal was limited to 100 µg per study. Considering that previous experience in our imaging facility recommends the use of >1 MBq of radioactivity per *in vivo* investigation (this is the minimal amount that is considered to provide accurate biodistribution data in mice), the specific radioactivity required was 10 MBq/mg. This value of specific radioactivity was exceeded when >185 MBq of [<sup>67</sup>Ga]GaCl<sub>3</sub> were used.

### 3.3.1.3 *Radiochemical integrity of NPs*

The majority of the polymeric based NPs used in the current PhD thesis were radiolabelled by using BFCAs. As previously mentioned, the use of BFCAs can lead to the release of the radiometal because complexation is a reversible process with a defined  $K_m$ . Additionally, proteins present in the bloodstream can sequester the radiometal by trans-chelation. Hence, one critical step before evaluation of the NPs *in vivo* is the determination of the radiochemical integrity of the NPs *in vitro*. As mentioned above (see section



3.2.3.3) this can be done using different approximations to mimic *in vivo* conditions.

In our case, the radiochemical integrity was determined by incubation in the presence of a competitor (DOTA) at a concentration equivalent to apo-Transferrin concentration in blood (32  $\mu\text{M}$ ) for CID and GU NPs, while physiologic saline solution was used for BIU NPs.

The dissociation of  $^{67}\text{Ga}$  (expressed in percentage) from the radiolabelled NPs at each time point was calculated as the ratio between the amount of radioactivity in the filtrate and the starting amount of radioactivity after incubation of the radiolabelled samples at 37 °C (incubation time: 1 - 48 hours). All the experiments have been repeated twice and the results are expressed as mean  $\pm$  SD (see Table 7).

**Table 7:** Radiochemical integrity results of radiolabelled nanoparticles, expressed as percentage of unmodified NPs; <sup>1</sup>after incubation with a solution containing DOTA at a final concentration of 32  $\mu$ M; and <sup>2</sup>after incubation in saline solution. Incubation temperature was 37 °C in all cases.

Partner ID & NP code	1 h	3 h	24 h	48 h
CID-01 <sup>1</sup>	85 $\pm$ 14 %	83 $\pm$ 17 %	78 $\pm$ 8 %	57 $\pm$ 15 %
CID-02 <sup>1</sup>	69 $\pm$ 29 %	70 $\pm$ 25 %	63 $\pm$ 22 %	45 $\pm$ 15 %
GU-01 <sup>1</sup>	54 $\pm$ 0.4 %	39 $\pm$ 5 %	30 $\pm$ 19 %	29 $\pm$ 13 %
GU-02 <sup>1</sup>	57 $\pm$ 17 %	50 $\pm$ 15 %	29 $\pm$ 7 %	16 $\pm$ 1 %
GU-03 <sup>1</sup>	63 $\pm$ 23 %	59 $\pm$ 12 %	48 $\pm$ 7 %	45 $\pm$ 4 %
BIU-01 <sup>2</sup>	72 $\pm$ 13 %	74 $\pm$ 14 %	67 $\pm$ 4 %	19 $\pm$ 9 %
BIU-02 <sup>2</sup>	73 $\pm$ 11 %	60 $\pm$ 9 %	29 $\pm$ 9 %	24 $\pm$ 11 %
BIU-03 <sup>2</sup>	80 $\pm$ 12 %	74 $\pm$ 9 %	56 $\pm$ 7 %	67 $\pm$ 4 %

As it can be seen in the table, the fraction of radioactivity detached from the NPs was significant in all cases at t= 48 hours. Such detachment was higher in BIU and GU NPs, while CID particles showed higher stability in the presence of the competitor. Interestingly, CID and GU's NPs showed very high stability when incubated in physiologic saline solution, with >90 % of radioactivity attached to the NPs even at t= 48 hours of incubation.

Altogether, the results suggest that the presence of the competitor at a concentration similar to that of the Apo-transferrin has a marked effect on the radiochemical integrity of the NPs, which may have a significant impact during *in vivo* investigations.

During the performance of the experiments, UNIBO's NPs radiochemical integrity was not assessed. *A priori*, these NPs are similar to those of GU partner, bearing a BFCA and a maghemite core, as well as same targeting moieties. For these reasons, similar results could be expected.

#### 3.3.1.4 *Dose preparation*

Average doses as prepared for subsequent *in vivo* imaging experiments using the NPs provided by all partners are summarized in Table 8.

**Table 8:** Average injected dose of each <sup>67</sup>Ga radiolabelled compound for *in vivo* SPECT-CT animal experiments (n=2).

Partner ID & NP code	Average administered dose (MBq) ± STDV
CID-01	45.7 ± 18.9
CID-02	20.1 ± 11.5
UNIBO-01	30.41 ± 1.7
UNIBO-02	19.5 ± 14.5
GU-01	6.7 ± 0.9
GU-02	6.3 ± 1.5
GU-03	10.1 ± 5.9
BIU-01	15.5 ± 4.7
BIU-02	8.2 ± 1.8
BIU-03	8.9 ± 0.9

### 3.3.2 ANIMAL MODEL: HUMAN PANCREATIC CARCINOMA TUMOURS GROWTH AND CHARACTERIZATION

As mentioned above, a first experiment was conducted using different cell concentrations per animal group (n=10) as to determine the optimal tumour growth curve in the animal model. With that aim, SC injections of pre-established amounts of cells (0.5 million, 1 and 2 million) were performed in the back of immunosuppressed mice (CD-1<sup>®</sup> Foxn1<sup>nu</sup>) following previously published works (101,102,107,108).

A frequent monitoring of the tumour volume and animal weight was carried out during several weeks, and tumour volume data was plotted. As expected, the growth of Panc-1 SC tumours followed an exponential profile (see Figure 18).

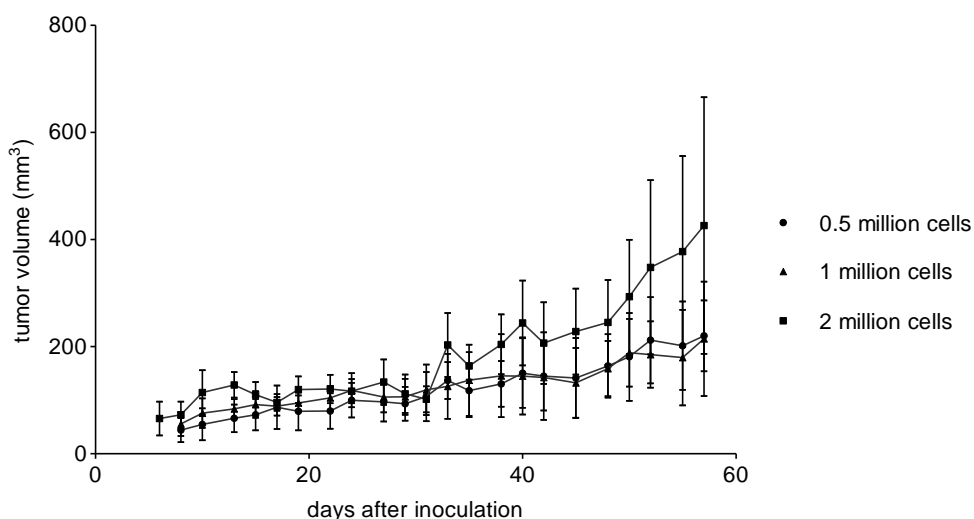


**Figure 18:** Panc-1 SC tumours growth curve represented in volume (mm<sup>3</sup>) throughout time expressed in days after inoculation of 0.5 million (rhombus), 1 million (triangle) and 2 million (square) tumour cells. Results are expressed as mean  $\pm$  SD, n=10 per group.

After injection of 2 million Panc-1 cells, average tumour volumes of *ca.* 150 mm<sup>3</sup> were achieved within 6 to 8 weeks (see Figure 19 for example of an animal with the tumour). This is a reasonable time that enables appropriate planning of the imaging studies. Injection of 0.5 and 1 million cells led to a

slower tumour growth, and hence the value of 2 million cells was selected as the most appropriate experimental scenario.



**Figure 19:** Photograph of a representative immunosuppressed mouse with a pancreatic SC tumour in its left flank 8 weeks after injection of 2 million Panc-1 cells.

The information obtained in this experiment was essential for the determination of the number of animals to be prepared, because it provided relevant information regarding the variability of the animal model.

Before performing *in vivo* imaging studies, the expression of SSTRs in the tumour was checked. With that aim, a representative number of tumours excised from animals were sent to SHEBA partner, who determined the expression of the different SSTR subtypes by using immunohistochemistry. High expression of SSTR2 and SSTR4 was observed in the excised tumours, followed by SSTR1's. The expression of SSTR3 and SSTR5 was detectable but weak when compared to other SSTR subtypes.

For execution of the first *in vivo* screening with the radiolabelled NPs, 50 nude mice were inoculated. Out of these, and considering the variability of the model, we estimated that the appropriate number of animals would have the correct tumour volume (ca. 150 mm<sup>3</sup>) after 6-8 weeks, taking into account that 2 animals were to be used per each NP and that the maximum number of samples to be received was 15. Finally, as previously mentioned, only 11 samples could be successfully labelled and hence only these were included in *in vivo* investigations. Figure 20 shows the growth curve obtained for the animals inoculated with imaging purposes.

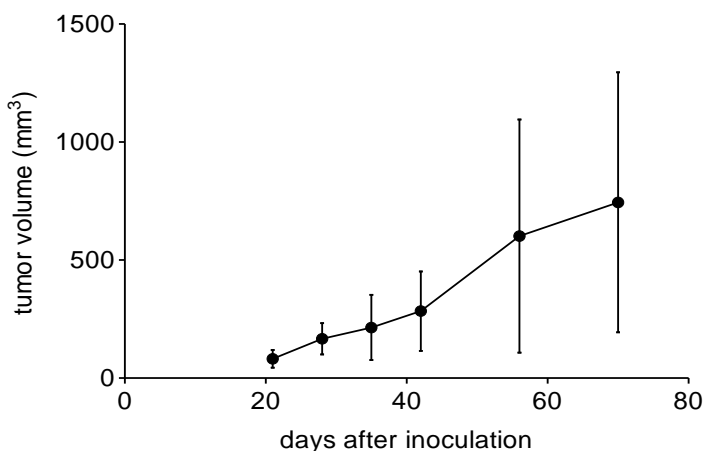


**Figure 20:** Panc-1 SC tumours growth curve represented in volume (mm<sup>3</sup>) throughout time expressed in days after inoculation of 2 million tumour cells. Dots, mean; lines, SD; n=50.

### 3.3.3 *IN VIVO* BIODISTRIBUTION IMAGING STUDIES

#### 3.3.3.1 *SPECT-CT: Biodistribution pattern of the different NPs*

SPECT-CT imaging studies were conducted with radiolabelled NPs. With that aim,  $^{67}\text{Ga}$ -functionalized NPs were suspended in a certain volume of saline solution (NaCl 0.9 %) and administered *via* one of the lateral tail veins of tumour-bearing mice. After administration of the radioactive NPs, the animals were recovered from anaesthesia until undergoing the first imaging study. Images were acquired at 3, 24 and 48 hours after administration of the radiolabelled NPs.

Because absolute quantification in our experimental set up was very challenging, we decided to determine the ratio between the tumour and a region of reference, namely the muscle. VOIs were delineated in the tumour and in the muscles anterior to the femur (quadriceps) and the T/M ratio was calculated for each time point and NP type (see Figures 21, 23, 25 and 27).

For BIU's NPs, no significant differences were observed between targeted and non-targeted NPs at each individual time point. The T/M ratios for the control NPs (BIU-01) were  $1.36 \pm 0.18$ ,  $1.84 \pm 0.62$  and  $2.84 \pm 0.66$  at 3, 24 and 48 hours after injection of the NPs, respectively. BIU's particles bearing PTR targeting moiety (BIU-02) showed increased accumulation with time starting with a T/M ratio of  $1.20 \pm 0.25$  at  $t = 3$  hours, which increased up to



2.15 ± 0.23 and 3.00 ± 0.54 at 24 and 48 hours, respectively. For NPs decorated with tPA (BIU-03), T/M ratios were 1.50 ± 0.18, 2.52 ± 0.70 and 2.36 ± 0.90 at 3, 24 and 48 hours, respectively.

Interestingly, statistically significant differences were observed for BIU-01 between t= 24 and t= 48 hours (P = 0.019), and for BIU-02 NPs between t= 3 and t= 24 hours (P = 0.013) (see Figure 21). These results suggest that NPs accumulate in the tumour due to EPR effect (note that non-targeted NPs also show an increased accumulation with time) while the targeting moiety seems not to play a pivotal role in this particular case. Likewise, the tPA targeting moiety seems to have a negative effect on the accumulation in the tumour.

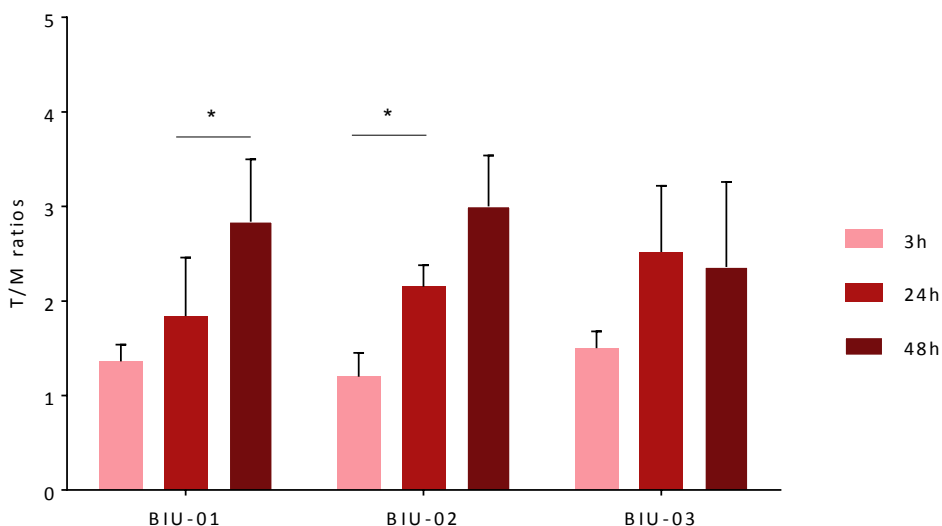


**Figure 21:** Average T/M ratios (mean  $\pm$  SD, n=2) for NPs BIU-01, BIU-02 and BIU-03 at 3, 24 and 48 hours after intravenous administration of labelled NPs ( $15.5 \pm 4.6$  MBq,  $8.2 \pm 1.8$  MBq and  $8.9 \pm 0.9$  MBq, respectively).

Visual inspection of the SPECT-CT images (see Figures 22-24) showed high accumulation of the NPs in the liver and the spleen, suggesting sequestration of the labelled NPs by the RES organs. In dorsal 3D images and a nearly lateral view of the animals, the liver's uptake is highlighted in a light bluish colour for clarity. Radioactivity could also be detected to a lesser extent in the lungs and in bones. The radioactivity in bones is more clearly visualized in the bone marrow and leg joints as can be observed in the bottom image of the axial slices. The presence of radioactivity in the bladder suggests elimination *via* urine. Hence, potential detachment of the

radionuclide or trans-chelation to plasma proteins may occur *in vivo* after administration.

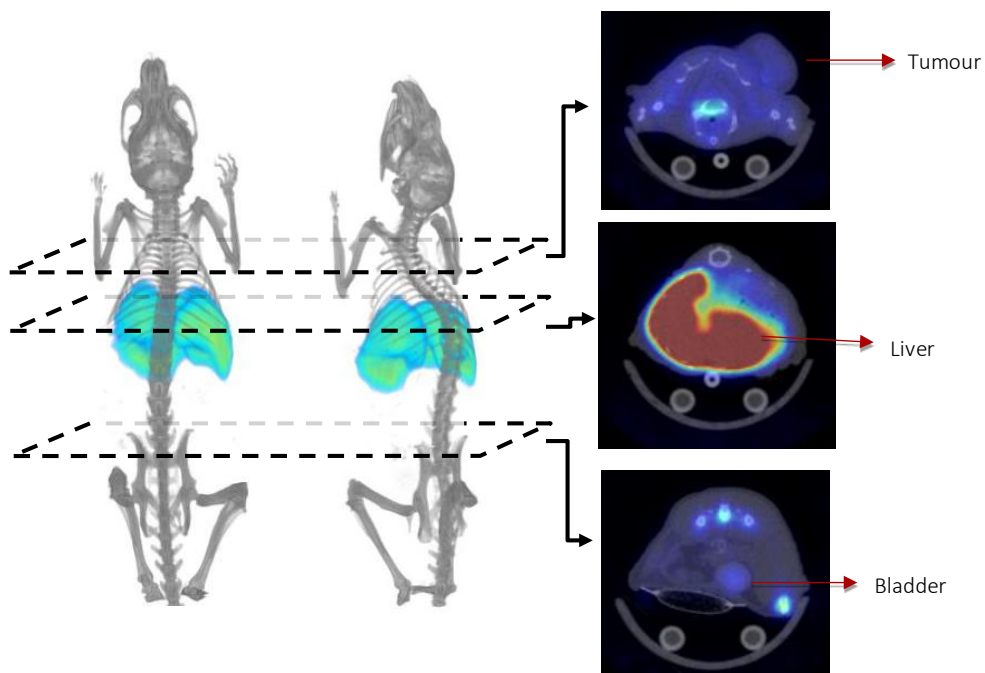


**Figure 22:** SPECT-CT 3D images of  $^{67}\text{Ga}$ -labelled BIU-01 NPs at  $t= 48$  hours after intravenous administration. Axial 2 dimensional (2D) slices show: tumour located in the upper dorsal left part of the animal (top), a transversal section of the liver (middle) and a slice in the inguinal region showing the bladder (bottom).

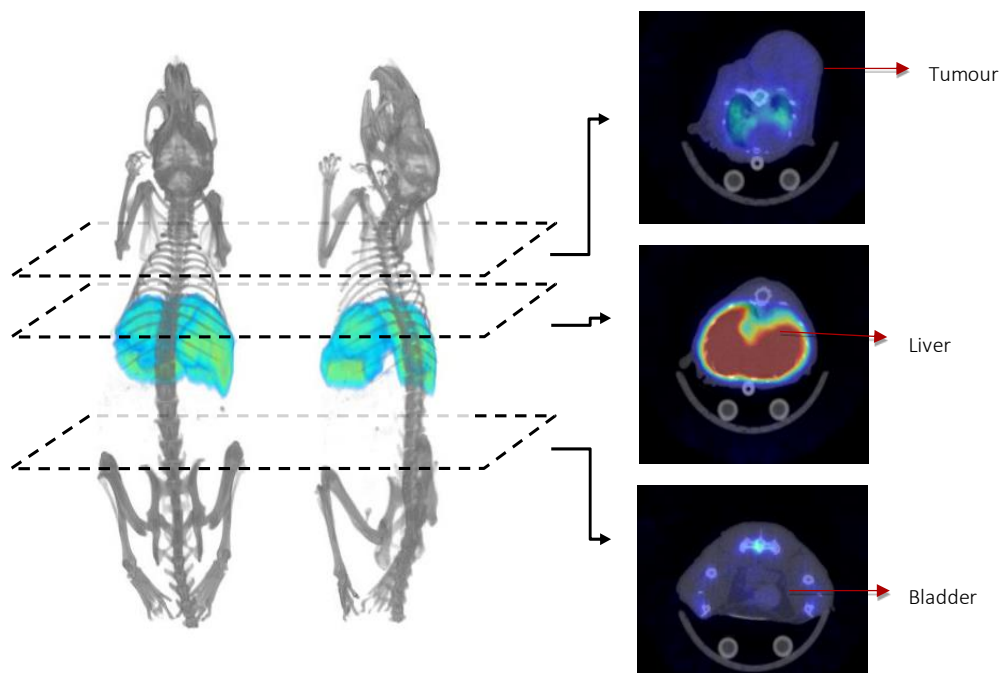


**Figure 23:** SPECT-CT 3D images of  $^{67}\text{Ga}$ -labelled BIU-02 NPs at  $t=48$  hours after intravenous administration. Axial 2D slices show: tumour located in the upper dorsal left part of the animal (top), a transversal section of the liver (middle) and a slice in the inguinal region showing the bladder (bottom).

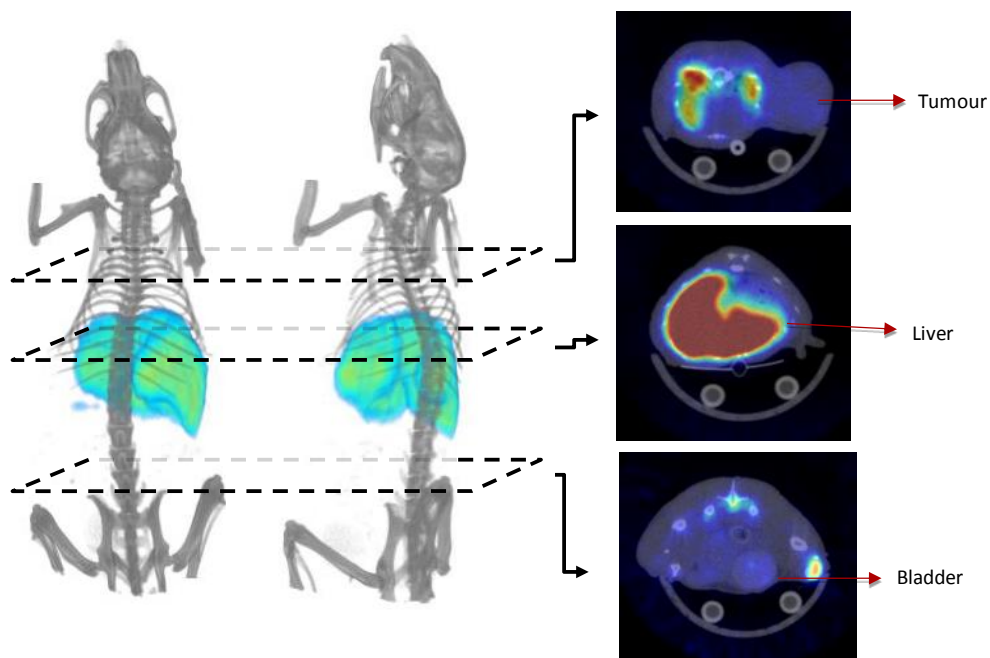


**Figure 24:** SPECT-CT 3D images of  $^{67}\text{Ga}$ -labelled BIU-03 NPs at  $t= 48$  hours after intravenous administration. Axial 2D slices show: tumour located in the upper dorsal left part of the animal (top), a transversal section of the liver (middle) and a slice in the inguinal region showing the bladder (bottom).

The same approach was used to investigate the biodistribution of GU's NPs. Figure 25 compares T/M values for the three particles investigated at different time points after administration. No significant differences in T/M values were observed, irrespective of the NPs and the time point. T/M ratios for non-targeted particles (GU-01) were  $1.57 \pm 0.38$ ,  $2.73 \pm 1.67$  and  $2.53 \pm 0.21$  at  $t= 3$ , 24 and 48 hours post-administration. The NPs bearing PTR showed a progressive, non-significant increase in T/M ratios:  $1.94 \pm 0.34$ ,  $3.04 \pm 0.69$  and  $4.08 \pm 0.11$  at  $t= 3$ , 24 and 48 hours, respectively. The NPs with tPA also showed an increase in T/M values with time:  $1.54 \pm 0.22$ ,  $2.63$

$\pm 0.35$  and  $3.07 \pm 0.54$  for  $t= 3, 24$  and  $48$  hours, respectively. Despite the differences are not significant between groups, probably due to the small sample size, a clear trend can be observed in the case of targeted particles, with higher T/M values at longer times post-administration. These results suggest that for GU's particles, accumulation in the tumour may occur by EPR effect; however, prolonged retention in the tumour can be achieved when the NPs bear a targeting moiety.

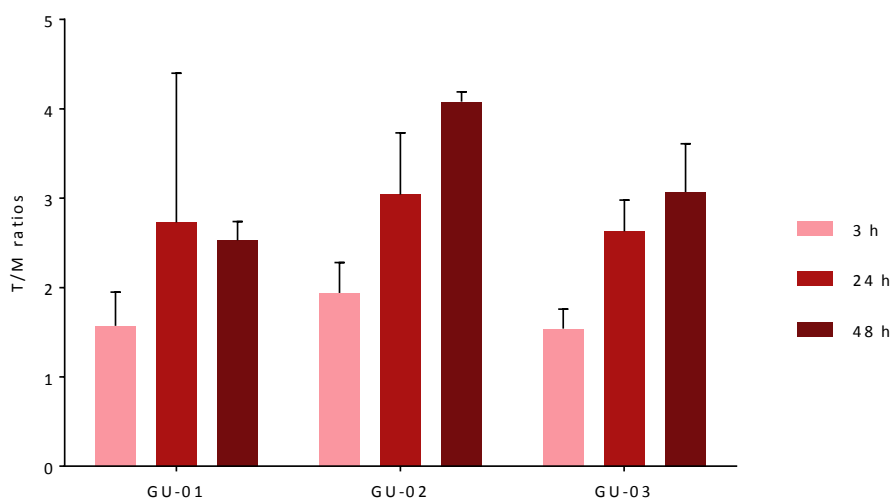


**Figure 25:** Average T/M ratios (mean  $\pm$  SD,  $n=2$ ) for NPs GU-01, GU-02 and GU-03 at 3, 24 and 48 hours after intravenous administration of labelled NPs ( $6.7 \pm 1.0$  MBq,  $6.3 \pm 1.5$  MBq and  $10.1 \pm 5.9$  MBq, respectively).

Figures 26-28 show representative SPECT-CT images (3D reconstructions and selected axial slices) for NPs GU-01, GU-02 and GU-03 at  $t= 48$  h after administration.

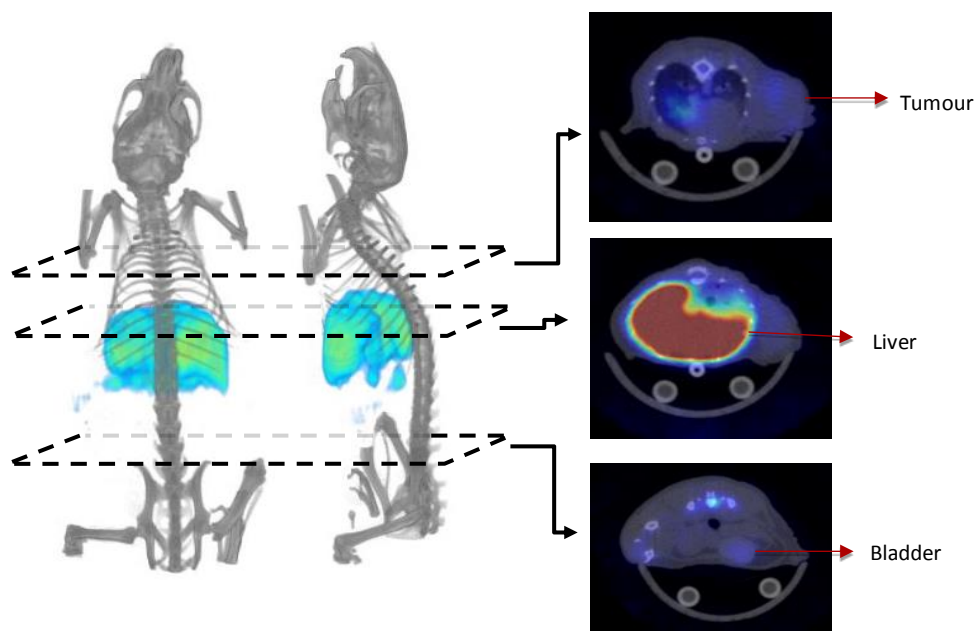


**Figure 26:** SPECT-CT 3D images of  $^{67}\text{Ga}$ -labelled GU-01 NPs at  $t= 48$  hours after intravenous administration. Axial 2D slices show: tumour located in the upper dorsal left part of the animal (top), a transversal section of the liver (middle) and a cut in the inguinal region showing the bladder (bottom).

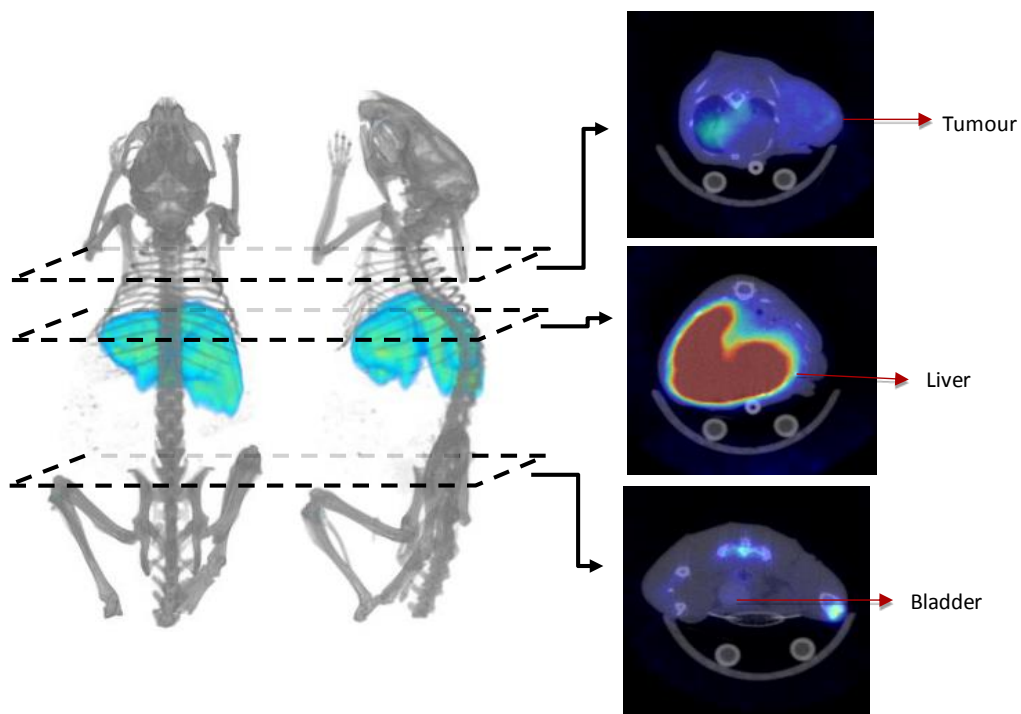


**Figure 27:** SPECT-CT 3D images of  $^{67}\text{Ga}$ -labelled GU-02 NPs at  $t= 48$  hours after intravenous administration. Axial 2D slices show: tumour located in the upper dorsal left part of the animal (top), a transversal section of the liver (middle) and a cut in the inguinal region showing the bladder (bottom).



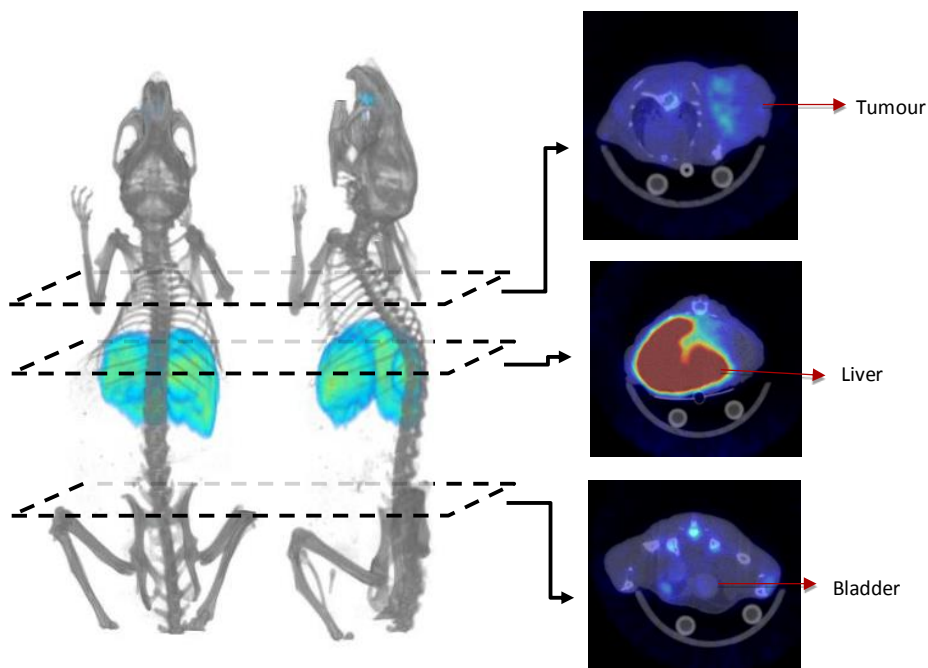


**Figure 28:** SPECT-CT 3D images of  $^{67}\text{Ga}$ -labelled GU-03 NPs at  $t= 48$  hours after intravenous administration. Axial 2D slices show: tumour located in the upper dorsal left part of the animal (top), a transversal section of the liver (middle) and a cut in the inguinal region showing the bladder (bottom).

Visual inspection of the images (see Figures above) clearly shows high accumulation of radioactivity in the liver, probably due to sequestration of the NPs by the MPS. However, in this case the presence of radioactivity could also be detected in the tumour. The distribution of the labelled NPs in the tumour was not uniform, as suggested by the presence of hot spots (see top axial slice in Figures 26-28). The non-uniform distribution of the particles over the tumour tissue was later on confirmed by MRI (*vide infra*).

The experiment was repeated for UNIBO's NPs. Control, non-targeted particles showed T/M ratios of  $0.81 \pm 0.10$ ,  $1.17 \pm 0.14$  and  $0.91 \pm 0.07$  at 3, 24 and 48 hours after administration (see Figure 29).

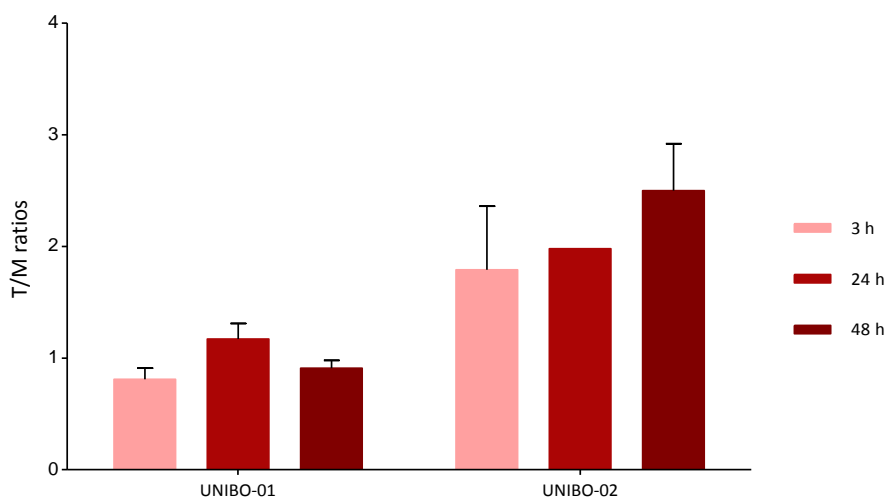


**Figure 29:** Average T/M ratios (mean  $\pm$  SD, n=2) for NPs UNIBO-01 and UNIBO-02 at 3, 24 and 48 hours after intravenous administration of labelled NPs ( $30.41 \pm 1.66$  MBq and  $19.50 \pm 14.50$  MBq doses respectively).

T/M ratios for the PTR-targeted particles showed a non-significant increase with time:  $1.79 \pm 0.57$ ,  $1.98 \pm 0.004$  and  $2.50 \pm 0.42$  at  $t= 3, 24$  and 48 hours. As in the case of GU's NPs, the targeting moiety seems to play a role in the accumulation of these NPs in the tumour, despite no significant differences between groups were obtained, probably due to the small sample size (see Figure 29). Nevertheless, the axial slices of the images (see Figures 30-32) do

not show uptake in the tumour, neither for the control nor PTR-targeted particles. Intriguingly, targeted NPs presented a higher accumulation in the spleen than any other particle. UNIBO-02 was in fact the only nanosystem with an especially high accumulation rate in the spleen compared to that of the liver (see dorsal and lateral 3D views in Figure 31).

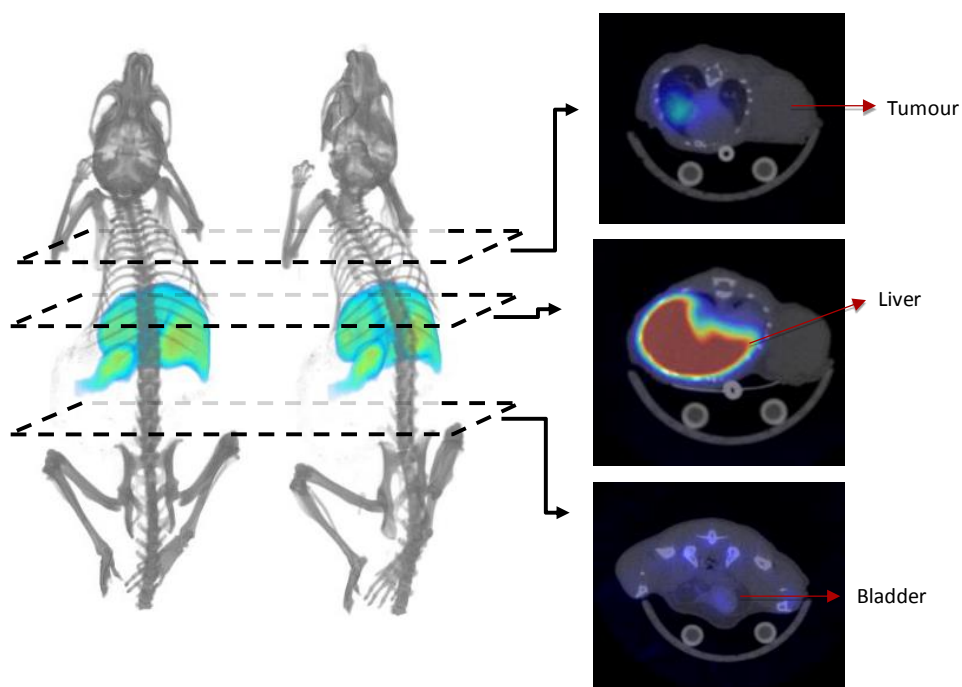


**Figure 30:** SPECT-CT 3D images of  $^{67}\text{Ga}$ -labelled UNIBO-01 NPs at  $t= 48$  hours after intravenous administration. Axial 2D slices show: tumour located in the upper dorsal left part of the animal (top), a transversal section of the liver (middle) and a cut in the inguinal region showing the bladder (bottom).

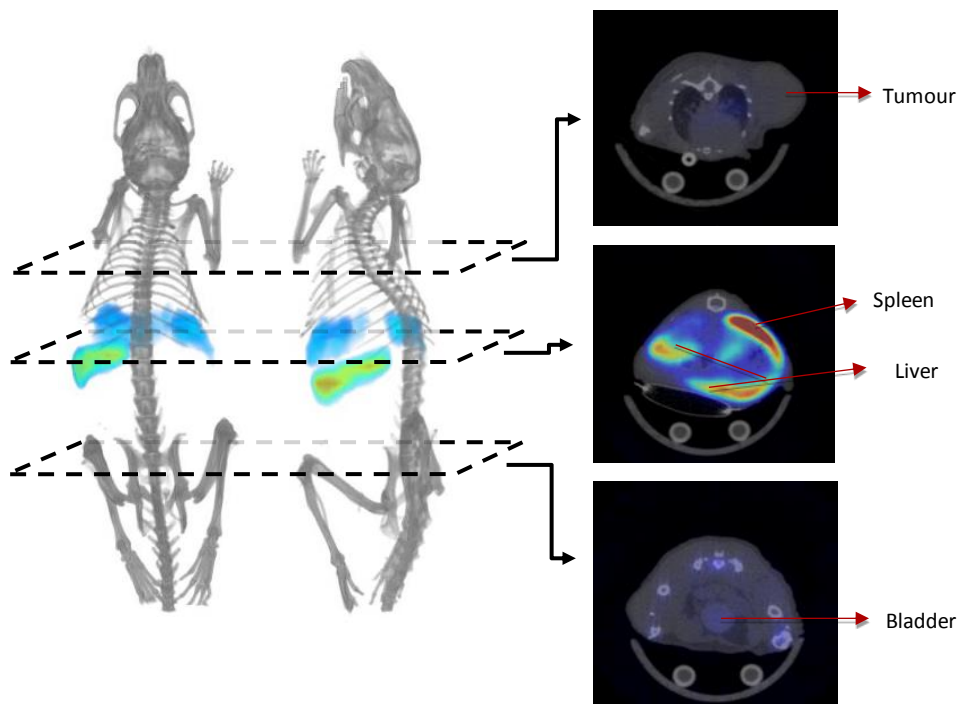


**Figure 31:** SPECT-CT 3D images of  $^{67}\text{Ga}$ -labelled and UNIBO-02 NPs at  $t= 48$  hours after intravenous administration. Axial 2D slices show: tumour located in the upper dorsal left part of the animal (top), a transversal section of the liver (middle) and a cut in the inguinal region showing the bladder (bottom).

CID's particles bearing tPA targeting moiety were not tested *in vivo* as previously mentioned, due to the low radiochemical incorporation ratios achieved during labelling experiments. Therefore, only CID-01 and CID-02 were assayed (see Figure 32).

The T/M ratios for CID's control (non-targeted) particles were  $1.22 \pm 0.14$ ,  $1.75 \pm 0.32$  and  $2.55 \pm 0.40$  at  $t= 3$ , 24 and 48 hours, respectively. For targeted particles, T/M values of  $1.44 \pm 0.03$ ,  $3.08 \pm 0.93$  and  $3.92 \pm 0.05$

were obtained at t= 3, 24 and 48 hours, respectively. As can be observed in Figure 32, T/M values increased clearly with time.

The most important finding in these NPs was the lower accumulation of radioactivity in the liver, as compared to previously investigated NPs. This lower accumulation, which can be observed by visual inspection of the images (see Figures 33-34) resulted in a higher bioavailability of the NPs, which led to better delineation of the tumour (see also Figure 35).

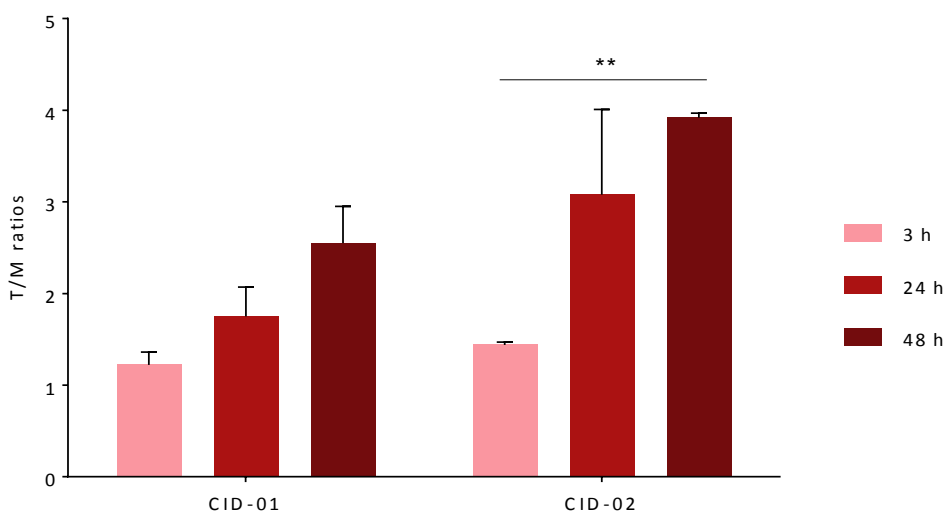


**Figure 32:** Average T/M ratios (mean  $\pm$  SD, n=2) for NPs CID-01 and CID-02 at 3, 24 and 48 hours after intravenous administration of labelled NPs ( $45.7 \pm 18.9$  MBq and  $20.1 \pm 11.5$  MBq, respectively).

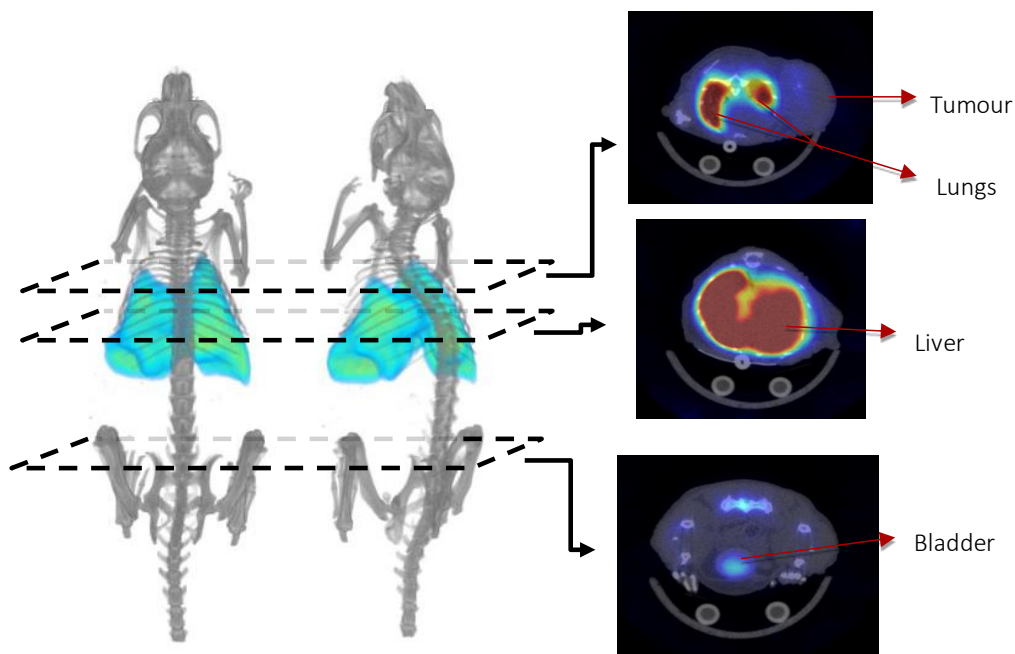


**Figure 33:** SPECT-CT 3D images of  $^{67}\text{Ga}$ -labelled CID-01 NPs at  $t= 48$  hours after intravenous administration. Axial 2D slices show: tumour located in the upper dorsal left part of the animal (top), a transversal section of the liver (middle) and a cut in the inguinal region showing the bladder (bottom).

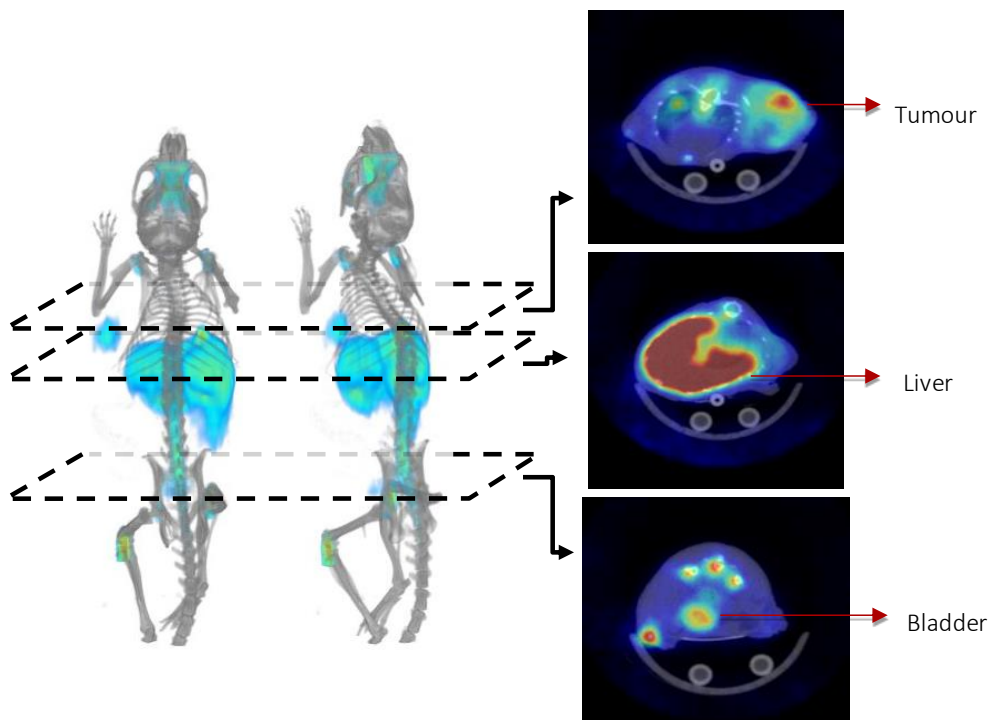


**Figure 34:** SPECT-CT 3D images of  $^{67}\text{Ga}$ -labelled CID-02 NPs at  $t= 48$  hours after intravenous administration. Axial 2D slices show: tumour located in the upper dorsal left part of the animal (top), a transversal section of the liver (middle) and a cut in the inguinal region showing the bladder (bottom).

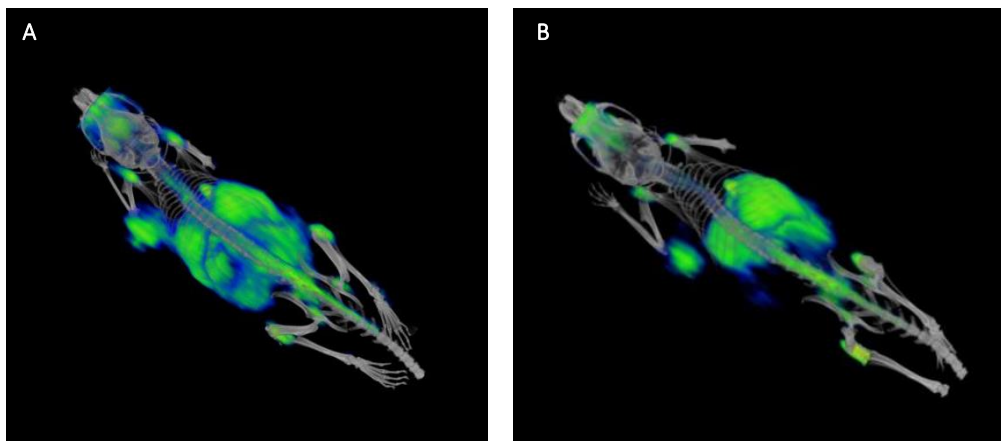


**Figure 35:** SPECT-CT 3D images of an animal injected with CID-02 NPs 24 hours (A) and 48 hours (B) after administration of the radioactive doses.

Interestingly, a high accumulation in urine was detected at  $t = 48$  hours, suggesting a slow elimination of the NPs *via* this route or detachment of the radiometal. The significant accumulation in the tumour and the low liver uptake resulted in images where the tumours could be clearly identified (see Figures 34-35).

The localized accumulation of radioactivity into the SC tumours of animals injected with CID-02 can be clearly visualized on the images. Uptake in the bones and joints was also considerable as can be observed in the 2D bottom axial cut (see Figure 34). Moreover, and following the trend of the graphic shown in Figure 32, the accumulation of radioactivity in the tumour was high already at 24 hours and did not significantly increase after 48 hours.



In view of these results, CID particles were selected as the most promising core particles to undergo more extensive *in vivo* investigation.

### 3.3.3.2 MRI: Angiogenesis in the PaCa tumour stages

As mentioned above, 12 animals were submitted to MRI images by using BIU's and GU's samples, in order to gain knowledge regarding the regional distribution of the NPs within the tumour tissue. The images were recorded before injection (BI), and 2 and 24 hours post injection (PI). T2 weighted images were acquired for BIU particles (see Figure 36) and GU particles (see Figure 37) selecting a slice in which the tumour and the liver could be observed.

The advantages of multimodal imaging lead to various qualitative observations. The most relevant information obtained from MRI images is related to the regional distribution of the particles among tissues, including the tumour itself. It is also noteworthy that the high spatial resolution of MRI allows us to describe the tumour as a highly heterogeneous mass of tissue. As mentioned, the high spatial resolution of MRI showed a lack of homogeneity, nevertheless, the sensibility of this technique is not sufficient to provide a reliable quantification of the amount of particles distributed to the tumour area.

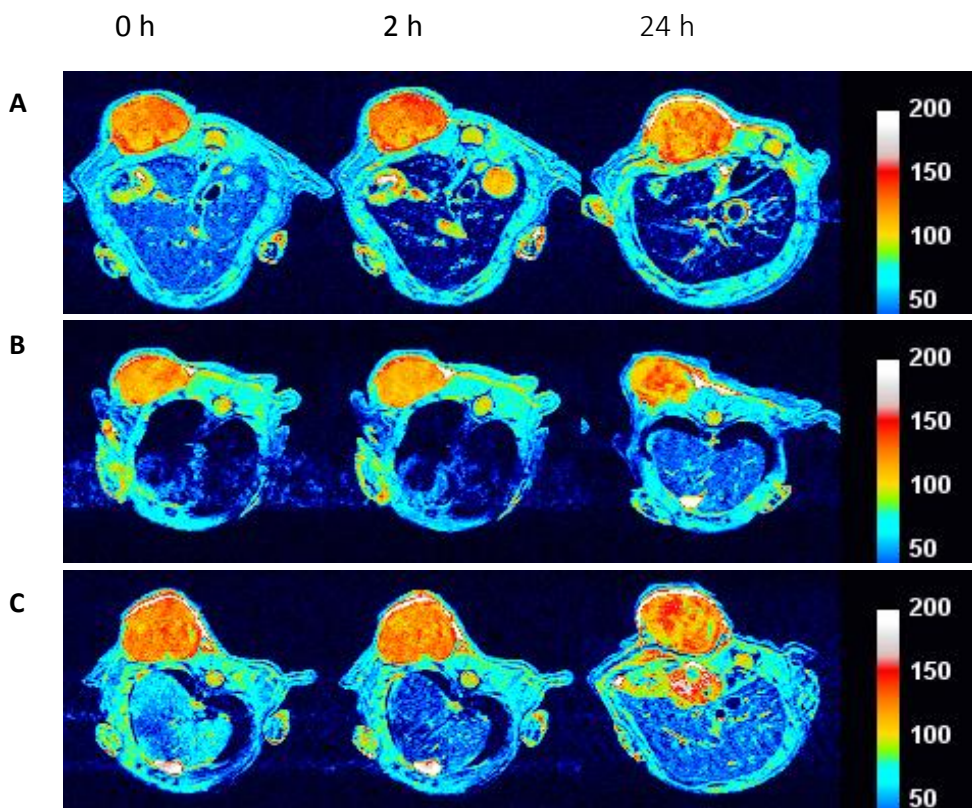


**Figure 36:** MRI T2-w images normalized against spinal-cord of the Panc-1 tumour bearing mice for BIU-01 (A), BIU-02 (B) and BIU-03 (C) particles at 0 h (before injection), and 2 and 24 h post injection. Scale reflects signal intensity (s.i.=100) in arbitrary units.

Some of the images suggest that the accumulation of NPs in the tumour increases with time as the signal decreases in the region, which is reflected in a progressive lighting of the tumour on the images. Similarly, the accumulation in liver is high and elimination from this organ occurs slowly. As a general trend, changes in the tumour signal were more significant at long time points (24 hours). This effect, which was observed for targeted

and non targeted BIU particles, is in good agreement with results obtained in SPECT images, which showed that uptake of NPs in the tumour was higher at  $t= 24$  h than at  $t= 3$  hours.

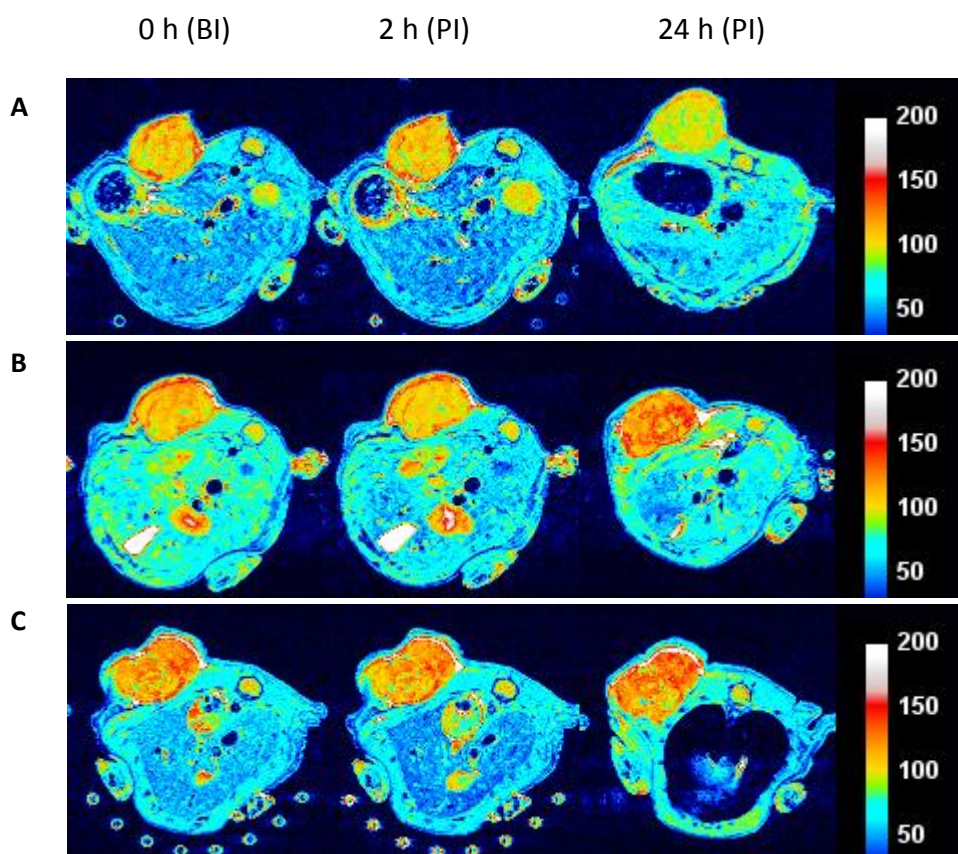


**Figure 37:** MRI T2-w images normalized against spinal-cord of the Panc-1 tumour bearing mice for GU-01 (A), GU-02 (B) and GU-03 (C) particles at  $t=0$  h (before injection) and  $t= 2$  and 24 h post injection. Scale reflects signal intensity (s.i.=100) in arbitrary units.

GU's targeted particles showed a more apparent contrast signal. Images acquired at 2 and 24 hours post injection clearly show a reddish signal

surrounding the tumour, which corresponds to the lymphatic system. PTR and tPA-1 targeted NPs (GU-02 and GU-03) showed a decrease at 24 hours relative to 2 hours. This finding suggests washout of targeted NPs from the target site. At 24 hours PI, the initial status was almost recovered as the tumour's shining increased and became comparable to that before injection.

### 3.4 CONCLUSIONS

The conversion step of  $^{67}\text{Ga}$  citrate into the chloride form resulted to be successful. Around 90 % of the total radioactivity could be recovered as chloride and used for further radiolabelling reactions. Additionally, the purification procedure was optimized as compared to the results reported previously in the literature (97).

The radiochemical labelling efficiency showed to be high when optimal reaction parameters were used. Harsh chemical conditions were avoided as compounds were going to be injected into animals.

NPs from CID and GU showed excellent radiochemical integrity in saline solution, with >90 % of the radioactivity still attached to the NPs after 48 hours of incubation. The presence of a chelator in the incubation media resulted in lower radiochemical integrity values.

For the implementation of the animal model, subcutaneous injection of 2 million Panc-1 cells resulted in an exponential tumour growth. Appropriate tumour sizes (150 mm<sup>3</sup>) could be achieved in 6-8 weeks after cell inoculation. This time window was considered appropriate for proper planning and execution of imaging experiments.

All NPs showed high accumulation in the liver, suggesting sequestration by the RES organs. Some of the NPs also showed elimination *via* urine,

suggesting potential detachment/transchelation of the radionuclide. SPECT-CT images showed that the most promising NPs for tumour visualization were the polymeric-based particles from CID. MRI images were of great value to confirm the heterogeneous vascularisation of cells along the tumour mass.

4. SECOND *IN VIVO* SCREENING:  
SELECTION OF OPTIMAL TARGETING  
WITH MOST PROMISING NP CORE





## 4.1 INTRODUCTION

After the first *in vivo* screening in which the highest T/M ratio at 48 hours was obtained with the particles from CID partner, the consortium as a whole decided to continue the development of new NPs with this partner. In this sense, CID provided new polymeric NPs with the same targeting agents attached to their structure, *i.e.*, PTR<sub>86</sub> and tPA. Moreover, a more promising targeting moiety based on SST analogues, named PTR<sub>58</sub>, which showed great affinity towards SSTRs, was developed (see section 4.2.1.1) and it was decided that it was worth assaying the targeting capabilities of this targeting agent after anchoring to the NPs.

It is widely accepted that NPs can be surface-decorated with PEG (PEGylation) in order to decrease undesired interactions with circulating proteins, as this interaction is majorly responsible for the subsequent sequestration of the NPs by the RES organs (109,110). Incorporation of PEG in the surface of the NPs provided by CID was thus considered an interesting approach in order to increase blood circulation time and potentially increase accumulation in the tumour. However, incorporation of long PEG chains on the surface of the NPs might lead to a significant increase in NP size, which may ultimately difficult cell internalization. To solve this issue, an innovative strategy was proposed by the consortium. The strategy was based on anchoring to the NP two PEG chains sandwiching a MMP substrate, namely, PEG-MMP-substrate-PEG.

In cancer proliferation, an inflammatory response is produced in which proteolytic cytokines are involved. Such is the case of gelatinase B (MMP-9), a proteolytic enzyme secreted in inflammation sites. *Via* the PEG-MMP-substrate-PEG functionality, the NPs might be recognized by the MMPs present in the extracellular matrix resulting in a cleavage of the outer protective PEG layer. The resulting NPs, smaller in size, might be more easily internalized into the tumour tissue, while exposed targeting moieties (PTR or tPA) should actively target tumour cells. The principle behind the approach is schematized in Figure 38.

In this context, and with the ultimate aim of assessing the effect of the different targeting moieties and PEGylation on the capacity of the nanosystems to selectively accumulate in the tumour, the following NPs were included in the final study: (i) Unmodified PMMAc core NPs (control); (ii) control particles functionalized with PTR<sub>86</sub>-FITC; (iii) control particles functionalized with tPA; (iv) control particles functionalized with PTR<sub>86</sub>-FITC and PEG-MMP-substrate-PEG; (v) control particles functionalized with tPA and PEG-MMP-substrate-PEG; (vi) control particles functionalized with PTR<sub>58</sub>-FITC; and (vii) control particles functionalized with PTR<sub>58</sub>-FITC and PEG-MMP-substrate-PEG.

Additionally, GU's particles were also selected for this final study in order to further investigate the effect of the core on the targeting capabilities of the newly developed targeting agent PTR<sub>58</sub>. As a result, GU partner also linked

this targeting moiety to their NPs and provided also unmodified particles as the control.

Following a similar experimental approach to that described in chapter 3, the T/M ratio was assessed at different time points after administration of the  $^{67}\text{Ga}$ -labelled particles using SPECT-CT for all particles; however, in order to gain statistical significance of the results, five animals were used per NP.

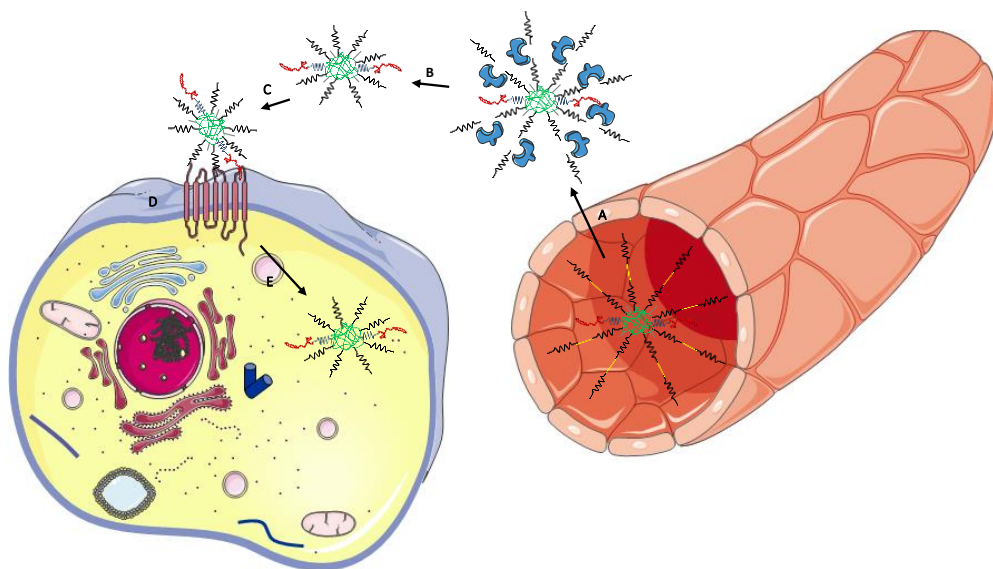


**Figure 38:** Schematic representation of the rationale behind the use of PEG-MMP-substrate-PEG decorations. The NPs present in the capillaries (A) cross the endothelial cells of the blood vessels and are recognized by MMPs, (B) which cleave the outer PEG chain, resulting in a reduction in NP size (C). Thanks to the presence of the targeting moieties, the NPs interact with tumour cell receptors (D) and are internalized (E).

## 4.2 MATERIALS AND METHODS

### 4.2.1 SYNTHESIS OF TARGETING MOIETIES

#### 4.2.1.1 *Synthesis of new SST analogues*

Recent studies have shown that replacement of the amino acid Asn in position 5 by the positively charged Arg results in an improvement of the affinity of PTRs for all SST receptor subtypes (111). In view of these results, a novel somatostatin analogue was synthesized and used in this project, with the following amino acids sequence; GABA-(D)Phe-**Arg**-cyclo(Cys-Phe-(D)Trp-Lys-Thr-Phe-GlyS<sub>2</sub>)-amide (PTR<sub>58</sub>). A FITC molecule was attached to the amino acid sequence following the procedure explained in section 3.2.1.1.

#### 4.2.1.2 *Synthesis of tPA analogues*

tPA analogue was synthesized following the synthetic strategy described in section 3.2.1.2.

### 4.2.2 SYNTHESIS OF NANOPARTICLES

Nanoparticles were prepared following the synthetic route described in sections 3.2.2.2 and 3.2.2.4, with slight modifications as described below.

#### 4.2.2.1 *IK4-CIDETEC*

Single chain polymeric NPs (1 g) were prepared and fully characterized. Further functionalization with targeting moieties and/or PEG decorations was performed using in all cases the same batch of NPs, which were properly characterized by different techniques, including NMR, TEM and DLS.

NODA was selected as the chelator for this set of experiments. NODA-functionalized targeted and non-targeted (control) SCPNs were synthesized (CID-04, CID-05, CID-06, CID-07, CID-08, CID-09 and CID-010, see Figure 11 in section 3.2.2.4 for clarity) by attachment of the commercially available 2,2'-(7-(4-((2-aminoethyl)amino)-1-carboxy-4-oxobutyl)-1,4,7-triazonane-1,4-diyl)diacetic acid (NH<sub>2</sub>-NODA-GA, MW: 417.46 g/mol) chelating agent purchased to CheMatech (Cat. No: C112) using covalent bonding. The quantification of the NH<sub>2</sub>-NODA-GA BFCA loading per nanoparticle (% w/w) was conducted by means of a xylenol orange/ZnCl<sub>2</sub> visual colorimetric assay based on a previously reported method originally implemented for DOTA (112). Basically, the incorporation of NH<sub>2</sub>-NODA-GA for radiolabelling to the different SCPNs was determined by incubating the NPs with a 0.1 % solution of xylenol orange (XO) tetrasodium salt (Acros, CAS: 3618-43-7) in distilled water and a solution containing ZnCl<sub>2</sub> (Sigma-Aldrich, CAS: 7646-85-7) in 0.01 N HCl. The principle behind this technique relies in the fact that Zn<sup>2+</sup> ions are more strongly linked to the BFCA than to XO at pH = 5.6. Hence, once all the

BFCAs are forming a complex with  $Zn^{2+}$  ions, the free  $Zn^{2+}$  ions react with XO forming a pink coloured XO- $Zn^{2+}$  complex, which can be visually identified.

The PMAAc NPs containing the BFCA were further functionalized with the targeting agents PTR<sub>86</sub>, PTR<sub>58</sub>, tPA, and PEG-MMP-substrate-PEG by sequential amide coupling as explained in section 3.2.2.4. The synthetic procedure has been recently patented by CID (Patent N. P3103EP00).

The PTR loading per NP (% w/w) was quantified by fluorescence using a calibration curve established with PTR<sub>86</sub>-FITC for the NPs bearing PTR<sub>86</sub> or PTR<sub>58</sub> (compounds CID-05, CID-07, CID-09 and CID-10). The amount of tPA present in CID-06 and CID-08 was calculated by UV absorption, and using a calibration curve established with tPA peptide (absorbance measured at  $\lambda$ : 277 nm).

The PEG-MMP-substrate-PEG, which contains a 24 amino acids chain in between two PEG fragments, was purchased to Synthezza (Cat. No: 1411370). The quantification of the PEGylated fragment of CID-07 and CID-08 could be determined by <sup>1</sup>H-NMR. The amount incorporated to CID-10 could not be determined.

The NPs used in this study, their main properties and the relative amount of targeting agents attached to the NPs are summarized in Table 9.

**Table 9:** Composition, functionalization, size, and PDI values of the NPs.

Partner ID & NP code	Core composition	Functionalization: BFCa / targeting moiety	Size (nm) (n=3)	PDI
CID-04	PMAAc based SCPNs	NH <sub>2</sub> -NODA-GA [15 % w/w]	35	0.3
CID-05	PMAAc based SCPNs	NH <sub>2</sub> -NODA-GA [1 % w/w] PTR <sub>86</sub> -FITC [6.7 % w/w]	38	0.4
CID-06	PMAAc based SCPNs	NH <sub>2</sub> -NODA-GA [2 % w/w] tPA [4 % w/w]	37	0.3
CID-07	PMAAc based SCPNs	NH <sub>2</sub> -NODA-GA [3 % w/w] PTR <sub>86</sub> -FITC [0.84 % w/w] PEG-MMP-substrate-PEG [3 % w/w]	52	0.6
CID-08	PMAAc based SCPNs	NH <sub>2</sub> -NODA-GA [3 % w/w] tPA [4 % w/w] PEG-MMP-substrate-PEG [3 % w/w]	39	0.4
CID-09	PMAAc based SCPNs	NH <sub>2</sub> -NODA-GA [5 % w/w] PTR <sub>58</sub> -FITC [1.7 % w/w]	40	0.453
CID-10	PMAAc based SCPNs	NH <sub>2</sub> -NODA-GA [4 % w/w] PTR <sub>58</sub> -FITC [1 % w/w] PEG-MMP-substrate-PEG [N/A*]	46	0.682

\* N/A: Information not provided by the supplier.

#### 4.2.2.2 Goethe University

The NPs provided by GU were synthesized by producing a CAN maghemite core with recombinant human serum albumin (rHSA), to which 2,2'-(7-(2-((2,5-dioxopyrrolidin-1-yl)oxy)-2-oxoethyl)-1,4,7-triazonane-1,4-diyl)diacetic acid (NOTA-NHS) was anchored as the chelator (CheMatech, Dijon, France). PTR<sub>58</sub> moiety containing fluorescein (FITC) was also anchored to the NP

surface *via* EDC chemistry (94). After production, the nanoparticles were purified by centrifugation and gel-permeation chromatography.

The NPs used in this study and their main properties are summarized in Table 10.

**Table 10:** Composition, functionalization, size, PDI and zeta-potential values of the NPs.

Partner ID & NP code	Core composition	Functionalization: BFCA / targeting moiety	Size (nm) (n=3)	PDI and Z potential
GU-04	CAN-Fe <sub>3</sub> O <sub>4</sub> -rHSA	NOTA-NHS [N/A*]	120 ± 1.4	N/A*
GU-05	CAN-Fe <sub>3</sub> O <sub>4</sub> -rHSA	NOTA-NHS [N/A*] PTR <sub>58</sub> -FITC [N/A*]	N/A*	N/A*

\* N/A: Information not provided by the supplier.

### 4.2.3 RADIOLABELLING OF NANOPARTICLES

#### 4.2.3.1 Purification of <sup>67</sup>Ga

As mentioned in section 1.3.4.1, gallium was obtained as a citrate form from commercial suppliers. The procedure for the transformation into the chloride form and fractioning was the same as explained in section 3.2.3.1.

#### 4.2.3.2 Radiolabelling and purification of NPs

The radiolabelling reactions were carried out as described in section 3.2.3.2 but with the NPs described in section 4.2.2. CID and GU incorporated NODA



or NOTA as BFCAs into the particles and hence the radiolabelling process relied on the formation of the  $^{67}\text{Ga}$ -NODA complex. The chelator-mediated labelling reactions were conducted by incubating  $^{67}\text{GaCl}^{3+}$  with 200  $\mu\text{L}$  of 0.2 M acetate buffer solution and 0.05 mg of the corresponding NPs, the latter obtained from stock solutions at a concentration of 1 mg/ml. The pH was measured by means of a pH-meter and reaction conditions (temperature, time and filtration parameters) as described in Table 6 were applied for both CID and GU particles. After purification through Millipore filters (100 kDa cut-off, Amicon Ultra-0.5 mL UFC510096, Molsheim, France) in a small centrifuge (Nahita, 2507/100 Auxilab S.L.) radiolabelling efficiencies were calculated and finally, the radioactive doses were prepared by suspending the residue present in the filters in 200  $\mu\text{L}$  of NaCl at 0.9 % (Braun Medical S.A., Catalonia, Spain).

#### *4.2.3.3 Radiochemical integrity of NPs*

The radiochemical integrity of the NPs was assessed following the procedure described in section 3.2.3.3, both in saline solution and in the presence of NOTA as the competitor; in both cases, the temperature was fixed at 37 °C.

#### *4.2.3.4 Dose preparation*

Animal doses were prepared as previously described in section 3.2.3.4 by diluting the purified labelled NPs in 200  $\mu\text{L}$  of saline solution 0.9 % and filling

Omnican® (B. Braun Vet Care GmbH, Melsungen AG, Germany) insulin syringes for injection.

#### 4.2.4 IMAGING STUDIES

##### 4.2.4.1 *Animal model: Athymic Nude Mice*

Following the experimental protocol described in section 3.2.4.1, animals (CD-1 Foxn1 nu/nu mice, Charles River Laboratories Inc., n=50) were subcutaneously injected with 2 million Panc-1 cells to develop the pancreatic tumours. Nude mice were housed as described in section 3.2.4.1 and the tumour growth monitored during 8 weeks. Animal images were acquired by SPECT-CT imaging at 3, 24 and 48 hours, after injection of the NPs described in section 4.2.2.

##### 4.2.4.2 *Nuclear imaging studies: Data acquisition and image processing*

Whole-body SPECT-CT images were acquired to a total number of 45 animals after injecting the different <sup>67</sup>Ga-NPs (n=5/NP). Thirty-five of these animals, all bearing SC tumours with tumour volume > 150 mm<sup>3</sup>, were used for CID's samples (weight 31.7 ± 2.6 g) and ten for GU's NPs (weight 30.8 ± 2.6 g). Mice received an IV injection of the radiolabelled systems as a slow infusion in a total volume of 200 µL of saline solution 0.9 % (see animal doses injection in section 4.3.1.3) three hours before examination. During the

administration of the doses and image acquisition, sedation was first induced using 4.5 – 5 % isoflurane and maintained with 1.5 – 2 % isoflurane blended with O<sub>2</sub>. The liquid anaesthesia for inhalation Isoflurane (IsoFlo®) was a product from Abbott Laboratories. During image acquisition, temperature was maintained by using a heating blanket (Homeothermic Blanket Control Unit; Bruker BioSpin GmbH, Karlsruhe, Germany). Animals' heart rate and body temperature were monitored uninterruptedly during imaging studies.

SPECT-CT images were acquired as previously described (section 3.2.4.2). Whole-body SPECT-CT scans were acquired at 3, 24, and 48 hours PI. After each SPECT scan, CT acquisitions were performed to provide anatomical information of each animal.

The SPECT images were reconstructed using the OSEM iterative algorithm (3 iterations, 5 subsets) into a 128 x 128 x 32 array with a voxel size of 0.4 x 0.4 x 2.46 mm<sup>3</sup>, and were not corrected for scatter and attenuation. The CT images were reconstructed using a cone beam filtered back-projection Feldkamp algorithm into 437 x 437 x 523 array with a voxel size of 0.2 x 0.2 x 0.2 mm<sup>3</sup>.

Finally, image data was analyzed by  $\pi$ MOD software (version 3.4,  $\pi$ MOD Technologies Ltd., Zürich, Switzerland) by co-registering SPECT and CT images. VOIs were drawn around the tissues under investigation (tumour

and muscle), and results of the SPECT signal were used to calculate the T/M ratios.

#### 4.2.5 STATISTICAL METHODS

Statistical calculations were performed by applying a one-way ANalysis Of VAriance (ANOVA) by using Graph Pad Prism software as in the case of the multiple comparisons of chapter 3 (see section 3.2.5). When significant differences between targeted and control NPs were observed, a Dunett's post-hoc test was performed to compare all groups with respect to the control group, in order to get more accurate information about the effect of the targeting moiety or surface decoration on the T/M ratio.

In the present study, independent samples have been compared and so, the normality assumption was tested within each group by means of residuals.

## 4.3 RESULTS AND DISCUSSION

### 4.3.1 RADIOLABELLING OF NPS

#### 4.3.1.1 Radiolabelling of NPs with $^{67}\text{Ga}$

The radiolabelling reactions with the different polymeric nanoparticles from CID partner were conducted by first converting gallium citrate to gallium chloride. Previous knowledge of the radiolabelling parameters of this NPs core bearing DOTA as BFCA made us think that the new samples bearing a NOTA derivative could be efficiently labelled at RT. Thereby, we conducted the radiolabelling experiments incubating 0.05 mg of the nanoparticles in 200  $\mu\text{L}$  of buffer acetate 0.2 M and 100  $\mu\text{L}$  of the peak fraction of  $^{67}\text{GaCl}$  at RT. Labelling time (30 minutes) and centrifugation parameters (10 minutes, 4472 g) were not modified with respect to chapter 3. Before radiolabelling, NPs were sonicated (2 minutes) to ensure proper dispersion, and pH values were maintained around 3.9 for the labelling step. Blank studies were also carried out to confirm the lack of formation of colloids.

Special attention was paid during radiolabelling of CID-05, CID-07, CID-09 and CID-10, as these particles could be damaged in contact with light due to the presence of the fluorescent moiety attached to the PTRs; *i.e.*, PTR<sub>86</sub>-FITC and PTR<sub>58</sub>-FITC.

NPs provided by GU were simply radiolabelled as described in chapter 3.

After radiolabelling, the unchelated gallium species were washed from the radiolabelled samples with 100 kDa cut-off Millipore filters as described in section 3.3.1.2. Thereafter, the radioactive doses for animals were prepared by suspending the precipitate in 200  $\mu$ L NaCl 0.9 % (see section 4.3.5). Table 11 summarizes the incorporation ratios obtained for the different NPs.

**Table 11:** Averaged RCC values expressed in percentage.

Partner ID & NP code	Functionalization: BFCA / targeting moiety	RCC $\pm$ SD %
CID-04	NH <sub>2</sub> -NODA-GA	63.9 $\pm$ 5.1 %
CID-05	NH <sub>2</sub> -NODA-GA PTR <sub>86</sub> -FITC	68.9 $\pm$ 2.0 %
CID-06	NH <sub>2</sub> -NODA-GA tPA	72.1 $\pm$ 2.5 %
CID-07	NH <sub>2</sub> -NODA-GA PTR <sub>86</sub> -FITC PEG-MMP-substrate-PEG	77.7 $\pm$ 1.1 %
CID-08	NH <sub>2</sub> -NODA-GA tPA PEG-MMP-substrate-PEG	74.6 $\pm$ 1.6 %
CID-09	NH <sub>2</sub> -NODA-GA PTR <sub>58</sub> -FITC	66.8 $\pm$ 4.1 %
CID-10	NH <sub>2</sub> -NODA-GA PTR <sub>58</sub> -FITC PEG-MMP-substrate-PEG	62.8 $\pm$ 5.2 %
GU-04	NOTA-NHS	42.8 $\pm$ 3.7 %
GU-05	NOTA-NHS PTR <sub>58</sub> -FITC	44.5 $\pm$ 2.2 %

In the case of CID's NPs, all NPs were efficiently radiolabelled at RT, possibly thanks to the NODA chelator. Moreover, the compounds bearing a targeting moiety did not show lower radiochemical conversion values. In fact, higher values were achieved. Despite not confirmed, this might be due to the presence of non-specific interactions of the functional groups present in the peptides with the radiometal.

In the case of GU's particles, lower radiolabelling efficiencies were obtained compared to data obtained in our previous studies (see Table 6).

All NPs were tested *in vivo* using 5 animals per NP. In the current study, radioactive doses were higher than those used in chapter 3 (see section 4.3.1.3). This was due to 2 main facts: (i) Higher RCC values were obtained; (ii) with the experience gained in previous studies, better planning and scheduling of the experimental work enabled a more efficient use of the radioactive gallium. In this occasion, radiolabelling experiments and imaging studies were designed to scan a lower number of animals per day, and the reception of commercially available gallium was better planned. Injection of higher amount of radioactivity enabled better results in terms of image quality.

#### 4.3.1.2 Radiochemical integrity of NPs

Radiochemical integrity of the developed final nanosystems was carefully assessed. The stability studies were conducted in presence of NOTA competitor at 37 °C. The results obtained are shown in Table 12.

**Table 12:** Stability of radiolabelled NPs, expressed as percentage of unmodified NPs, after incubation with a solution containing NOTA at a final concentration of 32 µM; incubation temperature: 37 °C.

Partner ID & NP code	2 min	1 h	3 h	24 h	48 h
CID-04	94.1 ± 1.4 %	94.0 ± 3.5 %	93.1 ± 1.8 %	85.3 ± 0.6 %	78.8 ± 4.9 %
CID-05	98.9 ± 0.5 %	96.0 ± 1.6 %	92.2 ± 5.7 %	88.2 ± 1.8 %	91.7 ± 5.2 %
CID-06	97.2 ± 1.3 %	96.5 ± 0.2 %	95.6 ± 0.5 %	88.5 ± 1.0 %	76.9 ± 6.9 %
CID-07	97.6 ± 1.1 %	96.9 ± 0.2 %	95.8 ± 0.7 %	85.4 ± 3.0 %	71.8 ± 14.8 %
CID-08	97.7 ± 1.7 %	97.7 ± 0.1 %	96.6 ± 1.0 %	85.5 ± 2.3 %	63.2 ± 2.3 %
CID-09	97.3 ± 0.6 %	94.7 ± 0.8 %	84.3 ± 6.2 %	83.5 ± 0.8 %	67.5 ± 6.1 %
CID-10	96.2 ± 1.9 %	95.4 ± 2.4 %	89.0 ± 5.3 %	83.8 ± 2.4 %	65.1 ± 1.2 %
GU-04	81.2 ± 1.8 %	64.3 ± 4.0 %	58.5 ± 2.1 %	34.8 ± 1.0 %	23.4 ± 4.1 %
GU-05	73.4 ± 20.6 %	52.9 ± 19.0 %	45.2 ± 22.4 %	31.7 ± 11.4 %	28.5 ± 4.9 %

As mentioned, the stability of the particles was also assessed in physiologic saline solution. The percentage of gallium attached to the NPs at different incubation times is represented in Table 13.



**Table 13:** Stability of radiolabelled NPs, expressed as percentage of unmodified NPs, after incubation with saline solution at 37 °C.

Partner ID & NP code	2 min	1 h	3 h	24 h	48 h
CID-04	94.4 ± 4.3 %	93.0 ± 1.3 %	85.0 ± 10.9 %	94.9 ± 0.4 %	96.6 ± 0.7 %
CID-05	92.9 ± 8.7 %	98.3 ± 0.6 %	94.6 ± 4.7 %	97.1 ± 0.1 %	89.8 ± 7.4 %
CID-06	97.5 ± 1.0 %	97.4 ± 1.1 %	97.3 ± 0.3 %	96.4 ± 0.7 %	95.8 ± 0.9 %
CID-07	97.7 ± 0.5 %	96.8 ± 0.1 %	97.5 ± 0.9 %	96.0 ± 1.9 %	94.7 ± 0.1 %
CID-08	97.8 ± 0.5 %	98.3 ± 0.4 %	97.7 ± 0.1 %	97.1 ± 0.6 %	92.8 ± 2.3 %
CID-09	96.0 ± 1.7 %	93.9 ± 4.7 %	96.4 ± 0.3 %	89.6 ± 7.4 %	88.4 ± 6.9 %
CID-10	97.7 ± 0.4 %	96.5 ± 0.4 %	95.6 ± 2.5 %	92.9 ± 0.4 %	91.7 ± 2.2 %
GU-04	80.1 ± 0.7 %	76.6 ± 0.4 %	87.8 ± 1.7 %	84.8 ± 2.5 %	81.6 ± 3.3 %
GU-05	92.2 ± 1.1 %	90.6 ± 0.6 %	91.9 ± 1.1 %	92.8 ± 1.9 %	92.1 ± 1.3 %

NPs showed excellent stability in physiologic saline solution, with >90 % of the radioactivity in all the NPs at t= 48 h except for CID-05, CID-09 and GU-04. In the presence of the competitor, this stability was slightly decreased to ~ 65 % in the NPs which contained the tPA and the PEG-MMP-substrate-PEG domain and in the ones labelled with PTR<sub>58</sub> moiety at t= 48h.

GU particles showed a very low stability in the presence of the competitor. The reason behind the low stability remains unknown, although a possible explanation is the lack of formation of the complex NODA-gallium. The

incorporation of the radionuclide in the NPs might be due to nonspecific interactions between the radiometal and the functional groups present in the protein at the core of the NPs. These interactions are weak, potentially leading to a loss of the label in the presence of strong chelators.

#### 4.3.1.3 Dose preparation

Doses were prepared as described in section 4.2.3.4. The amount of radioactivity used in the *in vivo* studies for the different NPs is summarized in Table 14.

**Table 14:** Average injected doses for the different <sup>67</sup>Ga-radiolabelled NPs for the *in vivo* SPECT-CT animal experiments (n=5).

Partner ID & NP code	Average administered dose (MBq) ± STDV
CID-04	44.4 ± 13.6
CID-05	24.7 ± 6.6
CID-06	35.7 ± 11.6
CID-07	40.9 ± 6.1
CID-08	38.1 ± 8.9
CID-09	32.5 ± 6.9
CID-10	24.4 ± 5.8
GU-04	18.5 ± 6.7
GU-05	13.8 ± 3.6

#### 4.3.2 ANIMAL MODEL: HUMAN PANCREATIC CARCINOMA TUMOURS GROWTH AND CHARACTERIZATION

Nine different NPs were assayed in tumour bearing mice. Because 5 animals were to be used per NP, 50 animals were inoculated with 2 million Panc-1 cells subcutaneously and the tumours growth curve studied. A representative growth curve can be seen in Figure 39.

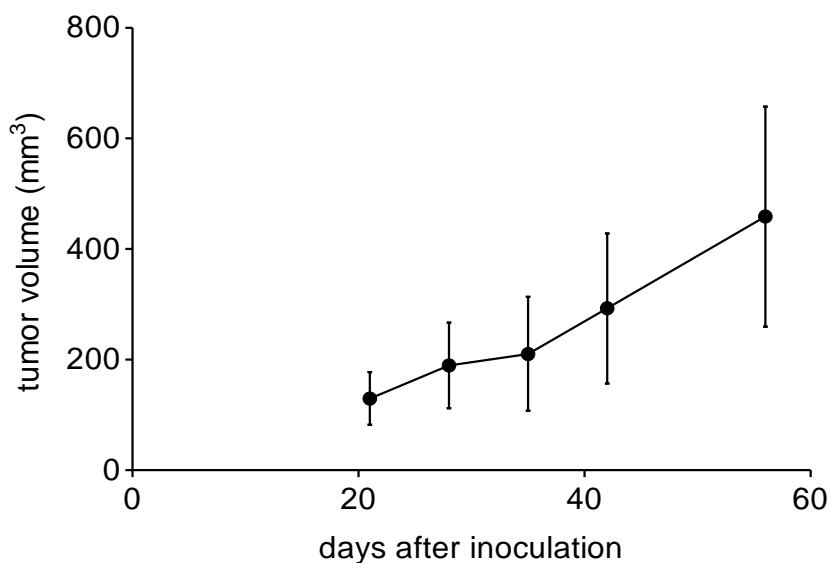


**Figure 39:** Panc-1 SC tumours growth curve expressed in volume (mm<sup>3</sup>) after inoculation of 2 million Panc-1 cells. Dots, mean; lines, SD; n=50.

The graph resembles the initial graph in section 3.3.2 (see Figure 20). Animals bearing homogeneous sized tumours were selected for *in vivo* experiments.

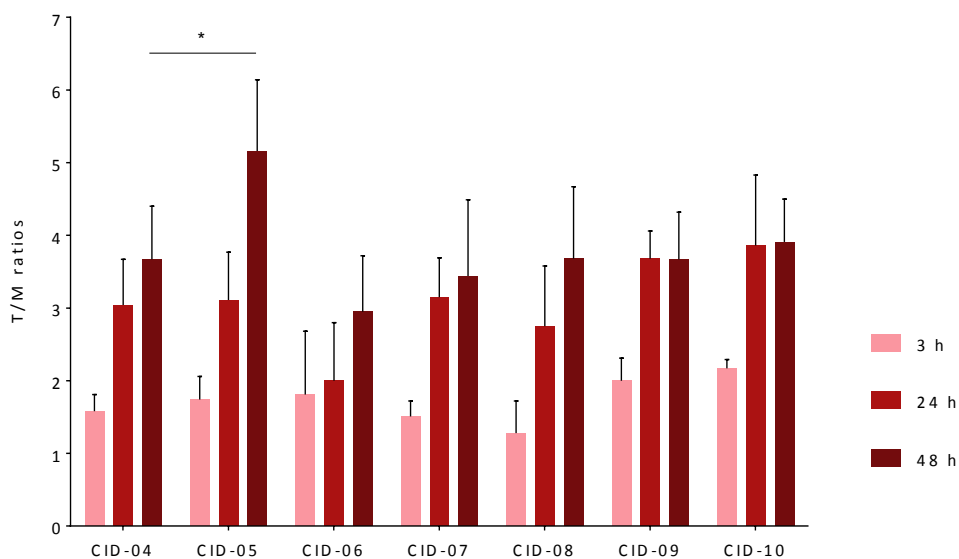
### 4.3.3 *IN VIVO* BIODISTRIBUTION IMAGING STUDIES

#### 4.3.3.1 *SPECT-CT: Biodistribution pattern of the different NPs*

For all NPs and time points, the radioactivity present in the tumour was compared to the amount of radioactivity present in the muscle, and the ratio between these two values was calculated. Tumour-to-muscle ratios, expressed as average  $\pm$  SD are presented and discussed in the following sections.

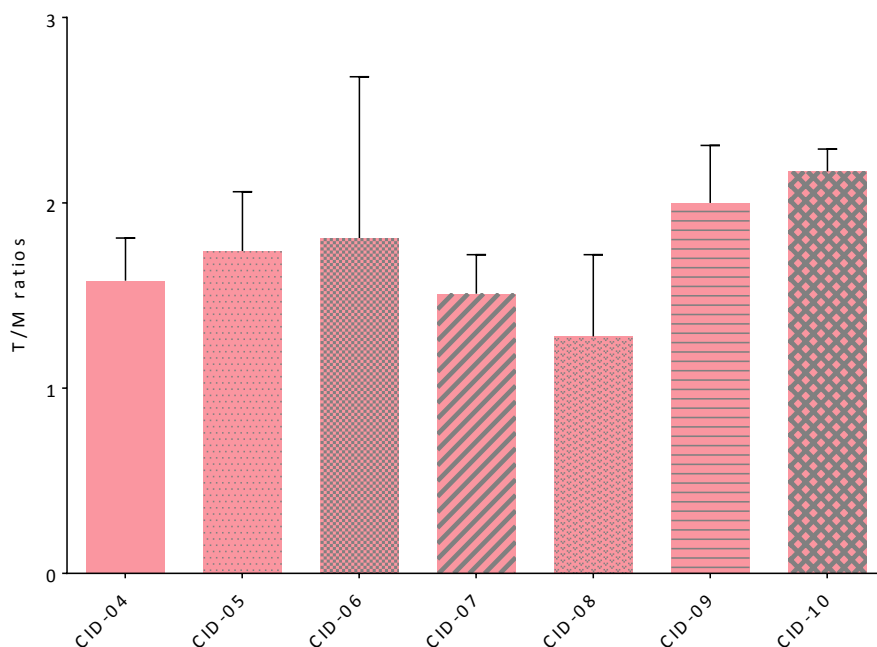
#### *IK4-CIDETEC:*

Figure 40 shows T/M values for all CID particles. In all cases, the results correspond to 5 animals except for CID-07 (n=3).



**Figure 40:** Average T/M ratios for  $^{67}\text{Ga}$ -PNPs in Panc-1 xenografted CD-1 Foxn1 nu/nu mice at 3, 24 and 48 h PI.

Tumour-to-muscle ratios  $t= 3$  hours have been plotted for clarity in Figure 41. The results show a ratio of  $1.58 \pm 0.23$  for the control NPs (CID-04) and  $1.74 \pm 0.32$ ,  $1.81 \pm 0.87$ ,  $1.51 \pm 0.21$ ,  $1.28 \pm 0.44$ ,  $2.00 \pm 0.31$  and  $2.17 \pm 0.12$  for CID-05, CID-06, CID-07, CID-08, CID-09 and CID-10, respectively.



**Figure 41:** Average T/M ratios for  $^{67}\text{Ga}$ -PNPs in Panc-1 xenografted CD-1 Foxn1 nu/nu mice at 3 h PI.

Despite no statistically significant differences were observed at this time point, the results show higher T/M ratios for CID particles tagged with both PTR targeting moieties (CID-05 and CID-09) compared to the control particles (CID-04). The NPs targeted with tPA (CID-06) presented as well a higher accumulation in the tumour but conversely, when these particles were coated with PEG-MMP-substrate-PEG (CID-08), lower T/M ratios were achieved. Surprisingly, the particles tagged with PTR<sub>58</sub> and PEG-coated were the ones which presented the highest T/M ratio at 3 hours time point. The results obtained with the One-Way ANOVA test confirm that the differences

observed at this time point were not significant, and hence no conclusions can be extracted regarding the influence of the decoration on T/M ratios.

Figure 42 shows T/M ratios for the same particles at  $t=24$  hours. Tumour-to-muscle ratios of  $3.04 \pm 0.63$ ,  $3.11 \pm 0.66$ ,  $2.00 \pm 0.80$ ,  $3.15 \pm 0.54$ ,  $2.75 \pm 0.83$ ,  $3.68 \pm 0.38$  and  $3.86 \pm 0.97$  were obtained for CID-04 (control), CID-05, CID-06, CID-07, CID-08, CID-09 and CID-10, respectively.

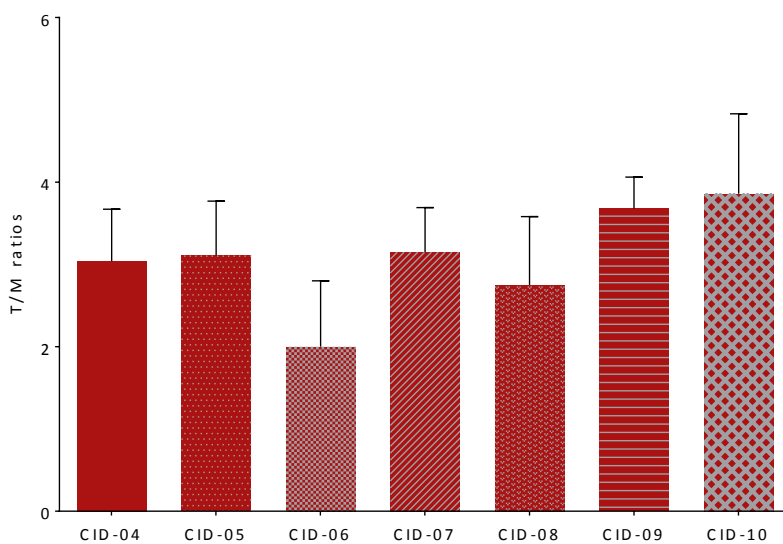


**Figure 42:** Average T/M ratios for  $^{67}\text{Ga}$ -PNPs in Panc-1 xenografted CD-1 Foxn1 nu/nu mice at 24 h PI.

In general terms, the results at  $t=24$  hours show higher T/M ratios than those observed at  $t=3$  hours (see also Figure 40), suggesting a progressive accumulation of the NPs in the tumour tissue. Unfortunately, no statistical differences were obtained among the different NPs, suggesting that surface

decoration seems not to play a pivotal role in the accumulation of the NPs in the tumour at this time point. Noteworthy, decoration of the NPs only with tPA seems to lead to poor accumulation in the tumour (T/M values lower than those obtained for control NPs), while inclusion of both tPA and PEG-MMP-substrate-PEG (CID-08) led to higher T/M values.

In Figure 43, T/M v ratios for the different NPs at t= 48 hours are shown. The results show ratios of  $3.67 \pm 0.73$ ,  $5.16 \pm 0.98$ ,  $2.95 \pm 0.77$ ,  $3.44 \pm 1.05$ ,  $3.68 \pm 0.99$ ,  $3.67 \pm 0.65$  and  $3.91 \pm 0.59$  for CID-04, CID-05, CID-06, CID-07, CID-08, CID-09 and CID-10, respectively.

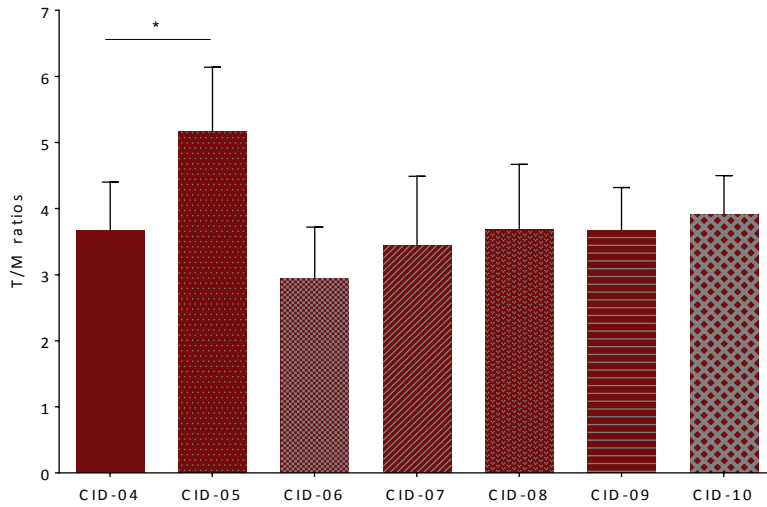


**Figure 43:** Average T/M ratios for  $^{67}\text{Ga}$ -PNPs in Panc-1 xenografted CD-1 Foxn1 nu/nu mice at 48 h pi; \*,  $P \leq 0.05$ .



Statistical analysis of the results confirmed that all T/M values at t= 48 h were equivalent to the T/M ratio obtained for control particles, with the exception of CID-05. For this NP, T/M values were significantly higher ( $P= 0.0264$ ) than the values obtained for control particles at the same time point. These results suggest that CID-05 particles are the most promising for tumour visualization.

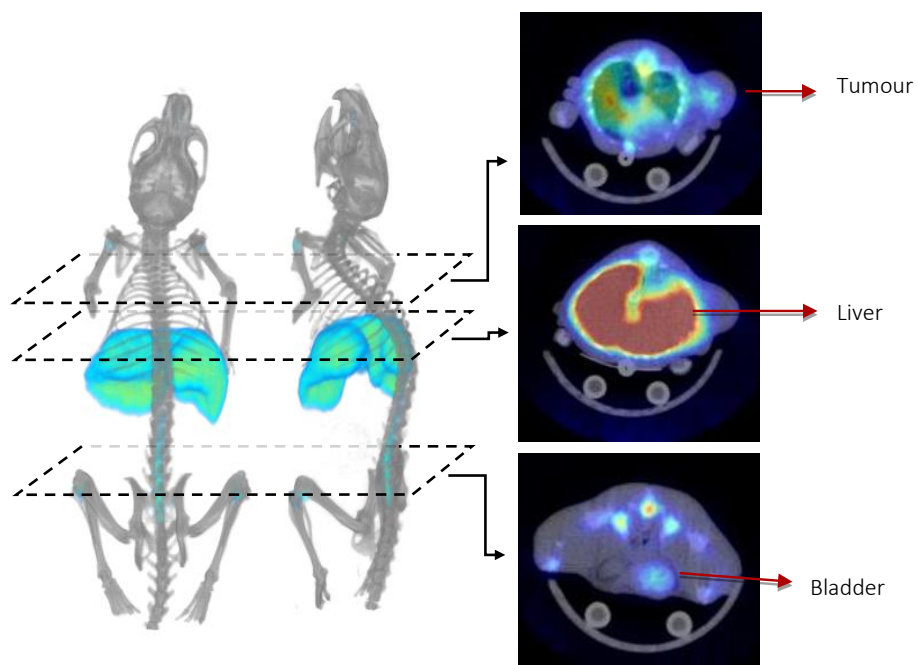


**Figure 44:** SPECT-CT 3D images of  $^{67}\text{Ga}$ -labelled CID-04 at t= 48 hours after intravenous administration. Axial 2D slices show: tumours located in the upper dorsal left part of the animal (top), a transversal section of the liver (middle) and a cut in the inguinal region showing the bladder (bottom).

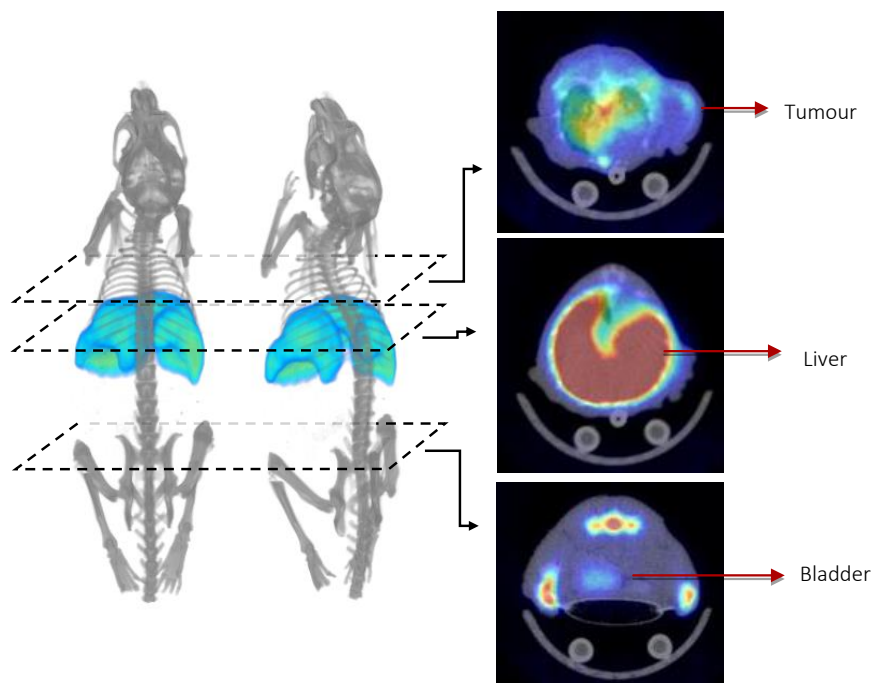


**Figure 45:** SPECT-CT 3D images of  $^{67}\text{Ga}$ -labelled CID-05 at  $t= 48$  hours after intravenous administration. Axial 2D slices show: tumours located in the upper dorsal left part of the animal (top), a transversal section of the liver (middle) and a cut in the inguinal region showing the bladder (bottom).

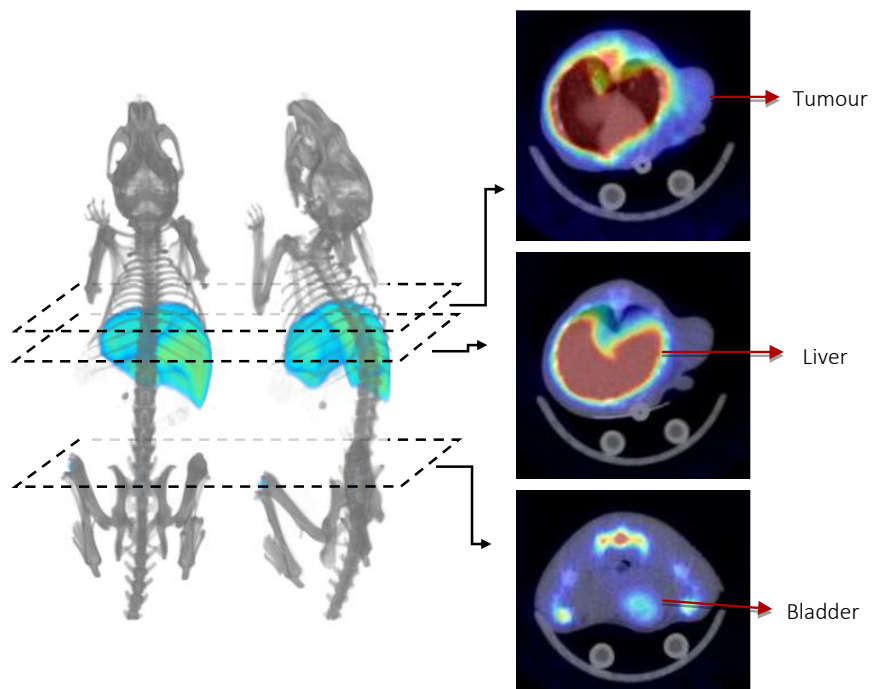


**Figure 46:** SPECT-CT 3D images of  $^{67}\text{Ga}$ -labelled CID-06 at  $t= 48$  hours after intravenous administration. Axial 2D slices show: tumours located in the upper dorsal left part of the animal (top), a transversal section of the liver (middle) and a cut in the inguinal region showing the bladder (bottom).

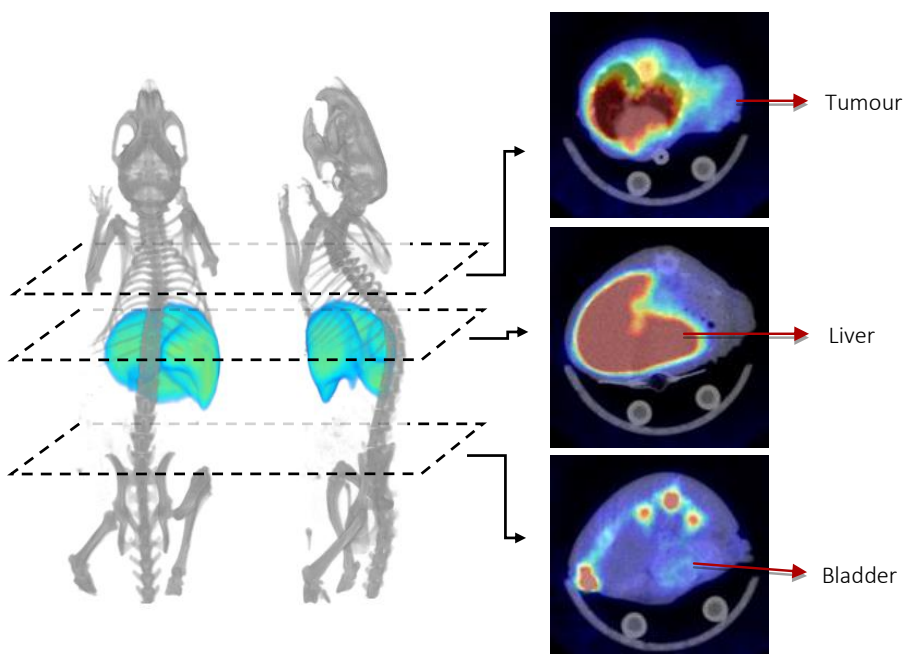


**Figure 47:** SPECT-CT 3D images of  $^{67}\text{Ga}$ -labelled CID-07 at  $t= 48$  hours after intravenous administration. Axial 2D slices show: tumours located in the upper dorsal left part of the animal (top), a transversal section of the liver (middle) and a cut in the inguinal region showing the bladder (bottom).

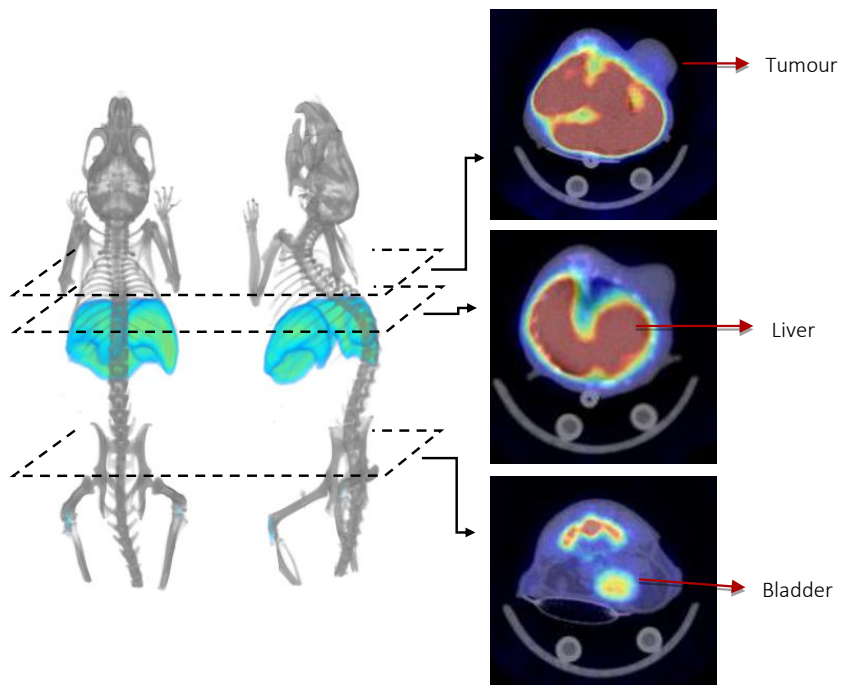


**Figure 48:** SPECT-CT 3D images of  $^{67}\text{Ga}$ -labelled CID-08 at  $t= 48$  hours after intravenous administration. Axial 2D slices show: tumours located in the upper dorsal left part of the animal (top), a transversal section of the liver (middle) and a cut in the inguinal region showing the bladder (bottom).

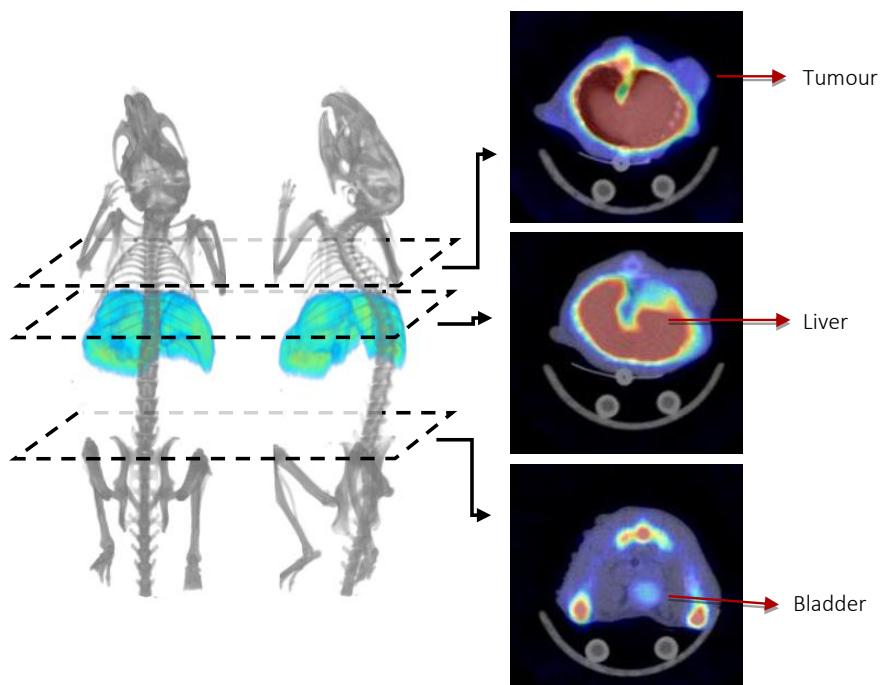


**Figure 49:** SPECT-CT 3D images of  $^{67}\text{Ga}$ -labelled CID-09 at  $t= 48$  hours after intravenous administration. Axial 2D slices show: tumours located in the upper dorsal left part of the animal (top), a transversal section of the liver (middle) and a cut in the inguinal region showing the bladder (bottom).

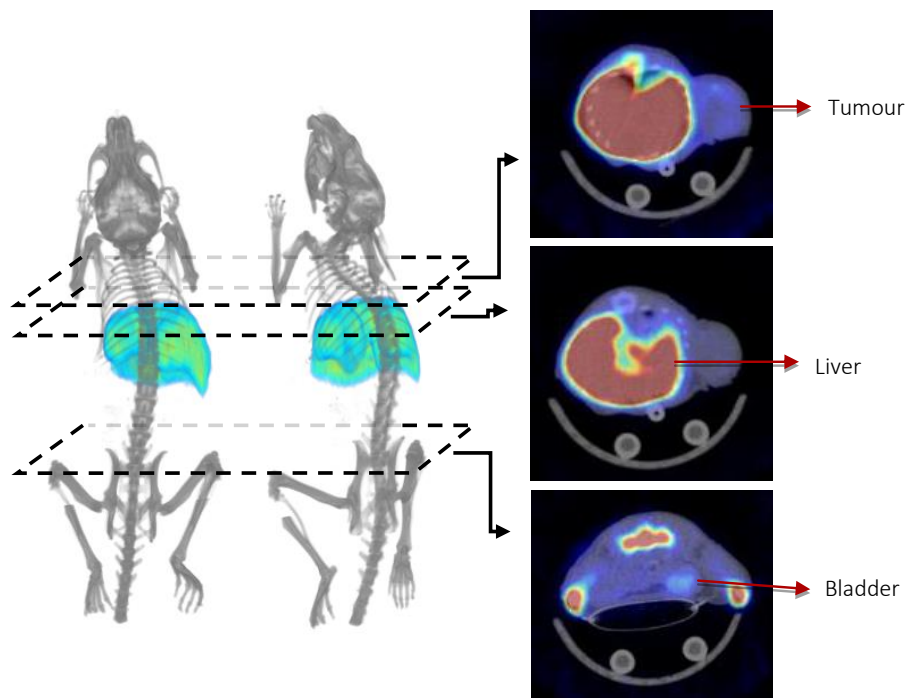


**Figure 50:** SPECT-CT 3D images of  $^{67}\text{Ga}$ -labelled CID-10 at  $t= 48$  hours after intravenous administration. Axial 2D slices show: tumours located in the upper dorsal left part of the animal (top), a transversal section of the liver (middle) and a cut in the inguinal region showing the bladder (bottom).

Besides analysing the values of T/M ratios, it is worth mentioning that visual inspection of the images (see Figures 44-50) showed high accumulation of radioactivity in the organs of the RES, mainly in the liver, suggesting sequestration of the NPs. The inclusion of the PEG decoration on the surface did not result in a significant decrease in liver accumulation. Also, the presence of radioactivity was detected in the bones at  $t>24$ , mainly in the spinal cord. This, together with partial elimination of the radioactivity *via*

urine, suggests the partial detachment of the radiolabel at long times after administration.

GOETHE:

Nanoparticles provided by Goethe were also investigated using 5 animals per NP. Two particles were included: non-functionalized NPs (GU-04, control) and NPs functionalized with PTR<sub>58</sub> (GU-05). Figure 51 shows T/M values obtained for both NPs at different time points after administration. The results showed ratios of  $1.74 \pm 0.32$ ,  $3.20 \pm 1.45$  and  $4.07 \pm 2.32$  for the control NPs (GU-04) at 3, 24 and 48 hours, respectively. Ratios obtained for NPs bearing PTR<sub>58</sub> were  $1.69 \pm 0.58$ ,  $5.24 \pm 2.23$  and  $3.71 \pm 1.00$  at the same time points, respectively. Targeted NPs showed an increase in T/M values from t= 3 hours to t= 24 hours. However, the value decreased at t= 48 hours, while a progressive increase was still observed for control particles (Figure 51). Hence, for GU particles inclusion of the targeting moiety did not result in a positive effect in terms of accumulation of the NPs in the tumour.



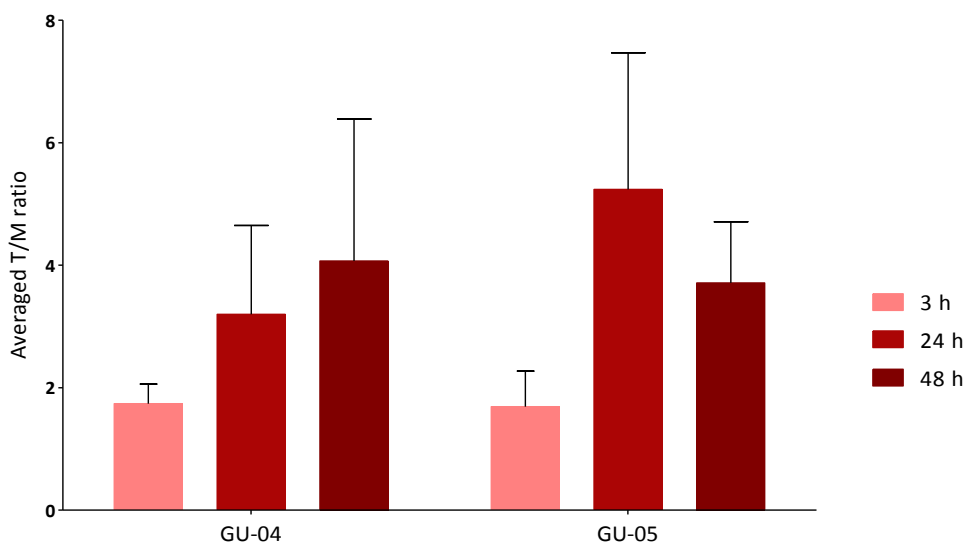


**Figure 51:** Average T/M ratios for  $^{67}\text{Ga}$ -PNPs in Panc-1 xenografted CD-1 Foxn1 nu/nu mice at different time points with GU-04 and GU-05 particles.

Visual inspection of the SPECT images showed a high accumulation of NPs in the liver, suggesting sequestration by the organs of the RES. Accumulation in the spleen could also be detected. The bone uptake was not significant, but the radioactivity was partially eliminated by urine, suggesting detachment of the radiolabel (see Figures 52-53).

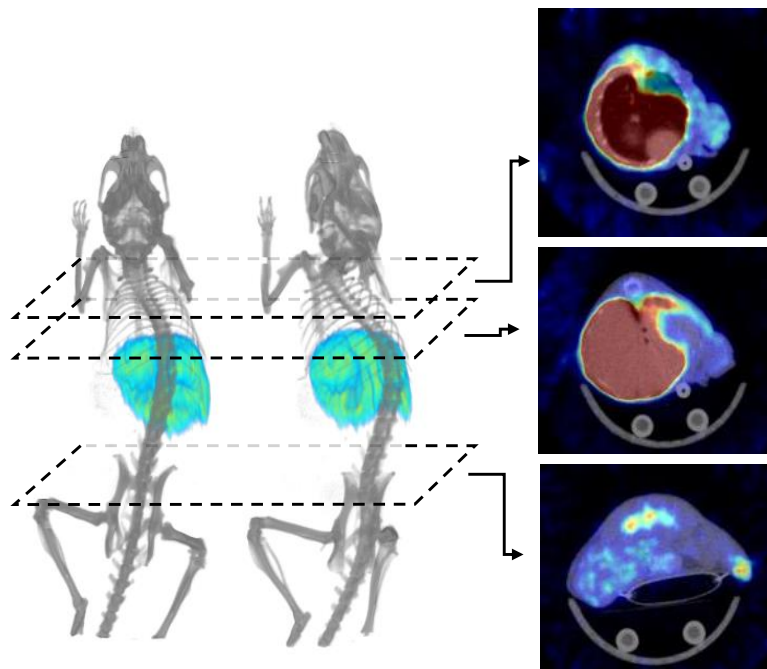


**Figure 52:** SPECT-CT 3D images of  $^{67}\text{Ga}$ -labelled GU-04 at  $t= 48$  hours after intravenous administration. Axial 2D slices show: tumours located in the upper dorsal left part of the animal (top), a transversal section of the liver (middle) and a cut in the inguinal region showing the bladder (bottom).

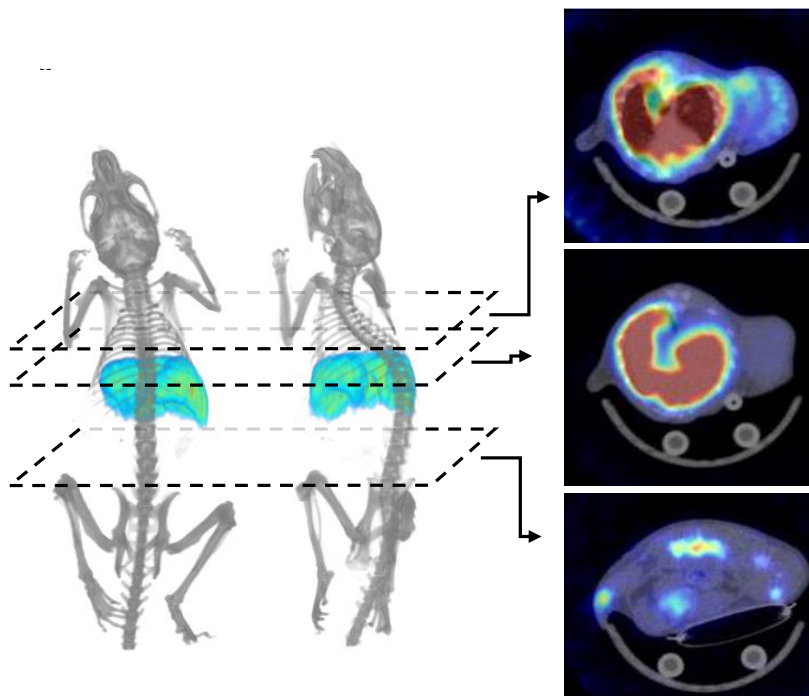


**Figure 53:** SPECT-CT 3D images of  $^{67}\text{Ga}$ -labelled GU-05 at  $t= 48$  hours after intravenous administration. Axial 2D slices show: tumours located in the upper dorsal left part of the animal (top), a transversal section of the liver (middle) and a cut in the inguinal region showing the bladder (bottom).

#### 4.4 CONCLUSIONS

Both CID and GU particles could be efficiently labelled with Gallium-67. The radiochemical integrity of the radiolabelled nanosystems in the presence of saline showed excellent results. However, the presence of a competitor in the incubation media resulted in poor stability of the radiolabel at long times of incubation.

Proper planning of the experimental set up enabled the administration of higher radioactive doses aiming to achieve higher quality images in similar acquisition times.

After intravenous administration, all NPs accumulated in the organs of the RES, mainly the liver and the spleen, irrespective of the time after administration. Nanoparticles provided by CID targeted with PTR<sub>86</sub> showed the best results in terms of T/M ratio at t= 48 hours after administration. The use of the novel somatostatin analogue (PTR<sub>58</sub>), tPA or PEG-MMP-substrate-PEG did not significantly improve selective accumulation of the NPs in the tumour tissue. In the NPs provided by GU, the inclusion of the targeting moiety did not result in an improvement in terms of T/M ratios increase with respect to control particles.

## 5. GENERAL DISCUSSION



Molecular imaging techniques are perceived as valuable tools in the process of drug development. When properly applied, molecular imaging techniques may aid in the identification of non-viable drug candidates at earlier stages of the development process, the determination of the pharmacokinetic properties or the adjustment of the effective dose. Indeed, the scientific literature is full of examples proving the suitability of different imaging modalities, and especially nuclear imaging, to assess the pharmacokinetic properties and predict the therapeutic efficacy of a wide variety of drug candidates, including small organic molecules (113–115), peptides (41,116), proteins (117), and antibodies (118,119), among others.

With the recent emergence of nanotechnology, novel nanomedicines aiming at increasing therapeutic efficacy while minimizing toxic or side effects are continuously being developed. Of note, the investigation of their pharmacokinetic properties, eventual toxicity and therapeutic efficacy is extremely complicated. In this scenario, consolidated technologies such as molecular imaging techniques need to be adapted and properly applied, in order to provide suitable and cost-efficient tools for the screening of newly developed nanomedicines.

In this European project, we were given the unique opportunity to apply a combination of *in vivo* imaging techniques in the pre-clinical screening of multi-functionalized engineered NPs of different nature, with the final

objective of selecting the most promising candidate/s for future application in the treatment of pancreatic cancer. The strategy, as described in the work description of the original project, was quite straightforward: Five partners should develop different core particles, and two more partners should design, synthesize and test different targeting moieties with high affinity for specific receptors over-expressed in pancreatic cancer cells, namely SSTRs and Gal-1 receptors. By combination of the above, a plethora of NPs would result, after appropriate *in vitro* testing, into a short list of promising NPs to be tested *in vivo* in our facilities. Because most of the NP cores designed by the partners contained iron oxide NPs, suitable to be used as contrast agents in MRI, this imaging modality was one of the selected ones for the multimodal *in vivo* evaluation. Additionally, bifunctional chelators were attached to the NP surface to enable subsequent radiolabelling using a radiometal and investigation using nuclear imaging.

The work performed by Save Me partners resulted in a short list of 15 particles that required *in vivo* evaluation in order to select the most promising candidate/s, and the first task to be tackled by CIC biomaGUNE consisted of selecting the most appropriate core and the most appropriate targeting moiety to maximize the accumulation of NPs in the tumour after intravenous administration, using an animal tumour model mimicking those tumours commonly found in humans.



In this context, the first decision to be made was the selection of the tumour model. As it has been mentioned in the introduction, the most common pancreatic cancer in humans is the pancreatic adenocarcinoma. This cancer accounts for > 85 % of all pancreatic cancers, and usually is diagnosed at late stages where resection is not viable due to metastasis (5,16). Hence, in a consensus decision with other partners involved in the consortium, Panc-1 cell line was selected to generate the animal model. The subcutaneous tumour model using this cancer cells from human origin is known to form a dense stroma poorly vascularised. Hence, low accumulation of any injected drug could be anticipated. However, despite compromising the final results, this tumour model was selected because it has proven appropriate to mimic the behaviour of human pancreatic adenocarcinomas (101,119). Additionally, this cell line is the one affecting more individuals' compared to any other (101). Finally, PANC-1 cells over-express different SSTR subtypes and Gal-1 receptor, targeted by the ligands developed within the consortium.

The subcutaneous inoculation was selected because monitoring of the tumour size and determination of the appropriate time-window to conduct imaging studies is simpler. Additionally, from an ethical point of view, subcutaneous tumour models have proven to cause less pain and distress to the animals than other models (120).

After deciding the animal model, implementation of the appropriate inoculation procedure was paramount. The number of cells to be injected required careful refinement in order to achieve a progressive and smooth tumour growth, which should be sufficiently slow to enable a proper planning and execution of the imaging studies. Hence, experiments in which different numbers of cells were inoculated into the animals were started, and the growth curve was determined. For these experiments, appropriate selection of the number of animals was essential in order to respect the concept of Reduction, while ensuring a sufficient number of animals to achieve statistically significant results. From literature data (101), 500 K, 1 M and 2 M cells were selected as starting points, and 10 animals were used per number of cells. Tumour growth curves showed that optimal tumour growth to conduct imaging experiments was achieved with inoculation of 2 M cells.

The number of animals to be used in the initial screening of the NPs provided by all partners was severely limited for technical reasons. Imaging studies to select the best candidates had to be conducted in a short period of time, in order to provide scientific evidences to ensure that non-promising candidates were identified without compromising the time-lines of the whole project. Additionally, only one MRI, one SPECT and one PET cameras were available at that time, with the consequent limitation in terms of throughput. Considering these factors and taking into account that 15 particles had to be investigated, only 2 animals were investigated per NP.

Selection of the imaging modality was one of the most critical points in the execution of the project. In principle, one nuclear imaging modality and MRI were to be used. Hence, in the first screening (chapter 3) both MRI and nuclear imaging were used. The selection of SPECT as the nuclear imaging technique was based on technical aspects. First, we decided to use the same imaging modality for all NPs, in order to prevent technology-related differences which may bias our final decisions. Second, and due to the long biological half-life of NPs after administration in the organism (31,110), long-lived radionuclides were required to conduct imaging studies in the appropriate time-window. The production of long-lived positron emitters (e.g.  $^{64}\text{Cu}$ ,  $^{89}\text{Zr}$ ,  $^{124}\text{I}$ ) was not feasible at that time in our institution and acquisition from commercial suppliers was extremely expensive. Hence, PET was discarded and the decision was simplified. To our understanding, it was also essential to use the same labelling strategy and the same radionuclide for all the particles. The selected radionuclide should fulfil the following requirements: (i) have long half-life, for the reasons mentioned above; (ii) have a maximum energy emission within the energy window of our SPECT camera (25-250 keV); and (iii) be available from commercial suppliers at reasonable cost. The selected candidate was  $^{67}\text{Ga}$ . Despite it was provided as the citrate salt, which is not optimal to approach subsequent labelling using bifunctional chelators, it could be easily converted into the chloride form following a previously established method (97). This method was implemented and further optimized in our lab.

NPs provided by the partners were decorated with a bifunctional chelator to enable incorporation of the radionuclide. The chelators were selected by the individual partners in charge of NP preparation, following indications provided from CIC biomaGUNE. Basically, and relying on literature data (79,121), NOTA or DOTA analogues were used by all the partners. These chelators form stable complexes with strong cations such as Ga(III) (69,71,122). For the radiolabelling of the NPs, experimental conditions required optimization on an individual basis, although the same general protocol was followed in all cases: incubation with the radionuclide, purification by centrifugal filtration and repeated washing. Incubation time, temperature and media were modified until satisfactory conditions were achieved. It is worth mentioning that radiochemical processes were not fully optimized. In other words, radiochemical yields reported in this work might be improved by fine tuning of the experimental conditions. However, it is a cost-efficient general practice in radiochemistry to use experimental conditions which are sufficient to approach subsequent steps.

SPECT and MRI studies were conducted in parallel in the first *in vivo* screening. Magnetic resonance imaging results showed promise in the determination of the regional distribution of the NPs within the tumour at different time points after administration, thanks to the exceptional spatial resolution of the technique (123,124). Indeed, data obtained from MRI studies confirmed the uptake of some of the NPs in the tumour tissue, and

distribution within the tumour could be determined at the sub-millimetre scale. However, the low sensitivity and the lack of an efficient methodology for the accurate quantification of the images forced the discontinuation of its use. Simply, it was not the optimal tool to achieve the objectives of this work (mainly, to quantify the accumulation of the different NPs in the tumour), although the complementary information provided by MRI images was extremely useful to better understand the behaviour of the NPs *in vivo*.

Contrary to MRI, SPECT images enabled the relative quantification of the accumulation of the labelled NPs in the tumour at different time points after administration, as well as complementary information related to the general biodistribution of the NPs and accumulation in major organs, such as the liver. It is worth mentioning that despite the original idea was to get absolute quantitative data of the accumulation of the NPs in the tumour, absolute quantification was extremely challenging and not reliable in our configuration. Indeed, it is well known that absolute quantification of SPECT data is extremely challenging (49). For this reason, relative quantitative analysis was carried out. With that aim, the ratio between the tumour and a region of reference was determined. As the region of reference, the muscle was selected because the SST and Gal-1 receptors are known to be poorly expressed in this tissue (104,125).

One of the key parameters in the use of nuclear imaging for the investigation of the biodistribution of radiolabelled NPs using nuclear imaging is the radiochemical stability of the labelled particles. The release of the label from the NP may lead to wrong results. Hence, after the radiolabelling, the radiochemical stability of all particles was investigated *in vitro*. As it has been shown in both chapters (3 and 4), the labelled NPs proved to be radiochemically stable in physiologic saline solution. However, with the presence of a competitor in the incubation media at a high concentration, a significant release of the radiolabel was observed. These results cannot be directly extrapolated to *in vivo* conditions, where many factors may influence the stability of the NPs. However, it is worth mentioning that the development of radiolabelling strategies leading to more stable nanosystems even in the presence of a chelator in the incubation media should be considered in future studies.

The investigation of the different NPs (targeted and non targeted NPs) using just 2 animals per NP type allowed us to create a ranking of the potential of each NP to accumulate in the tumour, and further select the best candidates in terms of core material and targeting moieties. Despite the results were not statistically significant, the experience of the imaging team and the observed trends allowed us to make a compromise decision: One core particle (cross-linked polymeric NPs, provided by partner CID) and 2 targeting moieties (one SST analogue and one ligand for Gal-1) were selected. A second NP core

(protein-based NPs, provided by partner GU) was also selected for the final screening.

After the first *in vivo* screening and selection of the most appropriate cores and targeting moieties, the next step was clearly identified: *In vivo* studies were to be repeated but with a higher number of animals, in order to have more reliable data about the accumulation of the NPs in the tumour. Additionally, two new factors were introduced by the consortium: decoration of the NP surface with a PEG-based protective shell, and inclusion of a new SSTR ligand, recently developed by one of the partners of the consortium. The inclusion of the PEG chain aimed at prolonging the circulation time of the NPs in the bloodstream, and consequently the bioavailability of the NPs (126). Additionally, and in order to favour the internalization of the NPs in the tumour cells, the PEG chain was linked to the NP via an MMP substrate, in order to favour cleavage in the immediacy of the tumour cells with the consequent reduction of particle size. Despite nuclear imaging techniques do not have enough resolution to determine if the NPs are inside or outside the cells, a favoured internalization in the tumour cells should result in a higher accumulation of the NPs in the tumour.

In order to guarantee the consistency of the results, our decision was not to change the experimental approach. In other words, SPECT was used as the imaging modality, radiolabelling was performed using the formation of

chelator-radiometal complexes and relative quantification was applied on the images. In order to increase the statistical power of the results, five animals were used per NP in this case.

Radiolabelling efficiencies of the best candidates developed to conduct the studies of chapter 4 showed to be good, following the same experimental procedures conducted for their analogue particles used in chapter 3. In great agreement with the results obtained when checking radiochemical integrity with compounds in chapter 3, there was a decrease in stability when putting in contact the NPs with a competing media. The newly developed targeting moiety based on SST affinity, i.e., PTR<sub>58</sub>, did not show a particular improvement in tumour targeting with respect to the firstly developed analogue. A proper planning of the experimental set up lead to higher injected doses and consequently, to shorter image acquisitions to achieve images of similar quality. In general, CID's particles showed higher tumour to muscle ratios compared to GU's particles and although the addition of a PEG-MMPsubstrate-PEG ligand was a priori thought to improve access to tumours, SPECT imaging did not apparently demonstrate this fact compared to CID-02 particles (used in chapter 3).

To sum up, different NPs were prepared and characterized based on iron oxide cores or a polymeric core, coated with polymers and including agents targeting receptors over-expressed in pancreatic cancer cells. An animal



tumour model was developed out of a human derived adenocarcinoma by SC inoculation of Panc-1 cells into the animal's flanks.

Radiolabelling with gamma emitters was conducted and SPECT-CT images acquired in order to calculate the tumour uptake of the different developed systems. MRI images were also performed to determine the morphology and expected heterogeneity and uptake of NPs in tumours. The effects of targeting ligands were investigated during this work and as a result, SST-based targeting agents have been highlighted as optimal ligands to hit pancreatic cancer cells. Altogether, polymeric NPs showed a greater access to tumours and CID partner's NPs have been suggested as potential therapeutic or diagnostic tools in the context of pancreatic cancer.



## 6. FINAL CONCLUSIONS



1. [<sup>67</sup>Ga]Gallium citrate can be efficiently converted into the chloride form by following an easy to automate, solid phase extraction-based methodology.
2. Polymeric and protein-based NPs bearing chelating agents on the surface can be efficiently labelled with <sup>67</sup>Ga by incubation with [<sup>67</sup>Ga]GaCl<sub>3</sub> under different experimental conditions (pH, temperature and time) depending on the properties of the NPs. The presence of the chelator is not necessary for the radiolabelling of polymeric NPs containing iron oxide NPs entrapped into the polymeric core.
3. NPs labelled following the strategy mentioned above are radiochemically stable in physiologic saline solution, where detachment of the radiolabel is not significant after 48 hours. The stability was significantly lower in the presence of a competitor (chelator) in the incubation media.
4. Subcutaneous inoculation of 2x10<sup>6</sup> M Panc-1 cells in athymic nude mice resulted in the formation of tumours. The exponential tumour growth yielded 150 mm<sup>3</sup> tumours in 6-8 weeks, which was appropriate to approach subsequent longitudinal imaging studies using either nuclear imaging or Magnetic Resonance Imaging.
5. After intravenous administration, labelled NPs accumulated majorly in the organs of the reticuloendothelial system, mainly liver and spleen, irrespective of surface decoration, particle size and composition of the core. Minor elimination of the radioactivity via the urinary system

- suggests detachment of the radiolabel *in vivo* or low stability of the NPs.
6. Magnetic Resonance Imaging is a suitable technique to qualitatively assess the spatiotemporal biodistribution of the NPs after intravenous administration, providing relevant information regarding the local distribution within the tumour. Nanoparticles provided by partners BIU and GU showed non homogeneous distribution within the tumour at  $2 < t < 24$  h post injection.
  7. After intravenous administration, tumour-to-muscle ratios determined by SPECT/CT progressively increased with time, irrespective of surface decoration and composition of the NP core. Inclusion of PTR<sub>86</sub> as the targeting moiety resulted in non-statistically significant enhanced tumour-to-muscle ratios with respect to control particles. Incorporation of tPA as the targeting moiety did not result in improved pharmacokinetic properties. Incorporation of the targeting agent PTR<sub>58</sub> improved tumour accumulation with respect to control particles, although better results were obtained with PTR<sub>86</sub>.
  8. Incorporation of a decoration on the surface of the NPs based on an MMP-substrate sandwiched between two PEG chains did not result in improved imaging capabilities of the NPs.
  9. NPs provided by CID partner bearing PTR<sub>86</sub> as the targeting moiety showed the highest T/M ratios among all NPs tested in the frame of this PhD thesis. This, in combination with lower liver uptake, turns

these NPs into the most promising ones for proper tumour visualization.





## 7. CONCLUSIONES FINALES



1. Mediante un sencillo método fácil de automatizar basado en la extracción en fase sólida, el citrato de [ $^{67}\text{Ga}$ ] galio puede convertirse en su forma clorada.
2. Las nanopartículas poliméricas y las nanopartículas a base de proteínas con agentes bifuncionales anclados en su estructura, pueden ser marcadas eficientemente con  $^{67}\text{Ga}$ , incubándolas con [ $^{67}\text{Ga}$ ]GaCl<sub>3</sub> bajo distintas condiciones experimentales (pH, temperatura y tiempo) dependiendo de las propiedades de las NPs. La presencia de agentes quelantes no resulta necesaria para el marcaje de NPs poliméricas que contengan en su núcleo nanopartículas de óxido de hierro.
3. Las NPs marcadas mediante la estrategia mencionada anteriormente, son estables radioquímicamente hablando en una solución de suero salino fisiológico, en la que la separación del trazador no resulta significativa tras 48 horas. La estabilidad resultó ser significativamente menor en presencia de un competidor (agente quelante) en el medio de incubación.
4. La inoculación subcutánea de  $2 \times 10^6$  M de células Panc-1 formó los tumores. El crecimiento exponencial de los mismos, originó tumores de 150 mm<sup>3</sup> en volumen en 6-8 semanas, tamaño que resultó apropiado para la realización de estudios de imagen longitudinales mediante técnicas de imagen nuclear o imagen por resonancia magnética.

5. Tras la administración intravenosa, las NPs marcadas se acumularon en su mayoría en los órganos del sistema retículo-endotelial, principalmente en hígado y bazo, con independencia de la decoración superficial de las NPs, el tamaño de partícula o la composición del núcleo de las mismas. La minoritaria excreción por vía urinaria observada, sugiere la liberación del radionucleido *in vivo* o una baja estabilidad de las NPs.
6. La imagen por resonancia magnética es una técnica adecuada para determinar la biodistribución espacio-temporal de las NPs tras su administración intravenosa, proporcionando información relevante con respecto a la distribución local en el tumor. Las nanopartículas suministradas por los miembros BIU y GU, mostraron una distribución no homogénea en el tumor de  $2 < t < 24$  h tras su inyección.
7. Tras la administración intravenosa en los estudios realizados mediante SPECT/CT, se determinaron los ratios de tumor respecto a músculo, en los que se observó que aumentaban progresivamente con el tiempo, con independencia de la decoración superficial y la composición del núcleo de la NP. La adición de agentes específicos para tumores pancreáticos como el PTR<sub>86</sub>, no resultó ser estadísticamente significativa en cuanto al ratio tumor/músculo se refiere en comparación con las NPs control. La incorporación de tPA como agente específico, no mejoró las propiedades farmacocinéticas. La incorporación del agente específico para tumores de origen

pancreático PTR<sub>58</sub>, mejoró la acumulación en tumor con respecto a las NPs control, aunque se obtuvieron resultados mejores con el derivado PTR<sub>86</sub>.

8. La adición de un substrato capaz de ser reconocido por enzimas metaloproteinasas entre dos cadenas de PEG como funcionalización, no resultó en una mejora significativa de la capacidad de trazado de las NPs mediante SPECT-CT.
9. Las NPs proporcionadas por el grupo CID funcionalizadas con el agente específico PTR<sub>86</sub> mostraron los ratios T/M mayores entre todas las NPs ensayadas durante la tesis doctoral. Este hecho, en combinación con la menor captación en hígado, hace que sean éstas las NPs más prometedoras para la adecuada visualización de los tumores pancreáticos.



## 8. BIBLIOGRAPHY





## BIBLIOGRAPHY

---

1. NIH National Cancer Institute [Internet]. [cited 2015 Dec 11]. Available from: <http://www.cancer.gov>
2. WHO. Globocan 2012: Estimated Cancer Incidence, Mortality and Prevalence Worldwide in 2012 [Internet]. International Agency for Research on Cancer. [cited 2015 Dec 18]. Available from: [http://globocan.iarc.fr/Pages/fact\\_sheets\\_cancer.aspx](http://globocan.iarc.fr/Pages/fact_sheets_cancer.aspx)
3. Hariharan D, Saied A, Kocher HM. Analysis of mortality rates for pancreatic cancer across the world. *HPB*. 2008;10(1):58–62.
4. American Cancer Society: Cancer Facts and Figures 2015 [Internet]. [cited 2015 Dec 12]. p. 1–54. Available from: <http://www.cancer.org/research/cancerfactsstatistics/cancerfactsfigures2015/>
5. Chan A, Diamandis EP, Blasutig IM. Strategies for discovering novel pancreatic cancer biomarkers. *J Proteomics*. 2012;81(6):126–34.
6. Jaidev LR, Krishnan UM, Sethuraman S. Gemcitabine loaded biodegradable PLGA nanospheres for *in vitro* pancreatic cancer therapy. *Mater Sci Eng C*. 2015;47:40–7.
7. Stathis A, Moore MJ. Advanced pancreatic carcinoma: current treatment and future challenges. *Nat Rev Clin Oncol*. 2010;7(3):163–72.
8. Drake RL, Vogl W, Tibbitts AWMM, Richard Richardson P. *Gray's anatomy for students*. Philadelphia: Elsevier/Churchill Livingstone.; 2005. 288–290, 297, 303 p.
9. Pancreatic Cancer Action Network [Internet]. [cited 2015 Apr 12]. Available from: <https://www.pancan.org/section-facing-pancreatic-cancer/learn-about-pan-cancer/what-is-the-pancreas/>
10. Olof E, Selvaraju RK, Johansson L, Eriksson HW, Sundin A, Gunnar A, et al. Quantitative Imaging of Serotonergic Biosynthesis and Degradation in the Endocrine Pancreas. *J Nucl Med*. 2014;55(6):1–6.
11. Ito T, Igarashi H, Jensen RT. Pancreatic neuroendocrine tumors: Clinical features, diagnosis and medical treatment: *Advances*. *Best Pract Res Clin Gastroenterol*. 2012;26(6):737–53.
12. Capozzi M, Caterina I, De Divitiis C, von Arx C, Maiolino P, Tatangelo F, et al. Everolimus and pancreatic neuroendocrine tumors (PNETs): Activity, resistance and how to overcome it. *Int J Surg*. 2015;21(1):S89–94.

## BIBLIOGRAPHY

---

13. Zakhari S. Chronic alcohol drinking: Liver and pancreatic cancer? *Clin Res Hepatol Gastroenterol*. 2015;39(1):S86–91.
14. Preziosi G, Oben JA, Fusai G. Obesity and pancreatic cancer. *Surg Oncol*. 2014;23(2):61–71.
15. Shah S, Morteale KJ. Uncommon Solid Pancreatic Neoplasms: Ultrasound, Computed Tomography, and Magnetic Resonance Imaging Features. *Semin Ultrasound, CT MRI*. 2007;28(5):357–70.
16. Yang F, Jin C, Subedi S, Lee CL, Wang Q, Jiang Y, et al. Emerging inorganic nanomaterials for pancreatic cancer diagnosis and treatment. *Cancer Treat Rev*. 2012;38:566–79.
17. Oettle H. Progress in the knowledge and treatment of advanced pancreatic cancer: From benchside to bedside. *Cancer Treat Rev*. 2014;40(9):1039–47.
18. Sanchez Cabus S, Fernandez-Cruz L. Surgery for pancreatic cancer: Evidence-based surgical strategies. *Cir Esp*. 2015;93(7):423–35.
19. Marmor S, Burke EE, Portschy PR, Virnig BA, Jensen EH, Tuttle TM. Lymph node evaluation for treatment of adenocarcinoma of the pancreas. *Surg Oncol*. 2015;24(3):284–91.
20. Wingren C, Sandström A, Segersvärd R, Carlsson A, Andersson R, Löhr M, et al. Identification of serum biomarker signatures associated with pancreatic cancer. *Cancer Res*. 2012;72(10):2481–90.
21. Bergmann L, Maute L, Heil G, Rüssel J, Weidmann E, Köberle D, et al. A prospective randomised phase-II trial with gemcitabine versus gemcitabine plus sunitinib in advanced pancreatic cancer: a study of the CESAR Central European Society for Anticancer Drug Research-EWIV. *Eur J Cancer*. 2015;51(1):27–36.
22. Lepage C, Capocaccia R, Hackl M, Lemmens V, Molina E, Pierannunzio D, et al. Survival in patients with primary liver cancer, gallbladder and extrahepatic biliary tract cancer and pancreatic cancer in Europe 1999-2007: Results of EUROCARE-5. *Eur J Cancer*. 2015;51:2169–78.
23. Li Q, Yuan Z, Yan H, Wen Z, Zhang R, Cao B. Comparison of Gemcitabine Combined With Targeted Agent Therapy Versus Gemcitabine Monotherapy in the Management

## BIBLIOGRAPHY

---

- of Advanced Pancreatic Cancer. *Clin Ther.* 2014;36(7):1054–63.
24. Chatterjee K, Sarkar S, Rao KJ, Paria S. Core/shell nanoparticles in biomedical applications. *Adv Colloid Interface Sci.* 2014;209:8–39.
  25. Perez-Campaña C, Gomez-Vallejo V, Martin A, San Sebastian E, Moya SE, Reese T, et al. Tracing nanoparticles *in vivo*: a new general synthesis of positron emitting metal oxide nanoparticles by proton beam activation. *Analyst.* 2012;137(21):4902–6.
  26. Mahmoudi M, Lynch I, Ejtehadi MR, Monopoli MP, Bombelli FB, Laurent S. Protein-Nanoparticle Interactions: Opportunities and Challenges. *Chem Rev.* 2011;111(9):5610–37.
  27. Ediriwickrema A, Saltzman WM. Nanotherapy for Cancer: Targeting and Multifunctionality in the Future of Cancer Therapies. *ACS Biomater.* 2015;1:64–78.
  28. Maeda H, Matsumura Y. EPR effect based drug design and clinical outlook for enhanced cancer chemotherapy. *Adv Drug Deliv Rev.* 2011;63(3):129–30.
  29. Kaltsas GA, Papadogias D, Makras P, Grossman AB. Treatment of advanced neuroendocrine tumours with radiolabelled somatostatin analogues. *Endocr Relat Cancer.* 2005;12:683–99.
  30. Wang M, Thanou M. Targeting nanoparticles to cancer. *Pharmacol Res.* 2010;62(2):90–9.
  31. Alexis F, Pridgen E, Molnar LK, Farokhzad OC. Factors Affecting the Clearance and Biodistribution of Polymeric Nanoparticles. *Mol Pharm.* 2008;5(4):505–15.
  32. Wicki A, Witzigmann D, Balasubramanian V, Huwyler J. Nanomedicine in cancer therapy: Challenges, opportunities, and clinical applications. *J Control Release.* 2015;200:138–57.
  33. Yang J, Kopeček J. Macromolecular therapeutics. *J Control Release.* 2014;190:288–303.
  34. Kocbek P, Kralj S, Kreft ME, Kristl J. Targeting intracellular compartments by magnetic polymeric nanoparticles. *Eur J Pharm Sci.* 2013;50(1):130–8.
  35. Breeman WAP, Blois E De, Chan HS, Konijnenberg M, Kwekkeboom DJ, Krenning EP. <sup>68</sup>Ga-labeled DOTA-Peptides and <sup>68</sup>Ga-labeled Radiopharmaceuticals for Positron

## BIBLIOGRAPHY

---

- Emission Tomography: Current Status of Research, Clinical Applications, and Future Perspectives. *Semin Nucl Med.* Elsevier Inc.; 2011;41(4):314–21.
36. Lamesa C, Rauscher A, Lacoeyille F, Desruet M. <sup>68</sup>Ga somatostatin analog radiolabelling: The radiopharmacist's point of view. *Med Nucl.* 2015;39(1):3–10.
37. Okarvi SM. Peptide-based radiopharmaceuticals and cytotoxic conjugates: Potential tools against cancer. *Cancer Treat Rev.* 2008;34:13–26.
38. Ginj M, Schmitt JS, Chen J, Waser B, Reubi J-C, De Jong M, et al. Design, Synthesis, and Biological Evaluation of Somatostatin-Based Radiopeptides. *Chem Biol.* 2006;13:1081–90.
39. Van Eijck CHJ, De Jong M, Breeman WAP, Slooter GD, Marquet RL, Krenning EP. Somatostatin receptor imaging and therapy of pancreatic endocrine tumors. *Ann Oncol.* 1999;10(4):177–81.
40. Reichert DE, Lewis JS, Anderson CJ. Metal complexes as diagnostic tools. *Coord Chem Rev.* 1999;184:3–66.
41. Montet X, Weissleder R, Josephson L. Imaging Pancreatic Cancer with a Peptide-Nanoparticle Conjugate Targeted to Normal Pancreas. *Bioconjug Chem.* 2006;17:905–11.
42. Zeglis BM, Lewis JS. A practical guide to the construction of radiometallated bioconjugates for positron emission tomography. *Dalt Trans.* 2011;40:6168–95.
43. Uehara TM, Marangoni VS, Pasquale N, Miranda PB, Lee K-B, Zucolotto V. A Detailed Investigation on the Interactions between Magnetic Nanoparticles and Cell Membrane Models. *Appl Mater interfaces.* 2013;5:13063–8.
44. Kumari A, Yadav SK, Yadav SC. Biodegradable polymeric nanoparticles based drug delivery systems. *Colloids Surfaces B Biointerfaces.* 2010;75:1–18.
45. Perez-Campaña C, Gomez-Vallejo V, Puigivila M, Martin A, Calvo-Fernandez T, Moya SE, et al. Biodistribution of Different Sized Nanoparticles Assessed by Positron Emission Tomography: A General Strategy for Direct Activation of Metal Oxide Particles. *ACS Nano.* 2013;7(4):3498–505.
46. Blundell HL. The Influence of Accurate Attenuation Correction on Quantitative Gamma Camera Imaging. [dissertation] Cardiff University; 2012.

## BIBLIOGRAPHY

---

47. Jenny Mansson. Preclinical PET/CT and SPECT/CT [Internet]. 2011 [cited 2016 Mar 8]. Available from:  
[http://www.med.lu.se/bioimaging\\_center/modalities/lbic\\_platforms/preclinical\\_nuclear\\_medicine\\_pet\\_spect\\_ct/basic\\_principles](http://www.med.lu.se/bioimaging_center/modalities/lbic_platforms/preclinical_nuclear_medicine_pet_spect_ct/basic_principles)
48. Hounsfield GN. Computerized transverse axial scanning (tomography): Part I. Description of system. *Br J Radiol.* 1973;46(552):1016–22.
49. Ntziachristos V, Leroy-Willig A, Tavitian B. Textbook of *in vivo* Imaging in Vertebrates. 2007. 1-373 p.
50. Lee SY, Jeon SI, Jung S, Chung IJ, Ahn C-H. Targeted multimodal imaging modalities. *Adv Drug Deliv Rev.* 2014;76:60–78.
51. Lee GY, Qian WP, Wang L, Wang YA, Staley CA, Satpathy M, et al. Theranostic Nanoparticles with Controlled Release of Gemcitabine for Targeted Therapy and MRI of Pancreatic Cancer. *ACS Nano.* 2013;7(3):2078–89.
52. Kilian K. <sup>68</sup>Ga-DOTA and analogs: Current status and future perspectives. *Reports Pract Oncol Radiother.* 2014;19:S13–21.
53. Xing Y, Zhao J, Conti PS, Chen K. Radiolabeled Nanoparticles for Multimodality Tumor Imaging. *Theranostics.* 2014;4(3):290–306.
54. Chen K, Conti PS. Target-specific delivery of peptide-based probes for PET imaging. *Adv Drug Deliv Rev.* 2010;62(11):1005–22.
55. Stockhofe K, Postema JM, Schieferstein H, Ross TL. Radiolabeling of Nanoparticles and Polymers for PET Imaging. *Pharmaceuticals.* 2014;7(4):392–418.
56. Gil Iceta L, Gomez-Vallejo V, Kozirowski J, Llop J. Isotopes in Nanoparticles, Fundamentals and Applications. In: Llop J, Gomez-Vallejo V, Gibson PN, editors. *Isotopes in Nanoparticles.* Singapore: Pan Stanford Publishing Pte. Ltd.; 2016. p. 429–53.
57. Garcia-Toraño E, Peyres Medina V, Romero E, Roteta M. Measurement of the half-life of <sup>68</sup>Ga. *Appl Radiat Isot.* 2014;87:122–5.
58. Engle JW, Lopez-Rodriguez V, Gaspar-Carcamo RE, Valdovinos HF, Valle-Gonzalez M, Trejo-Ballado F, et al. Very high specific activity <sup>66/68</sup>Ga from zinc targets for PET. *Appl Radiat Isot.* 2012;70(8):1792–6.

## BIBLIOGRAPHY

---

59. Hupf HB, Beaver JE. Cyclotron Production of Carrier-Free Gallium-67. *Int J Appl Radiat Isot.* 1970;21:75–9.
60. Van der Walt TN, Strelow FWE. Quantitative Separation of Gallium from Other Elements by Cation-Exchange Chromatography. *Anal Chem.* 1983;55(2):212–6.
61. Edwards CL, Hayes RL. Tumor scanning with  $^{67}\text{Ga}$  citrate. *J Nucl Med Off Publ Soc Nucl Med.* 1969;10(2):103–5.
62. Weiner RE. The Mechanism of  $^{67}\text{Ga}$  Localization in Malignant Disease. *Nucl Med Biol.* 1996;23(6):745–51.
63. Thakur ML. Gallium-67 and Indium-111 Radiopharmaceuticals. *Int J Appl Radiat Isot.* 1977;28:183–201.
64. Collery P, Keppler B, Madoulet C, Desoize B. Gallium in cancer treatment. *Crit Rev Oncol Hematol.* 2002;42(3):283–96.
65. Kumar V, Boddeti DK, Evans SG, Roesch F, Howman-Giles R. Potential use of  $^{68}\text{Ga}$ -apo-transferrin as a PET imaging agent for detecting *Staphylococcus aureus* infection. *Nucl Med Biol.* 2011;38(3):393–8.
66. Jalilian AR, Panahifar A, Mahmoudi M, Akhlaghi M, Simchi A. Preparation and biological evaluation of [ $^{67}\text{Ga}$ ]-labeled-superparamagnetic nanoparticles in normal rats. *Radiochim Acta.* 2009;97(1):51–6.
67. Shanehsazzadeh S, Oghabian MA, Lahooti A, Abdollahi M, Abolghasem Haeri S, Amanlou M, et al. Estimated background doses of [ $^{67}\text{Ga}$ ]-DTPA-USPIO in normal Balb/c mice as a potential therapeutic agent for liver and spleen cancers. *Nucl Med Commun.* 2013;34(9):915–25.
68. Cobaleda-Siles M, Gomez-Blanco N, Gonzalez M, Gomez-Vallejo V, Llop J, Mareque-Rivas JC. Intrinsically labelled magnetite- and quantum dot-filled micelles: improving specific activity of labelled Nanoparticles. *Intrinsically labelled magnetite- and quantum dot-filled micelles: improving specific activity of labelled Nanoparticles.* *Q. J. Nucl. Med. Mol. Im.* 58; 2014. p. 58–63.
69. Bartholoma MD, Louie AS, Valliant JF, Zubieta J. Technetium and Gallium Derived Radiopharmaceuticals: Comparing and Contrasting the Chemistry of Two Important Radiometals for the Molecular Imaging Era. *Chem Rev.* 2010;110(1):2903–20.

## BIBLIOGRAPHY

---

70. Velikyan I, Maecke H, Langstrom B. Convenient Preparation of  $^{68}\text{Ga}$ -Based PET-Radiopharmaceuticals at Room Temperature. *Bioconjug Chem*. 2008;19(2):569–73.
71. Prata MIM. Gallium-68: A New Trend in PET Radiopharmacy. *Curr Radiopharm*. 2012;5:1–8.
72. Velikyan I. Synthesis, Characterisation and Application of  $^{68}\text{Ga}$ -labelled Macromolecules. [dissertation] Uppsala Universitet; 2005.
73. Singh AN, Liu W, Hao G, Kumar A, Gupta A, Öz OK, et al. Multivalent Bifunctional Chelator Scaffolds for Gallium-68 Based Positron Emission Tomography Imaging Probe Design: Signal Amplification via Multivalency. *Bioconjug Chem*. 2011;22:1650–62.
74. Förster C, Schubert M, Pietzsch H-J, Steinbach J. Maleimido-Functionalized NOTA Derivatives as Bifunctional Chelators for Site-Specific Radiolabeling. *Molecules*. 2011;16(6):5228–40.
75. Chakravarty R, Chakraborty S, Dash A, Pillai MRA. Detailed evaluation on the effect of metal ion impurities on complexation of generator eluted  $^{68}\text{Ga}$  with different bifunctional chelators. *Nucl Med Biol*. 2013;40(2):197–205.
76. Meyer GJ, Mäcke H, Schuhmacher J, Knapp WH, Hofmann M.  $^{68}\text{Ga}$ -labelled DOTA-derivatised peptide ligands. *Eur J Nucl Med Mol Imaging*. 2004;31(8):1097–104.
77. Heppeler A, Froidevaux S, Mäcke HR, Jermann E, Be M, Powell P. Radiometal-Labelled Macrocyclic Chelator-Derivatised Somatostatin Analogue with Superb Tumour-Targeting Properties and Potential for Receptor-Mediated Internal Radiotherapy. 1999;(7):1974–81.
78. Bernstein LR. Mechanisms of Therapeutic Activity for Gallium. *Pharmacol Rev*. 1998;50(4):665–82.
79. Boschi S, Malizia C, Lodi F. Overview and Perspectives on Automation Strategies in  $^{68}\text{Ga}$  Radiopharmaceutical Preparations. *Theranostics, Gallium-68, and Other Radionuclides A Pathway to Personalized Diagnosis and Treatment*. 2013. p. 18–31.
80. Guerrero S, Herance JR, Rojas S, Mena JF, Gispert JD, Acosta GA, et al. Synthesis and *In Vivo* Evaluation of the Biodistribution of a  $^{18}\text{F}$ -Labeled Conjugate Gold-Nanoparticle-Peptide with Potential Biomedical Application. *Bioconjug Chem*.

## BIBLIOGRAPHY

---

- 2012;23:399–408.
81. Sharma R, Xu Y, Kim SW, Schueller MJ, Alexoff D, Smith SD, et al. Carbon-11 radiolabeling of iron-oxide nanoparticles for dual-modality PET/MR imaging. *Nanoscale*. 2013;5(16):7476–83.
82. Sarparanta M, Bimbo LM, Rytönen J, Mäkilä E, Laaksonen TJ, Laaksonen P, et al. Intravenous Delivery of Hydrophobin-Functionalized Porous Silicon Nanoparticles: Stability, Plasma Protein Adsorption and Biodistribution. *Pharmaceutics*. 2012;9:654–63.
83. Polyak A, Hajdu I, Bodnar M, Trencsenyi G, Pöstenyi Z, Haasz V, et al. <sup>99m</sup>Tc-labelled nanosystem as tumour imaging agent for SPECT and SPECT/CT modalities. *Int J Pharm*. 2013;449:10–7.
84. Sarparanta M, Mäkilä E, Heikkilä T, Salonen J, Kukk E, Lehto VP, et al. <sup>18</sup>F-Labeled Modified Porous Silicon Particles for Investigation of Drug Delivery Carrier Distribution *in Vivo* with Positron Emission Tomography. *Mol Pharm*. 2011;8(5):1799–806.
85. Wei I-C, Tsao N, Huang Y-H, Ho Y-S, Wu C-C, Yu D-F, et al. <sup>99m</sup>Tc-glycopeptide: Synthesis, biodistribution and imaging in breast tumor-bearing rodents. *Appl Radiat Isot*. 2008;66(3):320–31.
86. Fragogeorgi EA, Savina IN, Tsoதாக T, Efthimiadou E, Xanthopoulos S, Palamaris L, et al. Comparative *in vitro* stability and scintigraphic imaging for trafficking and tumor targeting of a directly and a novel <sup>99m</sup>Tc(CO)<sub>3</sub> labeled liposome. *Int J Pharm*. 2014;465(1):333–46.
87. Wunderlich G, Grüning T, Paulke B-R, Lieske A, Kotzerke J. <sup>99m</sup>Tc labelled model drug carriers - labeling, stability and organ distribution in rats. *Nucl Med Biol*. 2004;31(1):87–92.
88. Zhang Y, Sun Y, Xu X, Zhu H, Huang L, Zhang X, et al. Radiosynthesis and micro-SPECT imaging of <sup>99m</sup>Tc-dendrimer poly (amido)-amine folic acid conjugate. *Bioorg Med Chem Lett*. 2010;20(3):927–31.
89. Fatahian S, Shahbazi-Gahrouei D, Pouladian M, Yousefi MH, Amiri GR, Noori A. Biodistribution and toxicity assessment of radiolabeled and DMSA coated ferrite nanoparticles in mice. *J Radioanal Nucl Chem*. 2012;293:915–21.



## BIBLIOGRAPHY

---

90. Llop J, Jiang P, Marradi M, Gomez-Vallejo V, Echeverria M, Yu S, et al. Visualising dual radiolabelled poly (lactide-co-glycolide) nanoparticle degradation *in vivo* using energy-discriminant SPECT. *J Mater Chem B*. 2015;14–6.
91. FP7. Save Me [Internet]. [cited 2015 Oct 10]. Available from: fp7-saveme.com
92. Gazal S, Gellerman G, Glukhov E, Gilon C. Synthesis of novel protected Nalpha(omega-thioalkyl) amino acid building units and their incorporation in backbone cyclic disulfide and thioetheric bridged peptides. *J Pept Res*. 2001;58(6):527–39.
93. Rosenberger I, Strauss A, Dobiasch S, Weis C, Szanyi S, Gil-Iceta L, et al. Targeted diagnostic magnetic nanoparticles for medical imaging of pancreatic cancer. *J Control Release*. 2015;214:76–84.
94. Rosenberger I, Schmithals C, Vandooren J, Bianchessi S, Milani P, Locatelli E, et al. Physico-chemical and toxicological characterization of iron-containing albumin nanoparticles as platforms for medical imaging. *J Control Release*. 2014;194:130–7.
95. Aiertza MK, Odriozola I, Cabañero G, Grande H-J, Loinaz I. Single-chain polymer nanoparticles. *Cell Mol Life Sci*. 2012;69(3):337–46.
96. Little FE, Lagunas Solar MC. Cyclotron Production of  $^{67}\text{Ga}$ . Cross Sections and Thick-Target Yields for the  $^{67}\text{Zn}$  (p, n) and  $^{68}\text{Zn}$  (p, 2n) Reactions. *Int J Appl Radiat Isot*. 1983;34(3):631–7.
97. Vergara I, Medina LA, Alagon A.  $^{67}\text{Ga}$ -Chloride from  $^{67}\text{Ga}$ -Citrate for radiolabelling of biomolecules. 2006.
98. Llauro JG. Nuclear Medicine. *Clin Nucl Med*. 1991;16(12):953.
99. Diehl K-H, Hull R, Morton D, Pfister R, Rabemampianina Y, Smith D, et al. A Good Practice Guide to the Administration of Substances and Removal of Blood, Including Routes and Volumes. *J Appl Toxicol*. 2001;21(1):15–23.
100. Zuñiga JM, Orellana JM, Tur JA. Ciencia y tecnología del animal de laboratorio. Volumen II. [Science and technology of laboratory animals. Volume II] Universidad de Alcalá de Henares y SECAL; 2008.
101. Deer EL, Gonzalez-Hernandez J, Coursen JD, Shea JE, Ngatia J, Scaife CL, et al. Phenotype and Genotype of Pancreatic Cancer Cell Lines. *Pancreas*. 2010;39(4):425–

## BIBLIOGRAPHY

---

- 35.
- 102.** Kikutsuji T, Harada M, Tashiro S, Li S, Moritani M, Yamaoka T, et al. Expression of somatostatin receptor subtypes and growth inhibition in human exocrine pancreatic cancers. *J Hepatobiliary Pancreat Surg.* 2000;7(5):496–503.
- 103.** Fisher WE, Trisha AD, Li PM, Boros LG, Christopher EE, Schirmer WJ. Expression of Somatostatin Receptor Subtype 1-5 Genes in Human Pancreatic Cancer. *J Natl Cancer Inst.* 1998;90(4):322–4.
- 104.** Roda O, Ortiz-Zapater E, Martinez-Bosch N, Gutierrez-Gallego R, Vila-Perello M, Ampurdanes C, et al. Galectin-1 Is a Novel Functional Receptor for Tissue Plasminogen Activator in Pancreatic Cancer. *Gastroenterology.* 2009;136(4):1379–90.
- 105.** Altman DG, Bland JM. Comparing several groups using analysis of variance. *BMJ.* 1996;312(7044):1472–3.
- 106.** Lessa JA, Parrilha GL, Beraldo H. Gallium complexes as new promising metallodrug candidates. *Inorganica Chim Acta.* 2012;393:53–63.
- 107.** Aubert M, Crotte C, Bernard JP, Lombardo D, Sadoulet M-O, Mas E. Decrease of human pancreatic cancer cell tumorigenicity by alpha1,3galactosyltransferase gene transfer. *Int J Cancer.* 2003;107(6):910–8.
- 108.** Fukasawa M, Korc M. Vascular Endothelial Growth Factor-Trap Suppresses Tumorigenicity of Multiple Pancreatic Cancer Cell Lines. *Clin Cancer Res.* 2004;10:3327–32.
- 109.** Sheng Y, Liu C, Yuan Y, Tao X, Yang F, Shan X, et al. Long-circulating polymeric nanoparticles bearing a combinatorial coating of PEG and water-soluble chitosan. *Biomaterials.* 2009;30(12):2340–8.
- 110.** Owens DE, Peppas NA. Opsonization, biodistribution, and pharmacokinetics of polymeric nanoparticles. *Int J Pharm.* 2006;307:93–102.
- 111.** Ginj M, Zhang H, Eisenwiener KP, Wild D, Schulz S, Rink H, et al. New Pansomatostatin Ligands and Their Chelated Versions: Affinity Profile, Agonist Activity, Internalization, and Tumor Targeting. *Clin Cancer Res.* 2008;14(7):2019–27.
- 112.** Studlar K, Janousek I. The photometric determination of Zinc with xylenol orange. In:

## BIBLIOGRAPHY

---

- Ltd. PP, editor. *Talanta*. 1961. p. 203–8.
113. Gao X, Cui Y, Levenson RM, Chung LWK, Nie S. *In vivo* cancer targeting and imaging with semiconductor quantum dots. *Nat Biotechnol*. 2004;22(8):969–76.
114. Horcajada P, Chalati T, Serre C, Gillet B, Sebrie C, Baati T, et al. Porous metal-organic-framework nanoscale carriers as a potential platform for drug delivery and imaging. *Nat Mater*. Nature Publishing Group; 2009;9(2):172–8.
115. Veisheh O, Gunn JW, Zhang M. Design and fabrication of magnetic nanoparticles for targeted drug delivery and imaging. *Adv Drug Deliv Rev*. Elsevier B.V.; 2010;62(3):284–304.
116. Lewin M, Carlesso N, Tung C, Tang X, Cory D, Scadden DT, et al. Tat peptide-derivatized magnetic nanoparticles allow *in vivo* tracking and recovery of progenitor cells. *Nat Biotechnol*. 2000;18:410–4.
117. Wangler B, Quandt G, Iovkova L, Schirrmacher E, Wangler C, Boening G, et al. Kit-Like  $^{18}\text{F}$ -Labeling of Proteins: Synthesis of 4-(Di-tert-butyl[ $^{18}\text{F}$ ]fluorosilyl)benzenethiol ( $[\text{Si}^{18}\text{F}]\text{FA-SH}$ ) Labeled Rat Serum Albumin for Blood Pool Imaging with PET. *Bioconjug Chem*. 2009;20:317–21.
118. Goldenberg DM, DeLand F, Kis E, Bennett S, Primus FJ, van Nagell JR, et al. Use of radiolabeled antibodies to carcinoembryonic antigen for the detection and localization of diverse cancers by external photoscanning. *N Engl J Med*. 1978;298(25):1384–8.
119. Boyle AJ, Cao P-J, Hedley DW, Sidhu SS, Winnik MA, Reilly RM. MicroPET/CT imaging of patient-derived pancreatic cancer xenografts implanted subcutaneously or orthotopically in NOD-scid mice using  $^{64}\text{Cu}$ -NOTA-panitumumab  $\text{F}(\text{ab}')_2$  fragments. *Nucl Med Biol*. 2015;42(2):71–7.
120. Workman P, Aboagye EO, Balkwill F, Balmain A, Bruder G, Chaplin DJ, et al. Guidelines for the welfare and use of animals in cancer research. *Br J Cancer*. 2010;102(11):1555–77.
121. Varasteh Z, Mitran B, Rosenström U, Velikyan I, Rosestedt M, Lindeberg G, et al. The effect of macrocyclic chelators on the targeting properties of the  $^{68}\text{Ga}$ -labeled gastrin releasing peptide receptor. *Nucl Med Biol*. 2015; 42(5):446–454.

## BIBLIOGRAPHY

---

122. Banerjee SR, Pomper MG. Clinical applications of Gallium-68. *Appl Radiat Isot.* 2013;76:2–13.
123. Lascano AM, Perneger T, Vulliemoz S, Spinelli L, Garibotto V, Korff CM, et al. Yield of MRI, high-density electric source imaging (HD-ESI), SPECT and PET in epilepsy surgery candidates. *Clin Neurophysiol.* 2015;27(1):150–5.
124. Velikyan I. Prospective of <sup>68</sup>Ga-Radiopharmaceutical Development. *Theranostics.* 2014;4(1):47–80.
125. de Herder WW, Hofland LJ, van der Lely AJ, Lamberts SWJ. Somatostatin receptors in gastroenteropancreatic neuroendocrine tumours. *Endocr Relat Cancer.* 2003;10:451–8.
126. Soppimath KS, Aminabhavi TM, Kulkarni AR. Biodegradable polymeric nanoparticles as drug delivery devices. 2001;70:1–20.

## 9. FIGURES AND TABLES INDEX



FIGURES

	Page
1 Anatomical description and localization of the pancreas. Image modified from reference (9).....	8
2 Schematic representation of passive targeting penetration for NPs access to tumour cells. Image modified from reference (32).....	17
3 SST amino acid's sequence and structure. MW: 1638 g/mol.....	19
4 Octreotide amino acid's sequence and structure. MW: 1019 g/mol.....	20
5 Principle of SPECT tomographic acquisition. In the representation, $g(s,\theta)$ is the number of gamma photons detected at any location (s) along the detector crystals at a given angle ( $\theta$ ). Image adapted from reference (46).....	25
6 Schematic representation of the detection of photons using SPECT (a) and PET (b) scanners. Adapted from reference (47).....	27
7 Schematic representation of the labelling strategy by means of bifunctional chelators.....	33
8 Examples of the ligands DOTA (A), NOTA (B) and NODAGA (C) derivatives. Adapted from reference (52) And $\text{NH}_2$ -DOTA-GA (D) and $\text{NH}_2$ -NODA-GA (E) chelators.....	34
9 $\text{PTR}_{3207-86}$ -GABA-FITC amino acid's sequence and structure. MW: 1753 g/mol. Reprinted with permission of TAU partner.....	59
10 tPA-1 targeting moiety with a Serine- $\gamma$ -D-lactose peptide sequence and FITC fluorescent agent. Reprinted with permission of UKH partner.....	60
11 Synthetic process of SCPNs, in which X stands for any BFCA or targeting or penetrating agent. Reprinted with permission of CID partner.....	65
12 Flowchart of the conversion procedure of $^{67}\text{Ga}$ citrate into $^{67}\text{Ga}$ chloride.....	69
13 Hot cell installed in the Molecular Imaging Unit of CIC biomaGUNE.....	70
14 Flowchart of the experimental protocol for the study of tumour growth profile until imaging assays were conducted. Red arrows indicate animal monitoring procedures; animal weight and tumour volume calculations.....	77
15 SPECT-CT preclinical imaging system from GE installed in CIC biomaGUNE (A) and animal positioned on the SPECT-CT gantry (B).....	78
16 MRI 11.7 Tesla scanner from Bruker installed in CIC biomaGUNE.....	81
17 Graphical representation of the fractionated elution of $^{67}\text{Ga}$ after extraction of the activity retained on the Sep-Pak <sup>®</sup> with $\text{HCl}_{30\%}$ .....	87
18 Panc-1 SC tumours growth curve represented in volume ( $\text{mm}^3$ ) throughout	

FIGURES AND TABLES INDEX

---

	time expressed in days after inoculation of 0.5 million (rhombus), 1 million (triangle) and 2 million (square) tumour cells. Results are expressed as mean $\pm$ SD, n=10 per group.....	97
<b>19</b>	Photograph of a representative immunosuppressed mouse with a pancreatic SC tumour in its left flank 8 weeks after injection of 2 million Panc-1 cells.....	98
<b>20</b>	Panc-1 SC tumours growth curve represented in volume (mm <sup>3</sup> ) throughout time expressed in days after inoculation of 2 million tumour cells. Dots, mean; lines, SD; n=50.....	99
<b>21</b>	Average T/M ratios (mean $\pm$ SD, n=2) for NPs BIU-01, BIU-02 and BIU-03 at 3, 24 and 48 hours after intravenous administration of labelled NPs (15.5 $\pm$ 4.6 MBq, 8.2 $\pm$ 1.8 MBq and 8.9 $\pm$ 0.9 MBq, respectively).....	102
<b>22</b>	SPECT-CT 3D images of <sup>67</sup> Ga-labelled BIU-01 NPs at t= 48 hours after intravenous administration. Axial 2 dimensional (2D) slices show: tumour located in the upper dorsal left part of the animal (top), a transversal section of the liver (middle) and a slice in the inguinal region showing the bladder (bottom).....	103
<b>23</b>	SPECT-CT 3D images of <sup>67</sup> Ga-labelled BIU-02 NPs at t= 48 hours after intravenous administration. Axial 2D slices show: tumour located in the upper dorsal left part of the animal (top), a transversal section of the liver (middle) and a slice in the inguinal region showing the bladder (bottom).....	104
<b>24</b>	SPECT-CT 3D images of <sup>67</sup> Ga-labelled BIU-03 NPs at t= 48 hours after intravenous administration. Axial 2D slices show: tumour located in the upper dorsal left part of the animal (top), a transversal section of the liver (middle) and a slice in the inguinal region showing the bladder (bottom).....	105
<b>25</b>	Average T/M ratios (mean $\pm$ SD, n=2) for NPs GU-01, GU-02 and GU-03 at 3, 24 and 48 hours after intravenous administration of labelled NPs (6.7 $\pm$ 1.0 MBq, 6.3 $\pm$ 1.5 MBq and 10.1 $\pm$ 5.9 MBq, respectively).....	106
<b>26</b>	SPECT-CT 3D images of <sup>67</sup> Ga-labelled GU-01 NPs at t= 48 hours after intravenous administration. Axial 2D slices show: tumour located in the upper dorsal left part of the animal (top), a transversal section of the liver (middle) and a cut in the inguinal region showing the bladder (bottom).....	107
<b>27</b>	SPECT-CT 3D images of <sup>67</sup> Ga-labelled GU-02 NPs at t= 48 hours after intravenous administration. Axial 2D slices show: tumour located in the upper dorsal left part of the animal (top), a transversal section of the liver (middle) and a cut in the inguinal region showing the bladder (bottom).....	108
<b>28</b>	SPECT-CT 3D images of <sup>67</sup> Ga-labelled GU-03 NPs at t= 48 hours after intravenous administration. Axial 2D slices show: tumour located in the upper dorsal left part of the animal (top), a transversal section of the liver	



FIGURES AND TABLES INDEX

---

	(middle) and a cut in the inguinal region showing the bladder (bottom).....	109
<b>29</b>	Average T/M ratios (mean $\pm$ SD, n=2) for NPs UNIBO-01 and UNIBO-02 at 3, 24 and 48 hours after intravenous administration of labelled NPs ( $30.41 \pm 1.66$ MBq and $19.50 \pm 14.50$ MBq doses respectively).....	110
<b>30</b>	SPECT-CT 3D images of $^{67}\text{Ga}$ -labelled UNIBO-01 NPs at t= 48 hours after intravenous administration. Axial 2D slices show: tumour located in the upper dorsal left part of the animal (top), a transversal section of the liver (middle) and a cut in the inguinal region showing the bladder (bottom).....	111
<b>31</b>	SPECT-CT 3D images of $^{67}\text{Ga}$ -labelled and UNIBO-02 NPs at t= 48 hours after intravenous administration. Axial 2D slices show: tumour located in the upper dorsal left part of the animal (top), a transversal section of the liver (middle) and a cut in the inguinal region showing the bladder (bottom).....	112
<b>32</b>	Average T/M ratios (mean $\pm$ SD, n=2) for NPs CIC-01 and CIC-02 at 3, 24 and 48 hours after intravenous administration of labelled NPs ( $4.5 \pm 1.9$ MBq and $2.0 \pm 1.1$ MBq, respectively).....	113
<b>33</b>	SPECT-CT 3D images of $^{67}\text{Ga}$ -labelled CID-01 NPs at t= 48 hours after intravenous administration. Axial 2D slices show: tumour located in the upper dorsal left part of the animal (top), a transversal section of the liver (middle) and a cut in the inguinal region showing the bladder (bottom).....	114
<b>34</b>	SPECT-CT 3D images of $^{67}\text{Ga}$ -labelled CID-02 NPs at t= 48 hours after intravenous administration. Axial 2D slices show: tumour located in the upper dorsal left part of the animal (top), a transversal section of the liver (middle) and a cut in the inguinal region showing the bladder (bottom).....	115
<b>35</b>	SPECT-CT 3D images of an animal injected with CID-02 NPs 24 hours (A) and 48 hours (B) after administration of the radioactive doses.....	116
<b>36</b>	MRI T2-w images normalized against spinal-cord of the Panc-1 tumour bearing mice for BIU-01 (A), BIU-02 (B) and BIU-03 (C) particles at 0 h (before injection), and 2 and 24 h post injection. Scale reflects signal intensity (s.i.=100) in arbitrary units.....	118
<b>37</b>	MRI T2-w images normalized against spinal-cord of the Panc-1 tumour bearing mice for GU-01 (A), GU-02 (B) and GU-03 (C) particles at t=0 h (before injection) and t= 2 and 24 h post injection. Scale reflects signal intensity (s.i.=100) in arbitrary units.....	119
<b>38</b>	Schematic representation of the rationale behind the use of PEG-MMP-substrate-PEG decorations. The NPs present in the capillaries (A) cross the endothelial cells of the blood vessels and are recognized by MMPs, (B) which cleave the outer PEG chain, resulting in a reduction in NP size (C). Thanks to the presence of the targeting moieties, the NPs interact with tumour cell receptors (D) and are internalized (E).....	127

FIGURES AND TABLES INDEX

---

39	Panc-1 SC tumours growth curve expressed in volume (mm <sup>3</sup> ) after inoculation of 2 million Panc-1 cells. Dots, mean; lines, SD; n=50.....	143
40	Average T/M ratios for <sup>67</sup> Ga-PNPs in Panc-1 xenografted CD-1 Foxn1 nu/nu mice at 3, 24 and 48 h PI.....	145
41	Average T/M ratios for <sup>67</sup> Ga-PNPs in Panc-1 xenografted CD-1 Foxn1 nu/nu mice at 3 h PI.....	146
42	Average T/M ratios for <sup>67</sup> Ga-PNPs in Panc-1 xenografted CD-1 Foxn1 nu/nu mice at 24 h PI.....	147
43	Average T/M ratios for <sup>67</sup> Ga-PNPs in Panc-1 xenografted CD-1 Foxn1 nu/nu mice at 48 h pi; *, P ≤ 0.05.....	148
44	SPECT-CT 3D images of <sup>67</sup> Ga-labelled CID-04 at t= 48 hours after intravenous administration. Axial 2D slices show: tumours located in the upper dorsal left part of the animal (top), a transversal section of the liver (middle) and a cut in the inguinal region showing the bladder (bottom).....	149
45	SPECT-CT 3D images of <sup>67</sup> Ga-labelled CID-05 at t= 48 hours after intravenous administration. Axial 2D slices show: tumours located in the upper dorsal left part of the animal (top), a transversal section of the liver (middle) and a cut in the inguinal region showing the bladder (bottom).....	150
46	SPECT-CT 3D images of <sup>67</sup> Ga-labelled CID-06 at t= 48 hours after intravenous administration. Axial 2D slices show: tumours located in the upper dorsal left part of the animal (top), a transversal section of the liver (middle) and a cut in the inguinal region showing the bladder (bottom).....	151
47	SPECT-CT 3D images of <sup>67</sup> Ga-labelled CID-07 at t= 48 hours after intravenous administration. Axial 2D slices show: tumours located in the upper dorsal left part of the animal (top), a transversal section of the liver (middle) and a cut in the inguinal region showing the bladder (bottom).....	152
48	SPECT-CT 3D images of <sup>67</sup> Ga-labelled CID-08 at t= 48 hours after intravenous administration. Axial 2D slices show: tumours located in the upper dorsal left part of the animal (top), a transversal section of the liver (middle) and a cut in the inguinal region showing the bladder (bottom).....	153
49	SPECT-CT 3D images of <sup>67</sup> Ga-labelled CID-09 at t= 48 hours after intravenous administration. Axial 2D slices show: tumours located in the upper dorsal left part of the animal (top), a transversal section of the liver (middle) and a cut in the inguinal region showing the bladder (bottom).....	154
50	SPECT-CT 3D images of <sup>67</sup> Ga-labelled CID-10 at t= 48 hours after intravenous administration. Axial 2D slices show: tumours located in the upper dorsal left part of the animal (top), a transversal section of the liver (middle) and a cut in the inguinal region showing the bladder (bottom).....	155
51	Average T/M ratios for <sup>67</sup> Ga-PNPs in Panc-1 xenografted CD-1 Foxn1 nu/nu	

## FIGURES AND TABLES INDEX

---

	mice at different time points with GU-04 and GU-05 particles.....	157
<b>52</b>	SPECT-CT 3D images of <sup>67</sup> Ga-labelled GU-04 at t= 48 hours after intravenous administration. Axial 2D slices show: tumours located in the upper dorsal left part of the animal (top), a transversal section of the liver (middle) and a cut in the inguinal region showing the bladder (bottom).....	158
<b>53</b>	SPECT-CT 3D images of <sup>67</sup> Ga-labelled GU-05 at t= 48 hours after intravenous administration. Axial 2D slices show: tumours located in the upper dorsal left part of the animal (top), a transversal section of the liver (middle) and a cut in the inguinal region showing the bladder (bottom).....	159




TABLES

	Page
1 Pancreatic cancer exocrine tumour types.....	11
2 Pancreatic cancer endocrine tumour types.....	13
3 Physical decay characteristics of conventional positron emitting (PET) and gamma emitting (SPECT) radionuclides and most common production routes.....	31
4 Composition, functionalization, size, polydispersity index (PDI) and zeta-potential of the NPs.....	66
5 List of NPs tested by MRI 11.7 T in the animal model bearing Panc-1 SC tumours (n=2/sample) and injected doses depending upon NP's iron content.....	82
6 Optimized radiolabelling conditions and radiochemical conversion (RCC) values of <sup>67</sup> Ga labelled NPs for <i>in vivo</i> imaging studies in Panc-1 SC tumour model nude mice. All results are expressed as mean ± SD (n=4).....	90
7 Radiochemical integrity results of radiolabelled nanoparticles, expressed as percentage of unmodified NPs; <sup>1</sup> after incubation with a solution containing DOTA at a final concentration of 32 µM; and <sup>2</sup> after incubation in saline solution. Incubation temperature was 37 °C in all cases.....	94
8 Average injected dose of each <sup>67</sup> Ga radiolabelled compound for <i>in vivo</i> SPECT-CT animal experiments (n=2).....	96
9 Composition, functionalization, size, and PDI values of the NPs.....	131
10 Composition, functionalization, size, PDI and zeta-potential values of the NPs.....	132
11 Averaged RCC values expressed in percentage.....	138
12 Stability of radiolabelled NPs, expressed as percentage of unmodified NPs, after incubation with a solution containing NOTA at a final concentration of 32 µM; incubation temperature: 37 °C.....	140
13 Stability of radiolabelled NPs, expressed as percentage of unmodified NPs, after incubation with saline solution at 37 °C.....	141
14 Average injected doses for the different <sup>67</sup> Ga-radiolabelled NPs for the <i>in vivo</i> SPECT-CT animal experiments (n=5).....	142


## 10. ANNEX: ORIGINAL PUBLICATIONS





### ARTICLES

-  Locatelli E, **Gil L**, Israel LL, Passoni L, Naddaka M, Pucci A, et al. Biocompatible nanocomposite for PET/MRI hybrid imaging. *Int J Nanomedicine*. 2012;7:6021–33.
-  Locatelli E, Bost W, Fournelle M, Llop J, **Gil L**, Arena F, et al. Targeted polymeric nanoparticles containing gold nanorods: A therapeutic approach against glioblastoma. *J Nanoparticle Res. Kluwer Academic Publishers*; 2014;16(3).
-  Rosenberger I, Strauss A, Dobiasch S, Weis C, Szanyi S, **Gil-Iceta L**, et al. Targeted diagnostic magnetic nanoparticles for medical imaging of pancreatic cancer. *J Control Release*. 2015;214:76–84.
-  Ana B. Benito, Miren K. Aiertza, Marco Marradi, **Larraitz Gil-Iceta**, Talia Shekther Zahavi, Boguslaw Szczupak, et al. Functional Single Chain Polymeric Nanoparticles: Targeting and Imaging Pancreatic Tumors *in vivo*. *J Biomaterials*. Submitted



### BOOK CHAPTERS

-  Jordi Llop Roig, Vanessa Gómez-Vallejo, Peter Neil Gibson. Isotopes in Nanoparticles, Fundamentals and Applications. Edited by Pan Stanford Publishing Pte. Ltd. 2016. Contribution to the book: Chapter 16. Radiochemical Stability Studies of Radiolabelled Nanoparticles. **Larraitz Gil Iceta**, Vanessa Gómez-Vallejo, Jacek M. Kozirowski, and Jordi Llop.

## ORAL PRESENTATIONS

-  V. Gómez-Vallejo, **L. Gil Iceta**, M. Errasti López, M. González Esparza, A. Lekuona Fernández y J. Llop Roig. Producción semiautomática de  $^{89}\text{Zr}$ . Rev Esp Med Nucl Imagen Mol. 2015; 34 (Supl 1): 144. Presented at SEMNIM 2015, Zaragoza, Spain.
-  Benito AB, Aiertza MK, Marradi M, **Gil L**, Alonso Guerrero E, Jiménez-González M, Reese T, Scanziani E, Passoni L, Orenstein A, Oron-Herman M, Shekther Zahavi T, Gazit E, Cabañero G, Grande HJ, Gómez-Vallejo V, Llop J and Loinaz I (2016). Functional single chain polymer nanoparticles: Targeting and imaging pancreatic tumors *in vivo*. *Front. Bioeng. Biotechnol.* doi: 10.3389/conf.FBIOE.2016.01.00979. Presented at 10<sup>th</sup> WBC, Montréal, Canada.

## POSTERS

-  Strauss A., Jiménez M., Szczupak B., Plaza S., Weis C., Llop J., Gómez-Vallejo V., **Gil L.**, Knoll P., Mirzaei S., Israel L., Lellouche J.-P., Felix K. Dobiasch S., Wemer J., Rosenberger I., Kreuter J., Kauczor H.-U., Grenacher L. “Homing-analysis of different iron-loaded nanoparticles targeted against PaCa using 11.7T MRI and SPECT-CT”. WMIC 2014, Seoul, Korea, September 17-20, 2014.
-  A. Benito, M. K. Aiertza, M. Marradi, **L. Gil**, E. Alonso Guerrero, M. Jiménez, T. Reese, E. Scanziani, L. Passoni, A. Orenstein, M. Oron-Herman, G. Cabañero, H.-J. Grande, V. Gomez, J. Llop, I. Loinaz. “Functional Single Chain Polymeric Nanoparticles: Targeting and



Imaging Pancreatic Tumors *in vivo*". CLINAM 2015, Basel, Switzerland, June 29 – July 1, 2015. **POSTER AWARD WINNER**



J. Llop, P. Jiang, M. Marradi, V. Gómez-Vallejo, M. Echeverría, L. Gil-Iceta, S. Yu, M. Puigivila, Z. Baz, B. Szczupak, C. Pérez-Campaña, Z. Mao, C. Gao, S. E. Moya. "A Novel Approach for Visualizing Dual Radiolabeled Poly (lactide-co-glycolide) Nanoparticles Degradation *in vivo* by means of energy-discriminant SPECT". ISAB meeting 2015, San Sebastián, Spain, September 17-18, 2015.



Larraitz Gil Iceta, Vanessa Gómez-Vallejo, María Jiménez-González, Ana Benito, Talia Shekther Zahavi, Ehud Gazit, Iraida Loinaz, Torsten Reese, Jordi Llop. "Influence of Different Targeting Moieties on SCPNs by SPECT/CT Imaging for Triggering Pancreatic Cancer". Biomapp 2015, San Sebastián, Spain, October 19-20, 2015.



Larraitz Gil Iceta, María Jiménez-González, Boguslaw Szczupak, Vanessa Gomez-Vallejo, Torsten Reese, Jordi Llop. "<sup>18</sup>F-FDG biodistribution differences depending upon different anesthesia conditions in tumor bearing mice". Molecular Imaging Workshop, November 10-12, 2015.



Larraitz Gil Iceta, María Jiménez-González, Talia Shekther Zahavi, Vanessa Gómez-Vallejo, Ehud Gazit, Torsten Reese, Jordi Llop. "Tumor targeting efficiency studies of radiolabeled PTR peptides for pancreatic cancer". Molecular Imaging Workshop, November 10-12, 2015. **POSTER AWARD WINNER**



# Biocompatible nanocomposite for PET/MRI hybrid imaging

Erica Locatelli<sup>1</sup>  
Larraitz Gil<sup>2</sup>  
Liron Limor Israel<sup>3</sup>  
Lorena Passoni<sup>4,5</sup>  
Maria Naddaka<sup>1</sup>  
Andrea Pucci<sup>1</sup>  
Torsten Reese<sup>6</sup>  
Vanessa Gomez-Vallejo<sup>2</sup>  
Paolo Milani<sup>5,7</sup>  
Michela Matteoli<sup>4,8</sup>  
Jordi Llop<sup>2</sup>  
Jean Paul Lellouche<sup>3</sup>  
Mauro Comes Franchini<sup>1</sup>

<sup>1</sup>Department of Industrial Chemistry "Toso Montanari", University of Bologna, Italy; <sup>2</sup>Radiochemistry Department, Molecular Imaging Unit, CIC biomaGUNE, San Sebastián, Guipúzcoa, Spain; <sup>3</sup>Department of Chemistry, Nanomaterials Research Centre, Institute of Nanotechnology and Advanced Materials, Bar-Ilan University, Ramat-Gan, Israel; <sup>4</sup>Department of Medical Biotechnology and Translational Medicine, University of Milano, Italy; <sup>5</sup>Fondazione Filarete, Milano, Italy; <sup>6</sup>Imaging Department, Molecular Imaging Unit, CIC biomaGUNE, San Sebastián, Guipúzcoa, Spain; <sup>7</sup>CIMAINA and Department of Physics, University of Milano, Italy; <sup>8</sup>Humanitas Clinical and Research Center, Rozzano, Italy

Correspondence: Mauro Comes Franchini  
Department of Organic Chemistry  
"A Mangini," Faculty of Industrial  
Chemistry  
Tel +39 05 1209 3626  
Fax +39 05 1209 3626  
Email mauro.comesfranchini@unibo.it

**Abstract:** A novel nanocarrier system was designed and developed with key components uniquely structured at the nanoscale for early cancer diagnosis and treatment. In order to perform magnetic resonance imaging, hydrophilic superparamagnetic maghemite nanoparticles (NPs) were synthesized and coated with a lipophilic organic ligand. Next, they were entrapped into polymeric NPs made of biodegradable poly(lactic-co-glycolic acid) linked to polyethylene glycol. In addition, resulting NPs have been conjugated on their surface with a 2,2'-(7-(4-((2-aminoethyl)amino)-1-carboxy-4-oxobutyl)-1,4,7-triazonane-1,4-diyl)diacetic acid ligand for subsequent <sup>68</sup>Ga incorporation. A cell-based cytotoxicity assay has been employed to verify the in vitro cell viability of human pancreatic cancer cells exposed to this nanosystem. Finally, in vivo positron emission tomography-computerized tomography biodistribution studies in healthy animals were performed.

**Keywords:** maghemite nanoparticles, organic coating, polymeric nanoparticles, magnetic resonance imaging, radiolabeling, positron emission tomography

## Introduction

Despite impressive progress in basic and clinical medicine, cancer still ranks as one of the leading causes of mortality in Europe and in the United States.<sup>1,2</sup> Consequently, the development of imaging agents and diagnostic methods for detecting cancer at an early presymptomatic stage as well as new therapeutic agents able to overcome the problems commonly associated with traditional treatments is urgently required.

Cancer diagnosis utilizes anatomical or molecular imaging methods such as magnetic resonance imaging (MRI), positron emission tomography (PET), single photon emission computerized tomography (CT), ultrasound imaging, optical imaging. Each of these modalities has its own limitations in terms of spatial resolution, sensitivity, and depth of signal penetration that might be overcome by the combination of two or more such modalities.<sup>3</sup> Therefore, dual or multimodal imaging are currently being explored to enhance the quality and specificity of imaging methods in order to achieve proper visualization of organs or to better localize the accumulation of a diagnostic or therapeutic agent. Concomitantly, the development of multimodal imaging probes has attracted much attention during the last years.

Recently, nanotechnology has emerged as an excellent tool for the generation of nanoparticles (NPs) for diagnostic (imaging) or therapeutic purposes. Among all NPs, inorganic ones have attracted great interest, given their intrinsic physical properties and compatible size. The best example can be found in magnetic NPs (MNP) which have been used as contrast agents for MRI for more than 20 years.<sup>4</sup> However, the pursuit of

multimodal imaging agents requires the development of organic ligands that are able to make the MNPs lipophilic (coated with an organic molecule), and that entrap them into a polymeric matrix acting as a targetable water soluble nanocarrier. In ideal planning, this nanocarrier would be further functionalized with an appropriate labeling agent (eg, a positron emitter), to allow multi-modal *in vivo* imaging. In order to achieve efficient distributions in the targeted tumor lesions for early cancer diagnosis and treatment, the colloidal nanocarriers are required to be highly monodisperse and smaller than 200 nm.<sup>5</sup>

Here we describe the preparation and characterization of a novel, versatile, and biocompatible hybrid nanocarrier for dual PET/MRI imaging. This nanocarrier contains a superparamagnetic maghemite core consisting of crystalline, as well as hydrophilic and strongly positively charged ceric ammonium nitrate (CAN)-stabilized maghemite NPs for MRI contrast,<sup>6</sup> which were encapsulated in the well-known poly(D,L-lactide-co-glycolide)-block-poly(ethylene glycol) copolymer (PLGA-b-PEG-COOH). Polyethyleneglycol (PEG)-based polymeric nanoparticles (PNPs), owing to their stealth character,<sup>7</sup> are widely used delivery systems for *in vivo* applications. On the other hand, the PLGA-b-PEG-COOH copolymer self-assembles to form targetable PNPs consisting of a hydrophobic poly(D,L-lactide-co-glycolide) (PLGA) core and a hydrophilic PEG corona-like shell. Interestingly, the presence of active sites (COOH) on the surface allows surface modification with 2,2'-(7-(4-((2-aminoethyl)amino)-1-carboxy-4-oxobutyl)-1,4,7-triazonane-1,4-diyl)diacetic acid (NODA) to chelate <sup>68</sup>Ga for PET imaging (see Figure 1 for the schematic representation of the fabrication of this nanocarrier). Since the resulting composite presented a high T<sub>2</sub> relaxivity, such a system should be suitable as an MRI contrast agent. Furthermore, the <sup>68</sup>Ga-radiolabeled NPs proved to be stable and allowed *in vivo* biodistribution studies in healthy animals using PET-CT. Further attachment

of functional groups that can act as targeting moieties or therapeutic agents could be pursued in the near future using the functional groups present on the NP surface, leading to multimodal PET-MRI diagnostic agents. The combination of both PET and MRI imaging capabilities should provide images with high anatomical resolution of MRI at the sensitivity of PET (10<sup>-9</sup> to 10<sup>-12</sup> M).<sup>8</sup>

Despite the suitability of the nanoplatforms reported here for the preparation of a wide range of diagnostic multimodal agents, one first application is expected in the field of pancreatic cancer diagnosis in the frame of the SaveMe project (EU-FP7 project number CP-IP 263307-2). Thus, a preliminary investigation (*in vitro* toxicity tests) of the developed nanosystem has been performed.

An application to pancreatic ductal adenocarcinoma (PDAC) has been preliminarily investigated. PDAC is one of the most aggressive malignancies with an overall 5-year survival rate of only 3%–5% and a median survival time after diagnosis of 6 months.<sup>9</sup> This highly lethal disease is usually diagnosed in an advanced stage when there are few or no effective therapies available.<sup>10</sup>

## Materials and methods

All chemicals were purchased from Sigma-Aldrich (St Louis, MO, USA) and used as received. Poly(D,L-lactide-co-glycolide) (50/50) with carboxylic acid end group (PLGA-COOH, pharmaceutical grade, inherent viscosity 0.12 dL/g, molecular weight (MW) ~7 kDa) was purchased from Lakeshore Biomaterials (Lakeshore Biomaterials, Inc, Birmingham, AL, USA). PEG with amino and carboxylic acid end groups (NH<sub>2</sub>-PEG-COOH, >95%, MW ~3 kDa) was purchased from Rapp Polymere GmbH (Tübingen, Germany). All aqueous solutions were prepared with deionized water obtained using an ultrafiltration system (Milli-Q, Millipore Corporation, Billerica, MA, USA) with a mea-

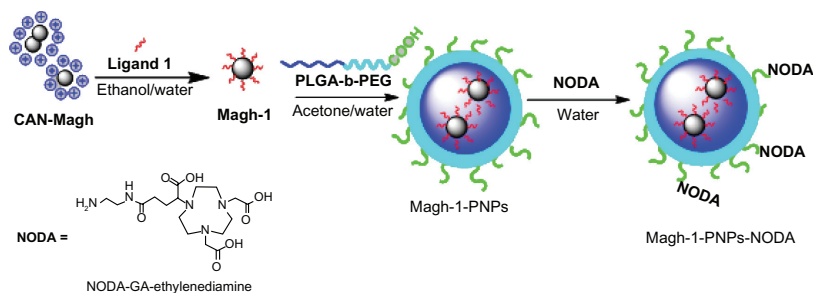


**Figure 1** Schematic representation of the synthesis of Magh-1-PNPs-NODA.

**Abbreviations:** CAN, ceric ammonium nitrate; PNPs, polyethyleneglycol-based nanoparticles; NODA, 2,2'-(7-(4-((2-aminoethyl)amino)-1-carboxy-4-oxobutyl)-1,4,7-triazonane-1,4-diyl)diacetic acid; PLGA-b-PEG, poly(D,L-lactide-co-glycolide)-block-poly(ethylene glycol).

sured resistivity above 18 M $\Omega$ /cm (referred in the text as double distilled [dd] water). Tetrahydrofuran was distilled from sodium/benzophenone just prior to use and stored under Ar. CH<sub>2</sub>Cl<sub>2</sub> and CHCl<sub>3</sub> were passed through basic alumina prior to use. Transmission electron microscopy (TEM) was conducted on a JEOL JEM 2010 at 200 keV (JEOL, Tokyo, Japan). Samples for TEM analyses were prepared by spreading a small drop of the NP dispersion on amorphous carbon-coated copper grids (Formvar carbon 400 mesh grids) followed by air-drying. Inductively coupled plasma (ICP) was performed on diluted acidic aqueous solutions using a Jobin Yvon Ultima 2 device (HORIBA, Ltd, Fukuoka, Japan). <sup>1</sup>H-NMR (hydrogen-1 nuclear magnetic resonance) and <sup>13</sup>C-NMR (carbon nuclear magnetic resonance) spectra were recorded using CDCl<sub>3</sub> or dimethyl sulfoxide solutions at 300, 400, and 600 MHz for <sup>1</sup>H, and 75.46, 100.6, and 150.92 MHz for <sup>13</sup>C. Chemical shifts ( $\delta$ ) are reported in ppm relative to CHCl<sub>3</sub> ( $\delta = 7.26$  for <sup>1</sup>H and  $\delta = 77.0$  for <sup>13</sup>C). Fourier transform infrared spectra were recorded on a PerkinElmer Spectrum 2000 (PerkinElmer, Waltham, MA, USA). Dynamic light scattering (DLS) measurements were performed on a Malvern Zetasizer nano-S working with a 532 nm laser beam (Malvern Instruments Ltd, Malvern, UK). Moreover,  $\zeta$  potential measurements were conducted in DTS1060C-clear disposable zeta cells at 25°C. SpectraAA 100 Varian (Palo Alto, CA, USA) was used for atomic absorption spectroscopy analyses. Thermogravimetric analyses were carried out on a TA Instruments 1GA Q500 (TA Instruments, New Castle, DE, USA) apparatus (nitrogen flow, isothermal temperature accuracy of 0.1°C for a weighting precision of 0.1  $\mu$ g).

Synthesis of ethyl 12-((3,4-dihydroxyphenethyl)amino)-12-oxododecanoate 1 was conducted as reported in the steps 2-4 of the supplementary material (see also Figures S2-S4).

## Synthesis of Magh-I

CAN-maghemite NPs were synthesized according to a known procedure that was recently developed in our laboratory with slight modifications, using preformed magnetite NPs as starting nanoscale material (see supporting information for details concerning the all synthesis pathways).<sup>6</sup>

Accordingly, the original CAN-Magh solution was diluted with water and added to an ethanolic solution of ethyl 12-((3,4-dihydroxyphenethyl)amino)-12-oxododecanoate (EDAO) 1. The mixture was sonicated in an ultrasound bath for 1 hour, and it was left to react overnight at room temperature under mechanical stirring. Afterward, the solution was decanted magnetically.

## Synthesis of Magh-I-PNPs

A total of 560 mg of PLGA-b-PEG-COOH (10 kDa) was added to 56 mL of an acetone solution of Magh-I. The organic phase was mixed to 560 mL of ultrapure water under vigorous stirring, maintaining the water/organic ratio of 10/1 with constant removal of the solution. The mixture was kept for 30 minutes under vigorous stirring. The residual organic solvent was evaporated under reduced pressure. The solution was concentrated to a volume of 100 mL using a tangential flow filter (Pellicon XL filter device, Biomax membrane with 500.000 NMWL; Millipore Corporation) following by filtration using a syringe filters Sterivex<sup>TM</sup>-GP of polyethersulfone (0.22  $\mu$ m, Millipore Corporation).

## Synthesis of Magh-I-PNPs-NODA

The linkage of NODA on the surface of the particle was carried out through a classic peptide formation. In particular, Magh-I-PNP water solutions were stirred for 2 hours in the presence of 1-ethyl-3-(3-dimethylaminopropyl) carbodiimide. Then, NODA-GA-ethylenediamine were added, and the reaction mixture was kept under stirring for an additional 2 hours. The particles were purified with a centrifugal filter device.

## Nuclear magnetic resonance (NMR) relaxivity

Relaxivity measurements were performed on a Bruker Minispec TD-NMR system (Bruker Optik GmbH, Ettlingen, Germany) at 37°C operating at 1.5 Tesla and 60 MHz proton resonance frequency. The longitudinal relaxation times ( $T_1$ ) and transverse relaxation times ( $T_2$ ) were determined at the following concentrations for each nanocomposite: 0.01, 0.03, 0.1, 0.3, 1, and 3 mM Fe in 50% D<sub>2</sub>O/H<sub>2</sub>O. A linear regression of the concentration versus  $T_1$  relaxation time or  $T_2$  relaxation time yielded  $R_1$  and  $R_2$  values [ $\text{mmol}^{-1} \text{s}^{-1}$ ], as summarized in Table 1.

**Table 1** Relaxivity values obtained for Magh, Magh-I-PNPs, and Magh-I-PNPs-NODA

Compound	$R_1$ [ $\text{mmol}^{-1} \text{sec}^{-1}$ ]	$R_2$ [ $\text{mmol}^{-1} \text{sec}^{-1}$ ]	
CAN-Magh	0.2	72	H <sub>2</sub> O/D <sub>2</sub> O
Magh-I-PNPs	0.9	134	H <sub>2</sub> O/D <sub>2</sub> O
Magh-I-PNPs-NODA	0.5	182	H <sub>2</sub> O/D <sub>2</sub> O

**Abbreviations:** PNP, polyethyleneglycol-based nanoparticles; NODA, 2,2'-(7-(4-((2-aminoethyl)amino)-1-carboxy-4-oxobutyl)-1,4,7-triazonane-1,4-diyl) diacetic acid; CAN, ceric ammonium nitrate.

## Radiolabeling of NPs with $^{68}\text{Ga}$

The  $^{68}\text{Ga}$  ( $T_{1/2} = 68$  minutes,  $\beta^+ = 89\%$ , Electronic Capture (EC) = 11%) was obtained from an iThemba  $^{68}\text{Ge}/^{68}\text{Ga}$  generator system (IDB Holland bv, Baarle-Nassau, Netherlands) with a nominal  $^{68}\text{Ge}$  activity of 740 MBq installed at CIC biomaGUNE (Guipuzcoa, Spain). The generator was eluted with 0.6 M of HCl solution (6 mL). Aqueous HCl solution (37%, 2.5 mL) was added to the generator eluate, giving a final HCl concentration of 4 M. The resulting solution (total volume = 8.5 mL) was passed through a Chromafix<sup>®</sup> 30-PS-HCO<sub>3</sub>-anion-exchange column (MACHEREY-NAGEL GmbH and Co, Düren, Germany; 45 mg, conditioned sequentially with 3 mL of purified water and 3 mL of 4 M aqueous HCl solution) at a flow rate of 3 mL/minute at room temperature and dried under air. The  $^{68}\text{Ga}$  was then eluted with 2 mL of purified water at a flow rate of 0.7 mL/min and the eluate (~220 MBq) was collected in a vial precharged with 45 mg of 4-(2-hydroxyethyl)-1-piperazineethanesulfonic acid (HEPES). After the addition of 1 M NaOH solution (5–10  $\mu\text{L}$ , final pH = 3.5) to the  $^{68}\text{Ga}$  eluate, 200  $\mu\text{L}$  of NPs (Magh-1-PNPs-NODA) solution were added and the vial, and was heated at 60°C for 30 minutes. The reaction crude was cooled at room temperature and  $^{68}\text{Ga}$ -labeled NPs were filtered under centrifugation (10,000 rpm, 10 minutes) using Amicon<sup>®</sup> Ultra-4 Centrifugal Filter Units (10 kDa, Millipore Corporation). The residue was washed twice with HEPES solution (pH = 3.5) and finally suspended in physiologic saline solution. All fractions were measured in a dose calibrator (CRC<sup>®</sup> – 25PET Dose Calibrator, Capintec, Inc, Ramsey, NJ). The labeling yield of the NPs was calculated as the ratio between the amount of radioactivity in the NPs solution and the total amount of radioactivity in all fractions.

Quality control of the NPs was performed by thin layer chromatography (TLC). A fraction of the NPs solution (100  $\mu\text{L}$ ) was mixed with a solution containing ethylenediaminetetraacetic acid (EDTA, 1 mg/mL). After shaking for 10 seconds, 5  $\mu\text{L}$  were deposited on a silica gel 60 F254 plate (Macherey-Nagel) and eluted with a mixture of buffered 0.1 M aqueous NaOAc solution (pH = 4.5)/0.1 M aqueous EDTA solution 90/10. After complete elution, the plates were dried at 60°C and analyzed using a radio-TLC reader (miniGITA Star, Raytest Isotopenmessgeräte GmbH, Straubenhardt, Germany) and the fractions corresponding to labeled NPs ( $R_f < 0.1$ ) and free gallium ( $R_f \sim 0.35$ ) were quantified. The same analytical procedure and conditions were used to assess the stability of labeled NPs in physiologic saline solution and in rat serum; in this case, the NPs solution was analyzed at different times after preparation (15, 30, 60, and 90 minutes).

## Toxicity assays

### Cell lines

Human PDAC-derived cell lines Panc-1, ASPC-1, MiaPaCa, Su86.86, T3M4, BxPC3, and Colo-357 were kindly provided by Dr Klaus Felix (University of Heidelberg, Heidelberg, Germany). ASPC-1, Su86.86, T3M4, BxPC3, and Colo-357 cell lines were maintained in culture in Roswell Park Memorial Institute medium supplemented with 10% fetal bovine serum, L-glutamine, penicillin, and streptomycin. Panc-1 and MiaPaCa cell lines were maintained in DMEM supplemented with 10% fetal bovine serum, L-glutamine, penicillin, and streptomycin.

### Viability assay

PDAC cells were seeded in flat-bottom 96-well plates at 5000 cells/well in a volume of 200  $\mu\text{L}$  of supplemented medium. After 72 hours of culture in the presence/absence of increasing dosage of Magh-1-PNPs-NODA NPs, 25  $\mu\text{L}$  of 5 mg/L 3-(4,5-dimethylthiazol-2-yl)-2,5-diphenyltetrazolium bromide (MTT, Sigma-Aldrich, St Louis, MO) was added directly to the cells followed by an additional 4 hours of incubation, then 100  $\mu\text{L}$  of DMSO was added. The optical density of individual wells was measured at a wavelength of 550 nm with Infinite<sup>®</sup> F500 (Tecan Group, Ltd, Mannedorf, Switzerland). All assays were performed in triplicate.

## Imaging studies

### Image acquisition

Male rats weighting 325–375 g (Sprague–Dawley, Harlan Laboratories, Udine, Italy) were used to perform PET studies. The animals were maintained and handled in accordance with the Guidelines for Accommodation and Care of Animals (European Convention for the Protection of Vertebrate Animals Used for Experimental and Other Scientific Purposes) and in accordance with internal guidelines, and experimental procedures were previously approved by local authorities. PET studies were performed using an eXploreVista-CT small animal PET-CT system (GE Healthcare, Little Chalfont, England). During PET studies, rats were kept normothermic using a heating blanket (Homoeothermic Blanket Control Unit; Bruker Optik GmbH). Three animals were submitted to whole body scans to assess the biodistribution pattern of labeled NPs. In all cases, anesthesia was induced with 3% isoflurane and maintained by 1.5% to 2% of isoflurane in 100% O<sub>2</sub>. The tail vein was catheterized with a 24-gauge catheter for intravenous administration of  $^{68}\text{Ga}$ -labeled NPs ( $7.4 \pm 2.4$  MBq, corresponding to  $3.8 \pm 1.3$   $\mu\text{g}$  of Fe<sub>2</sub>O<sub>3</sub>,

resuspended in 300  $\mu\text{L}$  of physiologic saline solution), which was injected concomitantly with the start of a PET dynamic acquisition.

Dynamic images (32 frames:  $4 \times 5$  seconds,  $4 \times 10$  seconds,  $6 \times 30$  seconds,  $6 \times 60$  seconds,  $6 \times 150$  seconds, and  $6 \times 300$  seconds) were acquired in four bed positions in the 400–700 keV energetic window, with a total acquisition time of 220 minutes. After each PET scan, CT acquisitions were also performed providing anatomical information as well as the attenuation map for the later image reconstruction. Dynamic acquisitions were reconstructed (decay and CT-based attenuation corrected) with filtered back projection using a ramp filter with a cut-off frequency of 1 Hz.

## Image analysis

PET images were analyzed using PMOD image analysis software (PMOD Technologies Ltd, Zürich, Switzerland). Volumes of interest were manually drawn in the lungs, liver, kidneys, brain, heart, spleen, bladder, and bone using the CT images as anatomical reference. Volumes of interest were then transferred to the PET images, and time activity curves (decay corrected) were obtained for each organ as cps/cm<sup>3</sup>. Injected dose and organ mass normalizations were finally applied to data to get time activity curves as standardized uptake values for each organ.

## Results and discussion

### Chemistry and nanotechnology

In a previous work, the production of hydrophilic water-compatible maghemite ( $\gamma\text{-Fe}_2\text{O}_3$ ) was described.<sup>6</sup> Accordingly, the experimental conditions did not involve any surface-passivating bifunctional ligand, nor routinely used physically adsorbed natural/nonnatural polymer. More specifically, this fabrication process comprises the high-power ultrasonic irradiation of preformed 10–15 nanosized magnetite ( $\text{Fe}_3\text{O}_4$ ) NPs together with the strong oxidant ceric ammonium nitrate [CAN,  $\text{Ce}^{\text{IV}}(\text{NH}_4)_2(\text{NO}_3)_6$ ] in a 1/1 v/v acetone/ $\text{H}_2\text{O}$  mixture.<sup>6</sup> Under these conditions, the simultaneous oxidation of the magnetite NPs to maghemite NPs and CAN-mediated modification(s) of the NP surface charge/functionality resulted in crystalline, hydrophilic, and strongly positively charged CAN-stabilized maghemite NPs that formed extremely stable colloidal water dispersions due to electrostatic repulsive interactions. These conditions also promote the formation of a polyCOOH-containing organic shell on the NP surface, which allows further grafting of the particles.<sup>11</sup>

These NPs have an average hydrodynamic radius of 44–55 nm (DLS measurements), a  $\zeta$  potential of  $-40$ – $-50$  mV, and are 8–12 nm in average size as measured from TEM (TEM micrograph analysis of more than 100 particulate objects). In addition, <sup>57</sup>Fe Mössbauer spectroscopy performed at 300 K afforded a spectrum that discloses asymmetrical sextets of broadened lines that were attributed to significant superparamagnetic fluctuations. The NPs superparamagnetism feature that is essential for MRI application, was also confirmed by superconductive quantum interference device.<sup>6</sup> The so-formed CAN-maghemite NPs are water-dispersible, and in these conditions (ie, without any surface modification), their entrapment into polymeric NPs is rather hard. In order to solve this phase compatibility problem, the maghemite NP surface was coated by a hydrophobic organic ligand (ethyl 12-((3,4-dihydroxyphenethyl)amino)-12-oxododecanoate (herein referred as ligand 1) specially designed to ensure lipophilicity to the iron oxide NPs. Ligand 1 possesses a catechol unit at one end, a central aliphatic chain, and a terminal ester group. On the one hand, the catechol unit is well known to present a strong affinity to iron due to both the  $\sigma$  and  $\pi$  donor power of oxygen atoms.<sup>12</sup> On the other hand, the aliphatic chain is necessary to confer stability to the systems thanks to interchain hydrogen bonding, while the terminal ester group should provide good solubility of the NPs in common organic solvents. To prove this idea, a solubility test of CAN-Magh versus Magh-1 in a water/dichloromethane mixture was performed (see Supplementary Material, Figure S6A). As could be expected upon coating of CAN-Magh NPs with ligand 1, the NPs readily transferred from the water phase to the dichloromethane organic layer.

IR analysis (see Supplementary Material, Figure S5) confirmed the successful coating of the maghemite NPs with ligand 1: in the region between 3300 and 3500  $\text{cm}^{-1}$ , there is a strong absorption due to the hydroxyl groups present on the surface of the maghemites that make impossible the identification of polar organic moieties. However, the stretching of aliphatic  $-\text{CH}$  of the ligand can be observed in region between 2800 and 3000  $\text{cm}^{-1}$ . Furthermore, at 1700 and 1640  $\text{cm}^{-1}$ , the stretching of the two  $\text{C}=\text{O}$  (ester and amide groups) can be easily recognized. In addition, thermogravimetric analysis confirmed the presence of an organic coating of 35.6% in mass (see Figure S3B).

Following our interest in the entrapment of lipophilic MNPs,<sup>13–15</sup> the hydrophobic Magh-1 NPs were incorporated into polymeric micelles using the nanoprecipitation technique.<sup>15,16</sup> The amphiphilic copolymer PLGA-b-PEG-COOH

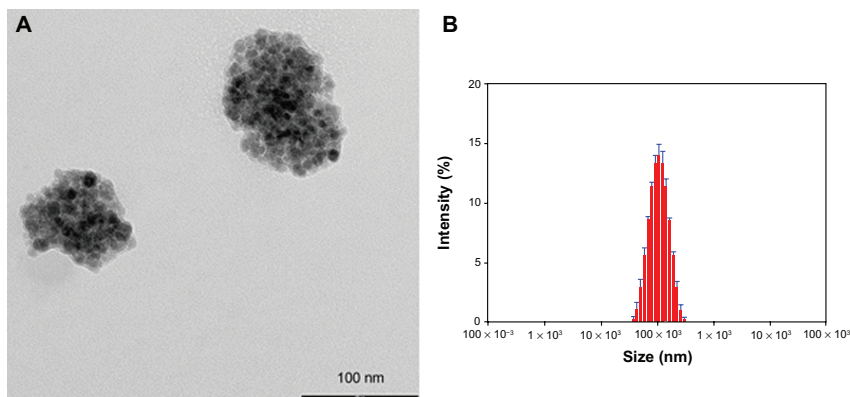


**Figure 2** TEM image and relative DLS measurements of Magh-1-PNPs. TEM image (A) and relative DLS measurements (B) of Magh-1-PNPs. **Abbreviations:** TEM, transmission electron microscopy; PNPs, polyethyleneglycol-based nanoparticles; DLS, dynamic light scattering.

served as a biocompatible coating that may enable blood circulation. Briefly, an acetone solution of Magh-1 and copolymer was added dropwise to dd water under vigorous stirring leading to the formation of Magh-1-PNPs. The as-synthesized polymeric NPs were characterized by means of DLS (Figure 2B). The analysis showed a hydrodynamic radius of  $95.32 \pm 0.88$  nm with a polydispersity index (PDI) value of  $0.153 \pm 0.007$ . The NPs proved to be stable in an aqueous environment with a  $\zeta$ -potential value of  $-39.2$  mV at pH = 5.45. TEM observations confirmed the formation of polymeric shells around clusters of magh-1 (Figure 2A).

The concentration of iron was investigated by means of atomic absorption spectrophotometry, and it was found to be 112 ppm.

In order to add the second contrast agent to obtain the dual modal imaging platform, the polymeric NP surface was functionalized with the  $^{68}\text{Ga}$  chelating agent, NODA. The carboxylic acid originating from the free end of the PEG building block was utilized for this functionalization reaction: first, it was activated with 1-ethyl-3-(3-dimethylaminopropyl) carbodiimide (EDC) in water. In the next step, NODA was introduced in the reaction mixture and an amidation reaction between the activated acid and NODA amine function occurred. The resulting Magh-1-PNPs-NODA possesses a hydrodynamic radius of  $92.34 \pm 0.72$  nm with a polydispersity index value of  $0.167 \pm 0.011$  (DLS analysis), and a  $\zeta$ -potential value of  $-44$  mV at pH = 6.30. The concentration of iron in this case was found to be of 134 ppm with a total yield in iron of 64%.

### Magh-1-PNPs-NODA in vitro toxicity in PDAC-derived cell lines

One potential field of application of  $^{68}\text{Ga}$ -labeled NPs is the clinical and preclinical diagnosis and evaluation of PDAC,

which is one of the most deadly tumors, for which detection of neoplastic lesions at an early stage might permit life-saving interventions.<sup>10</sup>

Thus, we evaluated the toxicity of Magh-1-PNPs-NODA NPs on different human PDAC-derived cell lines (ASPC-1, Panc-1, MiaPaCa, Su86.86, T3M4, BxPC3, Colo-357) using cell growth inhibition assays (MTT test, Figure 3 and Figure S1). Magh-1-PNPs-NODA NPs caused a modest dose-dependent decrease of cell proliferation.

Despite the fact that a considerable variability among cell lines was observed, about a 50% reduction of the proliferation rate was observed within 72 hours of incubation

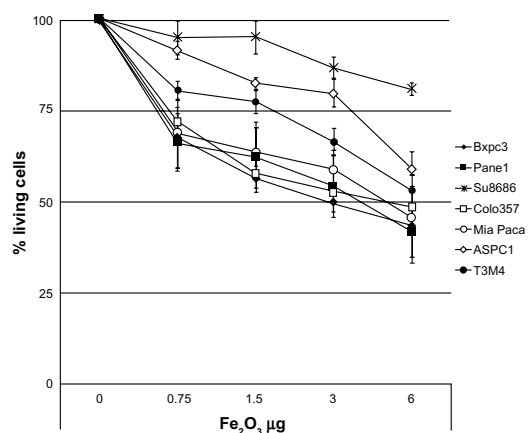


**Figure 3** Cellular viability rate versus maghemite concentration after 72 hour incubation with Magh-1-PNPs-NODA NPs.

**Notes:** Relative values were normalized to the values from the corresponding untreated cells and are shown as percent of survival. Results are expressed as a mean percentage of three independent experiments performed in triplicate  $\pm$  SD.

**Abbreviations:** NPs, nanoparticles; PNPs, polyethyleneglycol-based nanoparticles; NODA, 2,2'-(7-(4-((2-aminoethyl)amino)-1-carboxy-4-oxobutyl)-1,4,7-triazonan-1,4-diylo)diacetic acid; SD, standard deviation.



in the majority of the culture cells when 3–6  $\mu\text{g}$  of  $\text{Fe}_2\text{O}_3$  was present. Notably, at higher concentrations, the Su8686 cell growth was only marginally affected by Magh-1-PNPs-NODA NPs.

## NMR relaxivity

Although, in general, cells can survive short-term exposure to low concentrations of NPs, several groups have found cytotoxic effects to emerge in a dose- and time-dependent manner for most type of NPs. This is generally due to NP internalization inside cells, which elicits inflammatory responses, cell-cycle irregularities, and gene expression alterations.<sup>17</sup> Although a certain extent of Magh-1-PNP-induced cytotoxicity in the present study occurred, it is important to keep in mind that *in vitro* results can differ from what is found *in vivo*, and that toxicity *in vitro* may not necessarily be clinically relevant. This depends on whether repetitive NP administration is required, as well as on the NP bioavailability at the target site.

All nanocomposites were very weak  $T_1$  relaxing agents, and as expected for maghemite NPs, they were strong  $T_2$  relaxation agents (Table 1). The obtained values indicate that the polymer shell enhances  $R_2$  relaxivity, making the NODA functionalized compound ideally suitable as a  $T_2/T_2^*$  MRI contrast agent.

## Radiolabeling of NPs with $^{68}\text{Ga}$

The attachment of positron emitters to macromolecules is usually approached by the chelation of a (positron emitter) metallic atom using a bifunctional polyazacarboxylate- or tetraaza-macrocyclic.<sup>18,19</sup> This strategy can be transferred to the incorporation of radioisotopes into NPs, because contrary to the case of the radio-halogens (eg,  $^{18}\text{F}$ ), the labeling reaction usually takes place under mild conditions without damaging the NPs.

A number of metallic PET isotopes have been used to date for NP labeling, including  $^{64}\text{Cu}$ ,<sup>20</sup> and  $^{68}\text{Ga}$ .<sup>21</sup> Copper-64 has probably been the most widely used due to its relatively long half life (12.7 hours), which permits PET evaluation of slow biochemical pathways. However, the production of  $^{64}\text{Cu}$  requires the irradiation of  $^{64}\text{Ni}$  with protons, and a laborious purification process using anion exchange chromatography.<sup>22</sup> Due to this fact  $^{68}\text{Ga}$ , which can be easily obtained from a commercially available  $^{68}\text{Ge}/^{68}\text{Ga}$  generator, is gaining interest in the development of multimodal imaging agents, and its incorporation into NPs using bifunctional chelating agents has been already reported in the literature.<sup>23</sup> In the current work, a similar procedure was followed but a preconcentration step was applied to the  $^{68}\text{Ga}^{3+}$  solution obtained from

the generator.<sup>23</sup> Under optimized experimental conditions ( $T = 60^\circ\text{C}$ ,  $t = 30$  minutes,  $\text{pH} = 3.5$ ), the labeling yield of Magh-1-PNPs-NODA, as measured by gamma-counting after filtration, was  $84\% \pm 6\%$ . Quality control of the NPs performed by TLC (Figure 4, red line) showed no peak corresponding to free  $^{68}\text{Ga}$  after filtration and reconstitution in physiologic saline. The stability of labeled NPs in physiologic saline solution and in rat serum was also determined by TLC. The fraction of free gallium at  $t = 90$  minutes was  $<5\%$  in both media (not shown in Figure 4). These results confirm the stability of the  $^{68}\text{Ga}$ -NODA complex, which is very appropriate for subsequent *in vivo* studies.

## Imaging studies

In Figure 5A, an image corresponding to the biodistribution pattern at long times after administration (frames 10–32) is presented. High accumulation in the liver and spleen can be visualized. The significant accumulation observed in the lungs might suggest the presence of a small percentage of aggregates, probably formed after administration of the NPs. The significant levels of radioactivity detected in the heart, especially at long times after administration of the labeled NPs, point towards a slow clearance from the bloodstream (Figure 5B). The low level of radioactivity in the bladder (Figure 5H) indicates a partial (and slow) elimination via urine.

Time-activity curves for the heart, brain, lungs, kidney, spleen, liver, and bladder are shown in Figure 5B to H. Following tail vein injection, dynamic imaging revealed a steep peak in the heart, brain, and lungs (Figure 5B–D, respectively) as expected from a transient increase in blood

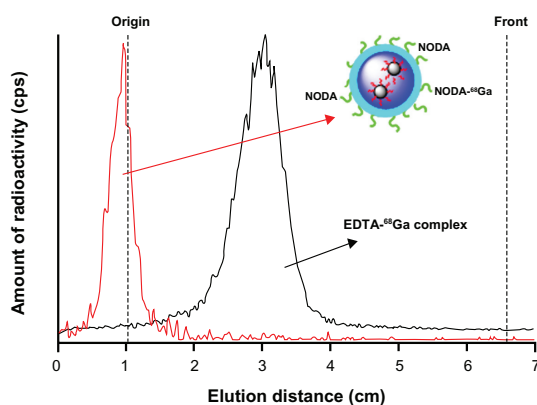


**Figure 4** TLC profiles obtained for  $^{68}\text{Ga}$ -labelled NPs (red line,  $R_f = 0$ ) and free EDTA- $^{68}\text{Ga}$  complex (black line,  $R_f = 0.35$ ).

**Note:** The complex EDTA- $^{68}\text{Ga}$  is generated *in situ*.

**Abbreviations:** TLC, thin layer chromatography; NPs, nanoparticles; EDTA, ethylenediaminetetra-acetic acid; NODA, 2,2'-(7-(4-((2-aminoethyl)amino)-1-carboxy-4-oxobutyl)-1,4,7-triazonane-1,4-diyl)diacetic acid.

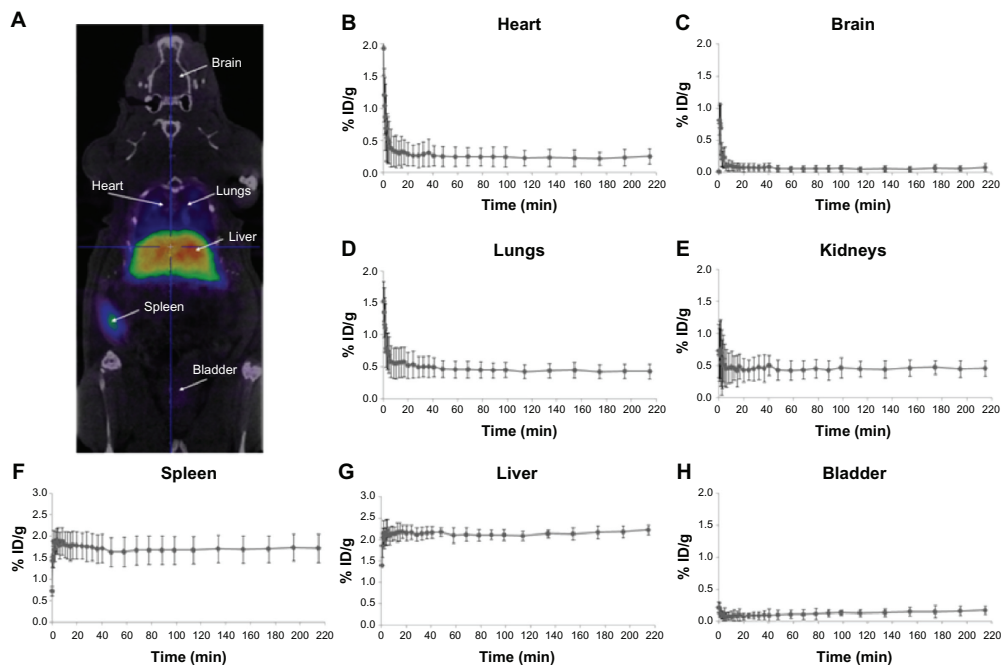


**Figure 5** PET image and CT time-activity curves of  $^{68}\text{Ga}$ . PET image of  $^{68}\text{Ga}$ -labeled NPs signal corresponding to averaged time frames at  $t > 20$  minutes after IV injection (A). CT images were adjusted on the Y-axis for an appropriate fitting with the tracer distribution. Time-activity curves for heart (B), brain (C), lungs (D), kidneys (E), spleen (F), and liver (G) after IV administration of  $^{68}\text{Ga}$ -labeled NPs.

**Note:** Average values  $\pm$  standard deviation ( $n = 3$ ) are shown.

**Abbreviations:** PET, positron emission tomography; CT, computerized tomography; NPs, nanoparticles; IV, intravenous; ID, injective dose.

pool activity. Brain activity decreased to negligible values ( $<0.1\%$  injected dose  $\text{g}^{-1}$ ) 10 minutes after injection; higher values were reached in the heart ( $\sim 0.25\%$  ID  $\text{g}^{-1}$ ) and lungs ( $\sim 0.45\%$  ID  $\text{g}^{-1}$ ). Uptake into the spleen (Figure 5F) and liver (Figure 5G) was rapid. Within 5 minutes of the appearance of radioactivity in the blood, liver, and spleen, levels reached a plateau at 1.7% and 2.1% injected dose  $\text{g}^{-1}$ , respectively. This level was maintained until the end of the study (4 hours after administration of NPs).

Accumulation of radioactivity in the bladder (Figure 5H) slowly increased along the scan time up to  $0.2\%$  ID  $\text{g}^{-1}$  at the end of the study, while the accumulation of radioactivity in bones (results not shown) was very low at all times ( $<0.1\%$  of ID/g all along the study). The results obtained in the current work demonstrate the suitability of  $^{68}\text{Ga}$ -labelling for subsequent determination of biodistribution patterns. Although the NPs described here did not have any functionalization to target specific organs or tissues, the same labeling and quantification strategy could be applied to targeted NPs to assess the potentially selective accumulation in specific organs or tumors. Therefore, the

NPs presented here are an excellent platform for further functionalization in order to become suitable PET/MRI dual imaging contrast agents.

Indeed, our *in vitro* growth inhibition studies indicate an  $\text{IC}_{50}$  value for PDAC cell lines of approximately  $3.0\text{--}6.0\ \mu\text{g}$  of  $\text{F}_2\text{O}_3$  (Figure 3). This is a considerably high value considering the dosage of NPs injected *in vivo* for imaging experiments ( $2.67\ \mu\text{g}$  of  $\text{F}_2\text{O}_3$  injected into animals, Figure 5) suggesting a low grade of toxicity of Magh-1-PNPs-NODA NPs. It is well known that the physicochemical characteristics of NPs are often changed when they come into contact with the blood. In particular, NP interactions with proteins in the blood both quantitatively and qualitatively affect NP half-lives and biodistribution. Surface protein deposition may induce NP aggregation, and large aggregates may be trapped in the capillaries. Also, surface opsonization is an issue (ie, the deposition of proteins that facilitate NP recognition and clearance from the blood by circulating phagocytes or tissue macrophages in direct contact with the blood). All these events contribute to the reduction of NP bioavailability at the target site. A very recent reference discussed these issues.<sup>24</sup>

Thus further investigation can be carried out on Magh-1-PNPs-NODA NPs for the application of such NPs for the early diagnosis and evaluation of pancreatic neoplasms.

## Conclusion

We have developed a novel multifunctional biocompatible hybrid nanocarrier for dual PET/MRI imaging. This nanocarrier is composed of a polymer shell containing maghemite NPs at its lipophilic core and bearing  $^{68}\text{Ga}$  chelating group on the outer surface. The  $T_2$  relaxivity values show promising perspectives for the NPs to be used as MRI contrast agents; moreover, the incorporation of the positron emitter  $^{68}\text{Ga}$ , and the stability of the resulting NP-NODA- $^{68}\text{Ga}$  complex, confirm the suitability of the labeled NPs as contrast agents for in vivo PET imaging. The values at which Magh-1-PNPs-NODA proved to be suitable for MRI/PET analysis were found to be not toxic in vitro on seven cell lines of PDAC. Thus, the nanopatform presented here is a promising tool for the future development of innovative PET/MRI diagnostic agents. Additional applications of this nanocarrier in nanomedicine are currently under investigation.

## Acknowledgments

This work has been supported with the funding of the EU-FP7 European project SaveMe (contract number CP-IP 263307-2).

The authors would like to thank Maria Puigvila, Boguslaw Szczupak, and Enrique Alonso for technical support. Lorena Passoni receives funding from Fondazione Umberto Veronesi (Milano, Italy).

## Disclosure

The authors report no conflicts of interest in this work.

## References

- Karim-Kos HE, de Vries E, Soerjomataram I, Lemmens V, Siesling S, Coebergh JW. Recent trends of cancer in Europe: a combined approach of incidence, survival and mortality for 17 cancer sites since the 1990s. *Eur J Cancer*. 2008;44(10):1345–1389.
- Jemal A, Siegel R, Xu J, Ward E. Cancer statistics, 2010. *CA Cancer J Clin*. 2010;60(5):277–300.
- Cheon J, Lee JH. Synergistically integrated nanoparticles as multimodal probes for nanobiotechnology. *Acc Chem Res*. 2008;41(12):1630–1640.
- Corot C, Robert P, Idée JM, Port M. Recent advances in iron oxide nanocrystal technology for medical imaging. *Adv Drug Deliv Rev*. 2006;58(14):1471–1504.
- Moghimi SM, Hunter AC, Murray JC. Long-circulating and target-specific nanoparticles: theory to practice. *Pharmacol Rev*. 2001;53(2):283–318.
- Haviv AH, Grenèche JM, Lellouche JP. Aggregation control of hydrophilic maghemite ( $\gamma\text{-Fe}_2\text{O}_3$ ) nanoparticles by surface doping using cerium atoms. *J Am Chem Soc*. 2010;132(36):12519–12521.
- Gref R, Minamitake Y, Peracchia MT, Trubetskoy V, Torchilin V, Langer R. Biodegradable long-circulating polymeric nanospheres. *Science*. 1994;263(5153):1600–1603.
- Cherry SR. Fundamentals of positron emission tomography and applications in preclinical drug development. *J Clin Pharmacol*. 2001;41(5):482–491.
- Bond-Smith G, Banga N, Hammond TM, Imber CJ. Pancreatic adenocarcinoma. *BMJ*. 2012;344:e2476.
- Zafar SF, El-Rayes BF. Chemotherapeutic strategies in advanced or metastatic pancreatic adenocarcinoma. *Am J Clin Oncol*. Epub May 24, 2012.
- Esman N, Haviv A, Lellouche JP. Magnetically responsive polypyrrole nanotubes using Ce(III)-stabilized maghemite nanoparticles. *Nanotechnology*. 2011;22(28):285604.
- Yuen AK, Hutton GA, Masters AF, Maschmeyer T. The interplay of catechol ligands with nanoparticulate iron oxides. *Dalton Trans*. 2012;41(9):2545–2559.
- Comes Franchini M, Baldi G, Bonacchi D, et al. Bovine serum albumin-based magnetic nanocarrier for MRI diagnosis and hyperthermic therapy: a potential theranostic approach against cancer. *Small*. 2010;6(3):366–370.
- Baldi G, Bonacchi D, Franchini MC, et al. Synthesis and coating of cobalt ferrite nanoparticles: a first step toward the obtaining of new magnetic nanocarriers. *Langmuir*. 2007;23(7):4026–4028.
- Comes Franchini M, Bonini BF, Camaggi CM, et al. Design and synthesis of novel 3,4-disubstituted pyrazoles for nanomedicine applications against malignant gliomas. *Eur J Med Chem*. 2010;45(5):2024–2033.
- Cheng J, Teply BA, Sherif I, et al. Formulation of functionalized PLGA-PEG nanoparticles for in vivo targeted drug delivery. *Biomaterials*. 2007;28(5):869–876.
- Lewinski N, Colvin V, Drezek R. Cytotoxicity of nanoparticles. *Small*. 2008;4(1):26–49.
- Kukis DL, Diril H, Greiner DP, et al. A comparative study of copper-67 radiolabeling and kinetic stabilities of antibody-macrocycle chelate conjugates. *Cancer*. 1994;73(Suppl 3):779–786.
- Boswell CA, Sun X, Niu W, et al. Comparative in vivo stability of copper-64-labeled cross-bridged and conventional tetraazamacrocyclic complexes. *J Med Chem*. 2004;47(6):1465–1474.
- Huang X, Zhang F, Lee S, et al. Long-term multimodal imaging of tumor draining sentinel lymph nodes using mesoporous silica-based nanopores. *Biomaterials*. 2012;33(17):4370–4378.
- Ko HY, Choi KJ, Lee CH, Kim S. A multimodal nanoparticle-based cancer imaging probe simultaneously targeting nucleolin, integrin  $\alpha v \beta 3$  and tenascin-C proteins. *Biomaterials*. 2011;32(4):1130–1138.
- Matarrese M, Bedeschi P, Scardaoni R, et al. Automated production of copper radioisotopes and preparation of high specific activity [(64)Cu] Cu-ATSM for PET studies. *Appl Radiat Isot*. 2010;68(1):5–13.
- Velikyan I, Beyer GJ, Långström B. Microwave-supported preparation of (68)Ga bioconjugates with high specific radioactivity. *Bioconjug Chem*. 2004;15(3):554–560.
- Moghimi SM, Hunter AC, Andresen TL. Factors controlling nanoparticle pharmacokinetics: an integrated analysis and perspective. *Annu Rev Pharmacol Toxicol*. 2012;52:481–503.
- Kaiser E, Colescott RL, Bossinger CD, Cook PI. Color test for detection of free terminal amino groups in the solid-phase synthesis of peptides. *Anal Biochem*. 1970;34(2):595–598.

## Supplementary materials

### 1. Derivatization of maghemite NPs with 1,4-diaminobutane for Kaiser test

*N*-(3-dimethylaminopropyl)-*N'*-ethylcarbodiimide hydrochloride (EDC), 50 mg (0.26 mmol), was added to 1 mL of maghemite NPs suspended in doubly distilled water (ddH<sub>2</sub>O), and the reaction mixture was shaken for 40 minutes at room temperature. Then, the excess of EDC was washed out by centrifugation at 8000 rpm (8 minutes, 5°C, three times). Then, 1 mL of ddH<sub>2</sub>O and 0.25 mL (3.22 mmol) of 1,4-diaminobutane were added and the solution was shaken for 1.5 hours. The excess of amine was removed by centrifugation at 12,500 rpm (5°C, and three times).<sup>25</sup>

## Results

Kaiser test<sup>25</sup> of NPs after surface derivatization with 1,4-diaminobutane afforded average values of 0.163 mmol of accessible COOH/g NPs. ICP measurements: Fe concentration was 3.24 mg/mL while Ce concentration was 1.053 µg/mL (Weight ratio Ce/Fe = 0.000325).

2. Acetyl chloride (20 µL, 0.28 mmol) was added to a stirred solution of 12-hydroxydodecanoic acid (1.00 g, 4.63 mmol) in 40 mL of ethanol under nitrogen atmosphere. The mixture was heated to reflux for 24 hours, then, the solvent was removed under vacuum and the resulting oil (1.02 g, 4.47 mmol, yield = 90%) was used for the next step without further purification.

Hydrogen-1 nuclear magnetic resonance (300 MHz, CDCl<sub>3</sub>): δ = 4.09 (q, 2H, CH<sub>2</sub>), 3.59 (t, 2H, CH<sub>2</sub>), 2.23 (t, 2H, CH<sub>2</sub>), 1.58 (bs, 6H, CH<sub>2</sub>), 1.25 (bs, 15H, CH<sub>2</sub> + CH<sub>3</sub>).

Carbon nuclear magnetic resonance: (75 MHz, CDCl<sub>3</sub>): δ = 174.023 (C=O), 61.835 (CH<sub>2</sub>), 60.170 (CH<sub>2</sub>), 34.035 (CH<sub>2</sub>), 32.578 (CH<sub>2</sub>), 29.560 (CH<sub>2</sub>), 29.477 (CH<sub>2</sub>), 29.385

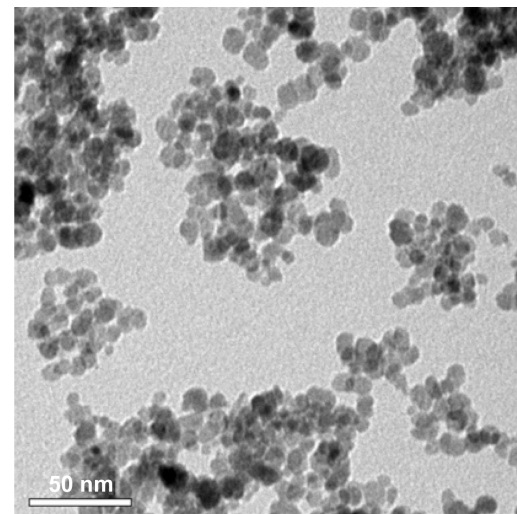


**Figure S1** Transmission electron microscopy image of ceric ammonium nitrate (CAN)-Magh nanoparticles (NPs).

(2CH<sub>2</sub>), 29.210 (CH<sub>2</sub>), 29.047 (CH<sub>2</sub>), 25.583 (CH<sub>2</sub>), 24.913 (CH<sub>2</sub>), 14.200 (CH<sub>3</sub>).

3. A suspension of periodic acid (2.13 g, 9.33 mmol) in 40 mL of acetonitrile was left to react for 20 minutes at room temperature. Then, a solution of ethyl 12-hydroxydodecanoate (1.02 g, 4.16 mmol) and pyridinium chlorochromate (20 mg, 0.091 mmol) in 10 mL of acetonitrile was slowly added, keeping the temperature at 0°C with an ice bath. Once completed, the addition the ice bath was removed and the mixture was left to react for 24 hours at room temperature.

Afterward, 40 mL of ethyl acetate were added, and the mixture was first washed with water (3 × 40 mL), then with an aqueous solution of sodium hydrogen sulfate (40% m/V, 3 × 40 mL), and finally again with water (2 × 40 mL). The organic phase was dried with anhydrous sodium sulfate, and it was filtered and evaporated in vacuo to obtain the product as a white solid (1.00 g, 3.87 mmol, yield = 93%). melting point: 51°C–53°C.

Hydrogen-1 nuclear magnetic resonance (300 MHz, CDCl<sub>3</sub>): δ = 4.12 (q, 2H, CH<sub>2</sub>), 2.37 (t, 2H, CH<sub>2</sub>), 2.29 (t, 2H, CH<sub>2</sub>), 1.61 (bs, 4H, CH<sub>2</sub>), 1.26 (bs, 15H, CH<sub>2</sub> + CH<sub>3</sub>).

Carbon nuclear magnetic resonance: (150 MHz, CDCl<sub>3</sub>): δ = 180.046 (C=O), 174.003 (C=O), 60.169 (CH<sub>2</sub>), 34.342

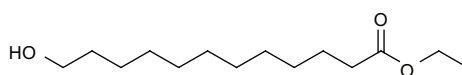


**Figure S2** Synthesis of ethyl 12-hydroxydodecanoate.

**Table S1** Statistical analysis of the mean values reported in Figure 3

Cell line	P-values			
	Treatment: Fe <sub>2</sub> O <sub>3</sub> mg/mL			
	0.75	1.5	3	6
BxPC3	0.010596	0.000987	2.94E-05	0.004902
Colo357	0.007747	0.001283	0.002206	0.000895
MiaPaCa	0.017082	0.000392	0.00308	2.58E-05
Pancl	0.008794	0.01066	0.005601	0.00213
ASPC1	0.012462	0.0272229	0.00528	0.002234
T3M4	0.010854	0.006424	0.002105	0.001432
Su8686	0.108404	0.101878	0.007791	0.001184

**Notes:** P-values were calculated using a two-sample Student's *t* test comparing differences in the means between two groups, treated versus untreated, after 72 hours of culture. P-values < 0.005 were considered statistically significant. Statistically significant values are highlighted.

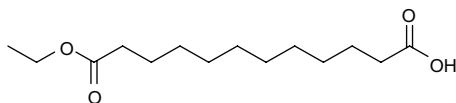


**Figure S3** Synthesis of 12-ethoxy-12-oxododecanoic acid.

(CH<sub>2</sub>), 34.041 (CH<sub>2</sub>), 29.441 (CH<sub>2</sub>), 29.295 (CH<sub>2</sub>), 29.156 (2CH<sub>2</sub>), 29.060 (CH<sub>2</sub>), 28.987 (CH<sub>2</sub>), 24.918 (CH<sub>2</sub>), 24.625 (CH<sub>2</sub>), 14.198 (CH<sub>3</sub>).

4. To a stirred solution of 12-ethoxy-12-oxododecanoic acid (3.87 mmol, 1.00 g) in 30 mL of anhydrous tetrahydrofuran (THF) under nitrogen, 1,1-carbonyldiimidazole (6.17 mmol, 0.99 g) was slowly added. The mixture was stirred for 1.5 hours, diluted with an additional 70 mL of anhydrous THF, and added dropwise (4 hours) to a suspension of dopamine hydrochloride (3.87 mmol, 0.73 g) and pyridine (5.8 mmol, 0.47 mL) in the same solvent (30 mL of anhydrous THF), maintaining a nitrogen atmosphere. The mixture was left to react for 1 hour, and then the solvent was removed under vacuum.

The solid was redispersed in ethyl acetate and washed three times with water. The organic phase was dried over MgSO<sub>4</sub>, filtered and evaporated in vacuo. The crude product was then purified with column chromatography (EtOAc/Pet ether, 3:1) to provide the final ligand (0.72 g, 1.83 mmol, yield = 47%). mp: 60°C–62°C.

Hydrogen-1 nuclear magnetic resonance (300 MHz, CDCl<sub>3</sub>): δ = 6.81 (d, 1H, Ar), 6.78 (m, 1H, Ar), 6.59 (d, 1H, Ar), 5.65 (bs, 1H, NH), 4.15 (q, 2H, CH<sub>2</sub>), 3.45 (q, 2H, CH<sub>2</sub>), 2.70 (t, 2H, CH<sub>2</sub>), 2.30 (t, 2H, CH<sub>2</sub>), 2.18 (t, 2H, CH<sub>2</sub>), 1.60 (bs, 4H, CH<sub>2</sub>), 1.22 (bs, 15H, CH<sub>2</sub> + CH<sub>3</sub>).

Carbon nuclear magnetic resonance (150 MHz, CDCl<sub>3</sub>): δ = 174.538 (C=O), 174.373 (C=O), 144.518 (C), 143.225 (C), 130.490 (C), 120.373 (CH), 115.479 (CH), 155.183 (CH), 60.373 (CH<sub>2</sub>), 41.000 (CH<sub>2</sub>), 36.777 (CH<sub>2</sub>), 34.898 (CH<sub>2</sub>), 34.404 (CH<sub>2</sub>), 29.309 (CH<sub>2</sub>), 29.294 (CH<sub>2</sub>), 29.180 (CH<sub>2</sub>), 29.115 (2CH<sub>2</sub>), 29.067 (CH<sub>2</sub>), 25.730 (CH<sub>2</sub>), 24.950 (CH<sub>2</sub>), 14.251 (CH<sub>3</sub>).

Gas chromatography–mass spectrometry ES+: 416 (M + Na).

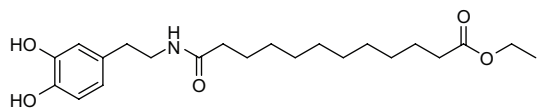


**Figure S4** Synthesis of ethyl 12-((3,4-dihydroxyphenethyl)amino)-12-oxododecanoate (EDAOC, 1).

## Coating of CAN-Magh with ligand

Original CAN-Magh solution (10 mL) was diluted with 30 mL of water and added to a solution of 1 (300 mg, 0.762 mmol) in 40 mL of ethanol. The mixture was sonicated in an ultrasound bath for 1 hour, and it was left to react overnight at room temperature under mechanical stirring. Afterward, the solution was decanted magnetically (strong external magnet) and the supernatant was removed while the brownish solid was washed with ethanol (2 × 30 mL). Finally, the solid (Magh-1) was redispersed in 80 mL of acetone, sonicated for 30 minutes (bath sonicator, Branson Ultrasonics Corporation, Danbury, CT) and immediately used in the following steps.

5. Poly(D,L-lactide-co-glycolide)-block-poly(ethylene glycol) was synthesized through the activation of carboxyl- capped PLGA-COOH (MW ~7 kDa) with N-hydroxysuccinimide using dicyclohexylcarbodiimide coupling chemistry, and then conjugated to the amine bifunctional NH<sub>2</sub>-PEG-COOH (MW ~3 kDa), in chloroform and in the presence of N,N-Diisopropylethylamine.<sup>15</sup>

6. Synthesis of Magh-1-PNPs-NODA

The linkage of 2,2'-(7-(4-((2-aminoethyl)amino)-1-carboxy-4-oxobutyl)-1,4,7-triazonane-1,4-diyl)diacetic acid (NODA) on the surface of the particle was carried out through a classic peptide formation. In particular, 35 mL of a 0.28 mM Magh-1-polyethyleneglycol-based nanoparticle water solution (0.010 mmol of D,L-lactide-co-glycolide)-block-poly(ethylene glycol) were stirred for 2 hours in the presence of 0.010 mmol of 1-ethyl-3-(3-dimethylamino-propyl)carbodiimide (1.7 mL of a 5.7 mM water solution neutralized with 0.1 M HCl solution up to pH = 7.60). Then, 0.010 mmol of NODA-GA-ethylenediamine was added (6.1 mL of a 1.6 mM water solution neutralized with 0.1 M NaOH solution up to pH = 7.15) and the reaction mixture was kept under stirring for additional 2 hours. The particles were purified with a centrifugal filter device (Amicon Ultra, Ultracel membrane with 100.000 normal molecular weight limit; Millipore Corporation, Billerica, MA) and redispersed in 25 mL of water.

7. Synthesis of Magh-1-PNPs-NODA

The linkage of 2,2'-(7-(4-((2-aminoethyl)amino)-1-carboxy-4-oxobutyl)-1,4,7-triazonane-1,4-diyl)diacetic acid (NODA) on the surface of the particle was carried out through a classic peptide formation. In particular, 35 mL of a 0.28 mM Magh-1-polyethyleneglycol-based polymeric nanoparticle water solution (0.010 mmol of poly(D,L-lactide-co-glycolide)-block-poly(ethylene glycol)) was stirred for 2 hours in the presence of 0.010 mmol of

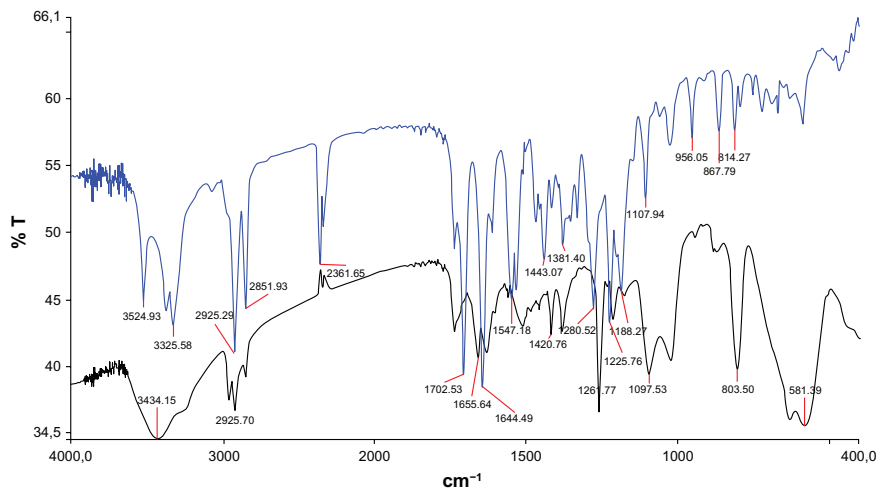


Figure S5 Infrared spectra of ceric ammonium nitrate (CAN)-Magh (black line) and Magh-I (blue line).  
Abbreviation: T, transmittance.

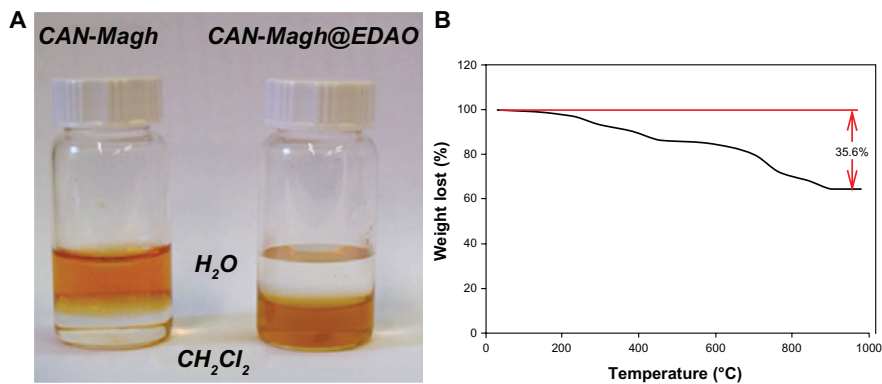


Figure S6 Solubility test of ceric ammonium nitrate (CAN)-Magh versus Magh-I (A) and thermogravimetric analysis of Magh-I (B).

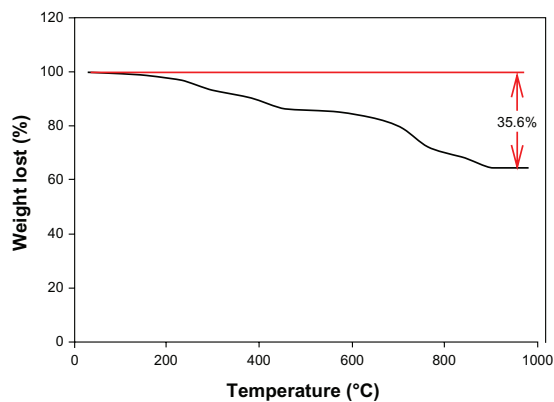


Figure S7 Synthesis of Magh-I-PNPs-NODA.

1-ethyl-3-(3-dimethylaminopropyl)carbodiimide (1.7 mL of a 5.7 mM water solution neutralized with 0.1 M HCl solution up to pH = 7.60). Then, 0.010 mmol of NODA-GA-ethylenediamine was added (6.1 mL of a 1.6 mM water solution neutralized with 0.1 M NaOH solution up to pH = 7.15),

and the reaction mixture was kept under stirring for additional 2 hours. The particles were purified with a centrifugal filter device (Amicon Ultra, Ultracel membrane with 100,000 normal molecular weight limit; Millipore Corporation, Billerica, MA) and redispersed in 25 mL of water.

### International Journal of Nanomedicine

#### Publish your work in this journal

The International Journal of Nanomedicine is an international, peer-reviewed journal focusing on the application of nanotechnology in diagnostics, therapeutics, and drug delivery systems throughout the biomedical field. This journal is indexed on PubMed Central, MedLine, CAS, SciSearch®, Current Contents®/Clinical Medicine,

Submit your manuscript here: <http://www.dovepress.com/international-journal-of-nanomedicine-journal>

Journal Citation Reports/Science Edition, EMBase, Scopus and the Elsevier Bibliographic databases. The manuscript management system is completely online and includes a very quick and fair peer-review system, which is all easy to use. Visit <http://www.dovepress.com/testimonials.php> to read real quotes from published authors.

Dovepress





Locatelli E, Bost W, Fournelle M, Llop J, Gil L, Arena F, Lorusso V, Franchini MC. Targeted polymeric nanoparticles containing gold nanorods: a therapeutic approach against glioblastoma. [Journal of Nanoparticle Research](#). 2014, 16:2304.

Rosenberger I, Strauss A, Dobiasch S, Weis C, Szanyi S, Gil-Iceta L, et al. Targeted diagnostic magnetic nanoparticles for medical imaging of pancreatic cancer. [Journal of Controlled Release](#). September 2015, 214:76–84.

Gil L, Gómez-Vallejo V, Kozirowski JM, Llop J. Radiochemical Stability Studies of Radiolabelled Nanoparticles. In: Llop J, Gómez-Vallejo V, Gibson PN editors. [Isotopes in Nanoparticles: Fundamentals and Applications](#). Pan Stanford; 2016. ISBN: 978-981-4669-08-5.





